

ETD Archive

2016

Development of Robust Control Techniques towards Damage Identification

Ryan J. Madden
Cleveland State University

Follow this and additional works at: <https://engagedscholarship.csuohio.edu/etdarchive>



Part of the [Engineering Commons](#)

[How does access to this work benefit you? Let us know!](#)

Recommended Citation

Madden, Ryan J., "Development of Robust Control Techniques towards Damage Identification" (2016). *ETD Archive*. 878.
<https://engagedscholarship.csuohio.edu/etdarchive/878>

This Dissertation is brought to you for free and open access by EngagedScholarship@CSU. It has been accepted for inclusion in ETD Archive by an authorized administrator of EngagedScholarship@CSU. For more information, please contact library.es@csuohio.edu.

DEVELOPMENT OF ROBUST CONTROL TECHNIQUES TOWARDS DAMAGE
IDENTIFICATION

RYAN J. MADDEN

Bachelor of Mechanical Engineering

Cleveland State University

2009

Master of Science in Mechanical Engineering

Cleveland State University

2010

submitted in partial fulfillment of requirements for the degree

DOCTOR OF ENGINEERING

at the

CLEVELAND STATE UNIVERSITY

March 2016

We hereby approve this dissertation

For

Ryan J. Madden

Candidate for the Doctor of Engineering degree

for the Department of

Mechanical Engineering

And

**CLEVELAND STATE UNIVERSITY'S
College of Graduate Studies by**

Dr. Jerzy T. Sawicki
Chair, Department of Mechanical Engineering

Dr. Peter Bubenik
Department of Mathematics

Dr. Stephen F. Duffy
Department of Civil Engineering

Dr. Hanz Richter
Department of Mechanical Engineering

Dr. Dan Simon
Department of Electrical and Computer Engineering

25-March-2016
Student's Date of Defense

“The man in black fled across the desert, and the gunslinger followed.”

-Stephen King, *The Gunslinger*

DEDICATION

I would like to acknowledge that this work would not have been completed without the contribution of many people. First, I would like to thank my advisor, Dr. Jerzy T. Sawicki. Without his time, patience, expertise, and guidance I would have never been able to see this work through to its successful completion. Next, I would like to thank my defense committee for their notes and insights into my work. Additionally, thanks to Dr. Tom Oomen for his correspondence and help in implementing his methodology and getting my work off the ground.

I would be remiss if I did not acknowledge all of the lab members that I have worked with over the years in the Center for Rotating Machinery Dynamics and Control at Cleveland State University for their various contributions. In particular, I would like to recognize Dr. Alex Pesch for being a friend and a mentor for the better part of six years.

Finally, I would like to thank my friends and family for their support over the years. Most notably, I would like to thank my parents for their unwavering support and love without which none of my achievements would be possible.

DEVELOPMENT OF ROBUST CONTROL TECHNIQUES TOWARDS DAMAGE

IDENTIFICATION

RYAN J. MADDEN

ABSTRACT

Robust control techniques have enabled engineers to create uncertain models which are able to describe any differences between the model and experimental system with uncertainties defined as a combination of exogenous inputs and plant perturbations. Subsequently, robust model validation techniques arose to provide a guarantee that the uncertain model is able to recreate all observed experimental data. As a result, the complete model set is robust to any model inaccuracies or external noise. At the same time, the technique of model-based identification was developed in the robust control framework to identify the dynamics resulting from unmodeled or under-modeled components in mechanical systems. The approach controls the nominal model in order to minimize the error between its response and that of the experimentally identified system. The resulting controller estimates the difference in dynamics between the model and actual system, also known as the unmodeled dynamics.

In this work, a damage identification technique is developed which combines model validation and model-based identification for robust control relevant structural health monitoring. The method will both detect the presence of damage and identify the local change in dynamics due to the damage in a robust control framework. As a result, the damage detection will be robust to mismodeling and noise. Additionally, the identified damage dynamics will be defined with an uncertainty bound which will serve the dual purpose of a definition for robust control and a quality estimation of the nominal damage dynamics. The new technique is demonstrated experimentally on a rotordynamic test rig. First, feasibility of the method is verified by the identification of a fully-open seeded crack in a non-rotating shaft. Finally, the precision of the method is demonstrated through identification of a breathing crack in a rotating shaft.

TABLE OF CONTENTS

	Page
ABSTRACT	v
LIST OF TABLES	ix
LIST OF FIGURES	x
CHAPTER	
I. INTRODUCTION	1
1.1 Motivation.....	1
1.2 Model Validation for Robust Control Literature Review	3
1.3 Areas of Application	13
1.3.1 Model-Based Identification	13
1.3.2 Damage Identification.....	16
1.4 Dissertation Structure.....	19
II. ROBUST CONTROL TOOLS	22
2.1 Uncertainty.....	23
2.2 LFT Formulation.....	25
2.3 Structured Singular Value.....	28
2.4 Generalized Structured Singular Value	30
2.5 Summary	32
III. APPLICATION OF ROBUST CONTROL TOOLS TO DAMAGE IDENTIFICATION.....	33
3.1 Robust Model Validation.....	33

3.2 Model-Based Identification	39
3.3 Application to Damage Identification.....	44
3.4 Illustrative Example of Damage Identification.....	46
3.4.1 Experimental Apparatus.....	46
3.4.2 Problem Description	49
3.4.3 Trial 1 Results	52
3.4.4 Trial 2 Results	56
3.4.5 Trial 3 Results	58
3.4.6 Comparison of the Trials	60
3.4.7 Conclusions.....	62
IV. IDENTIFICATION OF A WIRE EDM CUT IN A NON-ROTATING SHAFT	63
4.1 Experimental Apparatus.....	64
4.2 Damage Description.....	68
4.3 Modeling	69
4.4 Simulation of a Non-Rotating Crack	73
4.5 Simulated Damage Identification	75
4.6 Experimental Results	81
4.7 Conclusion	90
V. IDENTIFICATION OF A BREATHING CRACK IN A SHAFT	91
5.1 Introduction to a Breathing Crack.....	92
5.2 The Breathing Crack in Simulation	98
5.3 Illustrative Results from the Simulation	103

5.4 Reviewing the Healthy Model	106
5.5 Damage Identification Problem Description	111
5.6 Simulation Results	113
5.7 Experimental Results	120
5.6 Conclusions.....	130
VI. CONCLUSIONS	131
6.1 Contributions.....	131
6.2 Future Work	134
REFERENCES	137
APPENDIX.....	144
Finite Element Parameters	145

LIST OF TABLES

Table	Page
I. Three-Mass System Parameters	49

LIST OF FIGURES

Figure	Page
1. Concept of the Model Validation Technique.....	2
2. Generic Structure for Identification and Model Validation Problems [2]	4
3. Example of Parametric Uncertainty.....	24
4. Example of Dynamic Uncertainty	25
5. Linear Fractional Transformation Framework.....	26
6. General Framework for Robust Control	27
7. Framework for Robust Performance Analysis.....	27
8. Example Uncertainties Cast as LFTs	28
9. Structure for Robust Stability Analysis	29
10. Implicit LFT Structure	30
11. Robust Model Validation.....	34
12. Model Validation Problem.....	36
13. Frequency Domain Model Validation Problem.....	36
14. Model Reconciliation Control Schematic.....	40
15. Model-based Identification Control Schematic	40
16. Model-Based Identification Schematic with Uncertainties	43
17. Educational Control Products Model 210a Rectilinear Control System	48
18. ECP Model 210a Rectilinear Control System Labeled Schematic [83]	48
19. Three-Mass Healthy System (True).....	50
20. Three-Mass Engineering System Model.....	50
21. Three-Mass System Model with Damage.....	50

22.	Three-Mass Model Validation	51
23.	Three-Mass Model-Based Identification	52
24.	Three-Mass Trial 1 Model Validation Results (Magnitude).....	54
25.	Three-Mass Trial 1 Model Validation Results (Phase).....	54
26.	Three-Mass Trial 1 Identified Damage Dynamics.....	55
27.	Three-Mass Trial 2 Model Validation Results.....	57
28.	Three-Mass Trial 2 Identified Damage Dynamics.....	57
29.	Three-Mass Trial 3 Identified Damage Dynamics.....	59
30.	Three-Mass Identified Damage Comparison	62
31.	Crack Detection Test Rig Photograph (Top) and Schematic (Bottom)	65
32.	Crack Detection Test Rig Dimensions (mm).....	66
33.	Photograph of Active Magnetic Bearing	67
34.	Photograph of Active Magnetic Bearing Coils.....	67
35.	EDM Cut with Location (mm).....	68
36.	Photograph of the Filled EDM Cut.....	69
37.	Finite Element Discretization of Rotor System with Mode Shapes	70
38.	Magnitude Response of the Nominal Model Compared to the Healthy Data	72
39.	Phase Response of the Nominal Model Compared to the Healthy Data	72
40.	Location of Damaged Element in Simulated Damaged Model	74
41.	Comparison of the Simulated and Experimental Non-rotating Crack Responses	74
42.	Simulated Non-Rotating Crack Damage Model Validation Results (Magnitude)	77
43.	Simulated Non-Rotating Crack Damage Model Validation Results (Phase)	77
44.	Simulated Non-Rotating Crack Identified Damage Dynamics (Magnitude).....	79

45.	Simulated Non-Rotating Crack Identified Damage Dynamics (Phase).....	79
46.	Experimental Non-Rotating Crack Damage Model Validation Results (Magnitude).....	83
47.	Experimental Non-Rotating Crack Damage Model Validation Results (Phase) ..	83
48.	Complex Response at 107.9 Hz.....	85
49.	Experimental Non-Rotating Crack Identified Damage Dynamics (Magnitude) ..	86
50.	Experimental Non-Rotating Crack Identified Dynamics (Phase).....	86
51.	Non-Rotating Crack Identified Damage Dynamics Comparison	89
52.	Illustration of Weight Dominance Concept	93
53.	Crack Breathing in a Rotation Cycle	93
54.	Crack Shown in Rotating (η, ζ) and Fixed (x, y) Coordinates	94
55.	Local Coordinates of the Finite Element [84].....	100
56.	Change in Normalized Stiffness due to Mayes and Davies Breathing Model....	102
57.	Simulated Healthy and Cracked Orbits at 1000 rpm	104
58.	Simulated Healthy and Cracked Frequency Spectrum	105
59.	Finite Element Discretization of Rotor System with Mode Shapes	107
60.	Campbell Diagram with Forward Modes (Red) and Backward Modes (Green)	108
61.	Magnitude Response of the Nominal Model Compared to the Healthy Data at 1000 rpm	110
62.	Phase Response of the Nominal Model Compared to the Healthy Data at 1000 rpm	110
63.	Rotor-Bearing Model Layout.....	112
64.	Model Validation Schematic for the Rotating Crack Example	112

65.	Model-Based Identification Schematic for the Rotating Crack Example.....	112
66.	Simulated Rotating Crack Damage Model Validation Results (Magnitude).....	114
67.	Simulated Rotating Crack Damage Model Validation Results (Phase).....	114
68.	Simulated Rotating Crack Damage Model Validation Results Detail.....	117
69.	Simulated Rotating Crack Identified Damage Dynamics (Magnitude).....	118
70.	Simulated Rotating Crack Identified Damage Dynamics (Phase).....	118
71.	Experimental Rotating Crack Damage Model Validation Results (Magnitude)	122
72.	Experimental Rotating Crack Damage Model Validation Results (Phase)	122
73.	Experimental Rotating Crack Damage Model Validation Results Detail	124
74.	Experimental Rotating Crack Damage Model Validation Results Detail 2	125
75.	Experimental Rotating Crack Identified Damage Dynamics (Magnitude).....	126
76.	Experimental Rotating Crack Identified Damage Dynamics (Phase).....	126
77.	Simulated and Experimental Identified Damage Comparison.....	128

CHAPTER I

INTRODUCTION

This chapter reviews the methods which are utilized in this work, namely model validation, model-based identification, and damage identification. First, the motivation of the work is presented, providing a connection between the theory to practical outcomes and how the work will improve on the state-of-the-art. Second, a literature review for model validation for robust control is covered. Next, the areas of application for model validation is introduced, along with a brief literature review of each. Finally, the structure of the dissertation is presented.

1.1 Motivation

In the past quarter century, robust control tools have been developed which allow for engineers to design models that can account for, i.e. are robust to, uncertainties in modeling and experimental application, as well as design controllers which guarantee the stability and performance of these models in the presence of these unknown behaviors. While these innovations have been extremely useful in compensating for well-known issues such as under-modeling, the presence of difficult to model components, and even exogenous disturbances in experimental apparatuses to name a few, they have come at

the cost of requiring additional knowledge from the design engineer. Of particular interest is the design paradox of explicitly defining a bound for a behavior with a definition that is both uncertain in the robust and vernacular sense. As a result, there exists a trade-off between conservativeness of the model set and design performance. Specifically, to ensure stability of the closed-loop system, a model set is required to contain all destabilizing behaviors of the system in the defined bounds. When the design engineer is unsure of the size of these bounds, they can be increased in magnitude in order to ensure safe operation. Unfortunately, this increased safety comes at the cost of reduced closed-loop performance. Model validation for robust control provides a solution to this problem by identifying the robust parameters from experimental data in order to ensure that all destabilizing behaviors are enclosed in the bounds. As a result, the robust system is optimized to be the least conservative, allowing for the best performing closed-loop system possible. The concept for this technique is illustrated below in Figure 1. A comprehensive literature review of the research in model validation for robust control will be covered in the following section.

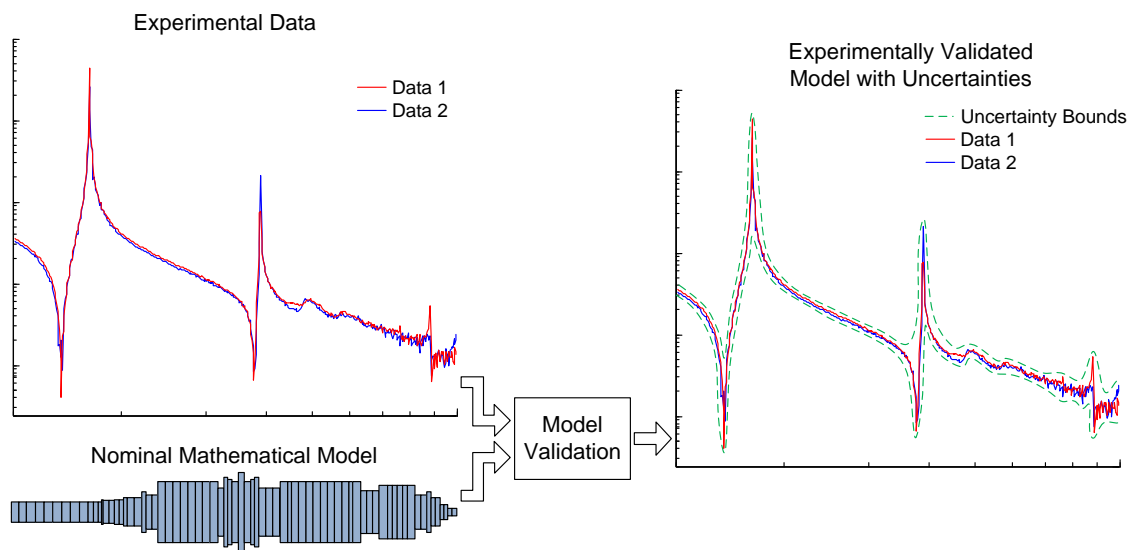


Figure 1 Concept of the Model Validation Technique

The aim of this work is to apply the knowledge of an experimentally validated model in the robust control framework to the fields of model-based identification and damage identification. Utilizing a model set with defined bounds for uncertainties in the model and exogenous disturbances in experimental data will allow for the development of a damage identification technique which is robust to the aforementioned uncertainty and noise. In other words, the damage identification technique will use tools from robust control for analysis in the presence of uncertainty and noise. Conveniently, working in the robust control framework allows for a natural application to model-based identification, as this technique identifies a known difference in dynamics between two systems through utilization of similar robust control tools. Adopting model-based identification as the final step in the damage identification technique allows for a comparison between the healthy and damaged system in order to identify the local change in dynamics due to the damage. Additionally, the uncertainty definition provided by the model validation procedure may be carried over into the model-based identification procedure, allowing for a quality estimate for the identified damage based on the experimental data.

1.2 Model Validation for Robust Control Literature Review

The work of model validation in the robust control framework began with Smith [1] and Smith and Doyle [2] in 1990. The basic premise was to correct models to match experimental data through the inclusion of both additive noise and norm-bounded perturbations. The generic structure for model validation in the robust control framework is shown in Figure 2. In the figure, $P_{\#\#}$ represent the uncertain plant partitions corresponding to the labeled inputs and outputs, y is the measured output, w is the

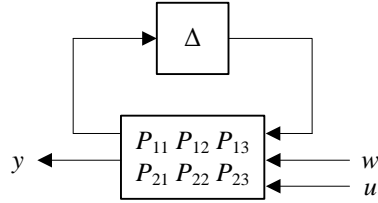


Figure 2 Generic Structure for Identification and Model Validation Problems [2]

unknown inputs from a norm-bounded set, u is the known inputs, and Δ is the uncertainty block. At the time, system identification techniques were able to account for errors between models and data, with any differences accounted for by only additive noise with magnitudes defined using stochastic methods. While these techniques were well-suited for handling disturbances in systems, they would require an update for use with the newly developed robust control theory. This robust control theory allowed for models to be defined including uncertain parameters, with a model set defining a single physical system. As a result, robust control design would take into account all members of the model set in evaluation of performance and stability. This update to control theory necessitated the expansion of model validation to include norm-bounded perturbations. The result would be identification of the robust parameters, i.e. the magnitudes of the noise and norm-bounded perturbations.

In 1992, Smith and Doyle [3] expanded on their previous work by providing an initial solution method to robust model validation as a quadratic optimization. Unfortunately, this solution technique was seen as being too computationally intensive at the time. In addition to providing the initial solution, the authors helped clarify the robust model validation problem defining it as: “Given experimental data and a model with both additive noise and norm-bounded perturbations, is it possible that the model could produce the observed input-output data?” Once this condition is met, validation turns to

an optimization problem seeking the smallest disturbance and norm-bound magnitudes which account for all of the experimental data. Smith, Chu and Fanson [4] later applied the technique to attenuate vibrations in an active truss structure.

Shortly after the initial work of Smith and Doyle, many researchers set out to create more computationally tractable methods for the robust model validation problem. Poolla et al. [5] updated the frequency domain technique of Smith and Doyle to directly apply time-domain input-output data to validate uncertainty models in discrete time. While this paper set the technique for model validation which became the standard for the time, the work stops short of providing a technique for creating a new uncertainty model in the case of invalidation.

Kumar and Balas [6] utilized the structured singular value, a readily available tool in the field of robust control, to construct a bound on the perturbation uncertainty assuming known noise and input disturbance. The authors reached the important conclusion that increasing the size of the model set leads to easier validation of a particular model. As a result, the authors' technique is used to synthesize controllers which significantly outperform more conservative representations of the same system. Kumar and Balas [7] went on to advance the method from single-input single-output to multi-input multi-output systems.

At the same time, Guo and Ljung [8] created an alternative solution approach. The authors provided a statistical technique which worked in the frequency domain to find the model structure that leads to the minimum total error. While this method did not become as popular as the previous techniques, the authors provided a useful interpretation of the errors which occur in any identified model. Similar to the distinction between norm-

bounded perturbations and disturbances, the authors separate the error into the bias error, which occurs due to the model being too simple to describe the system and variance error, due to errors and disturbances in the measurements of the physical system which the model is based on. The authors go on to state, “From a practical point of view, the distinction of the variance and bias errors is immaterial, it is the total error... that matters.” This work remained important as this opinion became a major issue of contention in later works.

Kosut [9] offered a strong counterpoint to Guo and Ljung, as the first paper to address what has come to be known as the ill-posed problem: the trade-off that exists between the size of the norm-bounded perturbations and the bound on the external disturbances. When all possible solutions are plotted with respect to the magnitudes of the norm-bounded perturbations and disturbances, the line of optimal models separates the falsified and unfalsified models, with the unfalsified models appearing above the curve.

This line became known as the trade-off curve as it illustrated the interdependence between the sizes of the perturbations and disturbances. This paper went on to present criteria for selecting the best uncertainty model from the tradeoff curve. The goal then became selecting the model which leads to the best robust performance. As a result, some of the connection to the actual system was lost, which caused the distinction between uncertainties due to the disturbance input and the norm-bounded perturbations to become somewhat arbitrary. The proposed solution for choosing the least-conservative yet stable model is as follows: First, begin by implementing the controller designed with the largest norm-bounded perturbations. Next, make the controller less conservative by reducing the

norm-bounded perturbations until performance objectives are met. Note that robust stability must be maintained at all times.

Various refinements to Smith and Doyle's original techniques were studied which retained the original problem description. First, Smith [10] created a discrete-time frequency domain approach which found the level of the unknown input, noise and disturbance, for each model given a known structured, norm-bounded perturbation. The technique was demonstrated experimentally on a laboratory process control problem. Zhou and Kimura [11] studied the robust identification problem in the discrete-time domain. Next, Rangan and Poolla [12] advanced the technique of Poolla et al. [5] by allowing for a continuous-time plant model. Similarly, Smith and Dullerud [13] applied the problem to validating a continuous-time model with sampled data. The authors went on to apply this technique to a 2-D heating experiment in Dullerud and Smith [14]. Finally, Smith et al. [15] provided a comparison of a few of the contemporary solution methods, including discrete frequency, discrete-time, and sampled-time frameworks.

Chen and Wang [16] were the first to consider the problem of robust model validation for unstructured uncertainties. The authors applied the linear fractional transformation (LFT) to solve for both structured and unstructured uncertainties. This advancement allowed for the validation of models in which the sources of uncertainty were not as explicitly defined, as they are in the structured case. While the lack of uncertainty structure can lead to a more conservative model set, Chen [17] went on to demonstrate that the solution of the validation problem in the LFT framework using a Nevanlinna-Pick boundary interpolation led to a lower level of computational complexity when compared to contemporary approaches. Additionally, the model validation problem could

be defined as a series of problems with respect to each individual frequency point. Alternatively, Toker and Chen [18] applied the structured singular value to the validation of LFT uncertainties, but were not able to arrive at a computationally efficient solution.

Shortly after, Boulet and Francis [19] investigated the robust model validation problem using coprime factor models along with frequency-response data. Similar to Toker and Chen [18] and Kumar and Balas [6], [7] before them, the authors employed the structured singular value to demonstrate that the data fell within the model set. While the method was demonstrated experimentally on a planar two-link flexible robot, it had the drawback of requiring prior knowledge of the factor uncertainty and noise bounds.

The next major advancement in robust model validation began with the work of Chen and Smith [20], [21] who examined validation of an inverted pendulum setup in the closed-loop. Examining the system in the closed-loop provided the added benefits of validating the model in its desired operating state, i.e. operating under robust control, and allowing for validation of a model which is unstable in the open-loop. Dullerud and Smith [22] went on to apply previous model validation methods in the frequency, time, and sampled-data domains to closed-loop systems. Specifically, the authors examined linear feedback systems. Later, Dullerud and Smith [23] extended their work in feedback systems to include examples of nonlinear systems. Interestingly, the authors were able to complete this analysis by using the first time-domain analysis technique developed by Poolla et al. [5].

Concurrently, Newlin and Smith [24] introduced a generalization of the structured singular value μ which guarantees stability with respect to perturbations which are bounded from both above and below. This generalization was developed with application

to model validation in mind, as the authors sought to find a more computationally efficient approach to the robust control model validation problem. As a result, the authors developed, “The real-valued function μ is the inverse of the size of the smallest destabilizing perturbation,” which serves as the foundation for the validation criteria which will be used in this work.

At the same time, works such as Parrilo et al. [25] and Xu et al. [26] investigated the effects of solving the model validation problem in both the time and frequency-domain. Parrilo et al. explained that there exists the possibility for the data to fit well in one of the domains at the expense of the other, so care should be taken in retaining consistency between the two. While Parrilo et al. interpolated between the frequency and time domain data, Xu et al. examined both sets of data simultaneously.

De Callafon [27] revisited the use of coprime factor models first presented in Boulet and Francis [19] with the added benefit of examining the system in the closed-loop. The author emphasized that the application of the model is essential to keep in mind during the validation procedure, as while the model may be valid in the open-loop, it may become invalid in the presence of a controller. This fact necessitated the inclusion of the controller in the validation procedure if the intended use of the model is for control purposes, which is allowed in the applied dual-Youla parameterization of a coprime factor model. De Callafon and van den Hof [28] went on to study closed-loop validation of an unstable model in the presence of a stabilizing controller. As a result, the authors demonstrated the two major strengths of validating in the closed-loop: application to unstable models and validation in the intended operating condition, i.e. robust control.

Crowder and Callafon [29] continued the work of model validation with coprime factor models. The authors advanced the solution technique using the generalized structured singular value first shown in the work of Newlin and Smith [24]. A new invalidation criteria was defined which employs the generalized structured singular value computed over a finite frequency grid. Crowder and Callafon [30] went on to apply the technique to a study of a flexible structure. The results were compared with an open-loop model validation technique and illustrated the advantages of examining the problem in the closed-loop.

All the previous work discussed in this section dealt with deterministic uncertainty representations for model validation in the robust control framework, due to the norm-bounded nature of disturbance and perturbation definitions in robust analysis. Despite this fact, many authors pursued more traditional stochastic explanations for observed errors in modeling. Zhou [31] examined model quality in a probabilistic framework for additive modeling errors. Specifically, the probability that a model set is not falsified by the measured frequency response data is estimated. In the following work, Zhou [32] examined the problem for a coprime factor model. By direct comparison to a stochastic method, the author offered insight into some of the weaknesses of the deterministic validation approaches. For instance, deterministic approaches are only able to supply meaningful conclusions when the noise in the system identification experiment is low. Additionally, the results are highly dependent on the experimental data. The author suggested the use of a stochastic representation in order to allow for an unfalsified probability which, given enough experimental data, is independent of the experimental data.

Later, Liu and Chen [33] expanded on the stochastic view of the model validation problem by investigating a mixed deterministic/probabilistic approach. The idea was to calculate the probability that no uncertainty would be able to fall within the given bound and still match the observed input-output data. This approach would be paired with a deterministic model validation procedure and serve as a secondary evaluation for the validation in a noisy experimental setting. The authors went on to study uncertainty defined by the H_∞ norm in [34].

Advanced applications of the robust parameters identified in the model validation procedures were illustrated by Kosut [35] and De Callafon, Nagamune and Horowitz [36]. Kosut demonstrated the application of model validation to iterative adaptive control. The author presented the approach of repeating robust parameter identification, followed by controller implementation, improving controller performance until the design objective is achieved. Interestingly, the author utilized the solution technique first developed by Poolla et al. [5] in 1994. Callafon, Nagamune and Horowitz applied model validation to dual-stage actuators in order to achieve precision tracking and control.

More recently, Oomen [37] and Oomen and Bosgra [38], [39] revisited the ill-posed problem first discussed by Kosut [9]. As mentioned by Kosut, a trade-off between disturbances and norm-bounded perturbations is present in most robust model validation techniques. Oomen and Bosgra attributed the cause of this ill-posed problem to poorly defined disturbances in deterministic model validation. Particularly, exogenous disturbances are independent of the system input. If the model residual contains elements that are dependent on the input to these systems, then these signals should be defined in the input-output behavior of the system and attributed to norm-bounded perturbations.

Unfortunately, the contemporary deterministic model validation techniques failed to adequately differentiate between these two effects, leading to the ill-posed condition.

Oomen and Bosgra offered a solution to this problem by identifying the uncertainty bound in two steps. First, the solution to the disturbance bound was independently identified. The authors developed a technique for converting a stochastic disturbance model to a deterministic disturbance with an appropriate confidence interval. This advancement allowed for the disturbance bound to be independent of the system input given enough data. Additionally, the technique addressed the issues brought up by Zhou [31], [32], by allowing a stochastic definition for disturbances, which is a more appropriate in realistic situations. Second, the Frequency Dependent Model Validation Optimization Problem is evaluated to identify the least-conservative perturbation bound over a discrete frequency grid. This technique employs the generalized structured singular value to solve the model validation problem, similar to the work of Crowder and de Callafon [29].

Oomen and Bosgra [38] first demonstrated that the disturbance definition becomes more precise when more data points are incorporated. In their next work [39] the authors demonstrated the technique to be convex across a number of frequencies. Later, Oomen, van Herpen and Bosgra [40] successfully applied the technique to precision control of a wafer stage and extended the method to include a coprime factor model, extending the work of de Callafon and Van den Hof [28] to multivariable uncertainty blocks. Oomen et al. [41] investigated model validation for a continuously variable transmission control and Oomen and Meulen [42] reviewed this example with additional insight. Finally,

Oomen et al. [43] combined system identification, model validation and robust control for precision control of a wafer stage.

1.3 Areas of Application

This section presents a pair of methods where the results from model validation for robust control are particularly useful. First, model-based identification seeks to identify difficult to model dynamics which is missing from a nominal engineering model through removing the residual between the model and experimental data. The references covered below illustrate that model-based identification utilizes many of the same robust control tools as the previously covered model validation techniques. Second, damage identification seeks to identify and classify the presence of damage with four levels of descriptiveness. These four levels of damage identification are detection, location, quantification and prognosis [44]. Particularly, vibration-based damage identification approaches will be covered due to their prevalence in non-destructive structural health monitoring. Many of these techniques rely heavily on having a precision model, and guaranteeing the robustness of these models to exogenous disturbances as well as modeling errors carries many inherent benefits.

1.3.1 Model-Based Identification

Maslen, Vazquez, and Sortore [45] presented the technique that came to be known as model-based identification. The idea came about as a way to reconcile well-developed rotating machinery modeling techniques with modern system identification techniques. What resulted was a method which allowed for the use of modeling techniques for well-known components along with experimental data to correct for dynamics which were unknown or otherwise difficult to model. Model-based identification uses the basic

approach of comparing the outputs of the nominal model with the experimental data, and controlling the nominal model in order to minimize any discrepancies between the two. Two important assumptions were employed in this technique. First, the structure of the model, i.e. the interconnection information between the exogenous inputs and outputs and the unmodeled dynamics, is correct, but there is missing dynamics due to the difficult to model components. Second, the location of these difficult to model components was known. As a result, the controller was applied only at the location(s) of any components which present difficulties in modeling. Therefore, the controller estimated the dynamics which were missing from the model. The initial work of Maslen, Vazquez and Sortore [45] illustrated the technique on a few practical rotordynamic examples, specifically, unmodeled dynamics due to interactions with a motor coupling and the effects of a seal. Later, Vazquez et al. [46] applied the technique to identify the dynamics of magnetic bearing journals.

Wang and Maslen [47] advanced the technique by introducing the structured singular value to solve the model reconciliation problem. This application of a common tool in the field of robust control allowed for the addition of a quality estimate to the identified missing dynamics. Additionally, the authors directly utilized experimental frequency response data along with simulated frequency response data of the model. Previously, a model was estimated for the data, which added an additional estimation, naturally resulting in less precise results. The study illustrated these innovations in a simulation for identification of the parameters of tilting pad bearings. Additional insight into this method is provided in Wang [48].

Later, Wang, Pettinato, and Maslen [49] compared the effect of utilizing direct measurements in place of model estimation. Their conclusions followed those of Wang and Maslen [47], and illustrated that more detailed information may be found through application of the data directly by the identification of the support dynamics in a rotor-support setup. Next, the authors investigated the uncertainties on the same rotor-support setup [50]. The authors presented the idea that uncertainties in the system model are carried over into the missing dynamics through the model-based identification process. By defining the uncertainties in a LFT, μ -analysis may be performed to bound the uncertainties of the missing dynamics.

Sawicki and Madden [51] applied model-based identification to the identification of the changes in dynamics of an experimental rotor due to the presence of a transverse crack. This work was the first to apply the technique to damage identification. More detail on the derivation of the technique may be found in Madden [52]. Later, Madden and Sawicki [53] investigated the use of model-based identification to extract local changes in dynamics resulting from experimentally updating the finite element model of a high-speed machining spindle. The aim of the paper was to capture the dynamics of regions with known modeling difficulties, specifically, the tool holder, active magnetic bearing rotors, and motor rotor. The paper illustrated that model-based identification utilizing μ -synthesis was capable of updating a model with multiple, difficult to model stations to a high degree of accuracy.

In later work, Madden, Sawicki, and Pesch [54] applied the model-based identification technique to determine the local change in dynamics brought on by a large cut. The technique was expanded to include detection of the change in dynamics, providing an

application to damage identification. The authors went on to apply the technique to a wire electrical discharge machining (EDM) cut in a shaft with the addition of locating the source of the damage [55]. Lastly, the damage identification technique was applied to a crack in a rotor [56]. A complete derivation of these damage identification techniques will be covered in this dissertation.

1.3.2 Damage Identification

Vibration-based damage identification methods are a popular choice due to their ability to identify the damage based on global properties of the system. Such methods are based on the idea that damage induces changes in the physical properties of a system, leading to changes in the modal properties of the system. These methods are classified into four major categories: natural frequency-based, mode shape-based, curvature mode shape-based, and methods using mode shapes and natural frequencies [57]. These methods can be further broken down into model-based methods or purely response-based methods, where the former requires an accurate engineering model of the system, whereas the latter attempts to identify the damage based only on experimental response data.

Natural frequency-based methods identify damage using the changes in natural frequencies. The primary benefit of this method is that the natural frequencies are a global property, meaning that the values will be consistent regardless of sensor and actuator location. As a result, a single sensor-actuator pair is required for these techniques. The forward problem involves predicting the changes in natural frequency of a structure based on damage location and severity. Liang, Hu and Choy [58] developed a relationship between natural frequency changes and crack location and depth for simply

supported and cantilever beams by utilizing a massless rotational spring to represent the local change in flexibility due to a crack. Morassi [59] demonstrated that the ratios of natural frequency changes of different modes are independent of crack severity, and are therefore useful in locating the damage in beams.

The basis for the inverse natural frequency problem is determining the damage location and size based on the experimental natural frequency data. Liang, Choy, and Hu [60] used multiple natural frequencies along with the variation of stiffness as a function of assumed damage location to identify possible locations of the damage. The authors were able to detect a single crack in a uniform beam under simply supported or cantilever boundary conditions using three modes. More recently, Messina, Williams and Contrusi [61] extended the technique to include multiple damage locations by developing the Multiple Damage Location Assurance Criterion, based on the sensitivity of each natural frequency to damage in each location. The main limitation of frequency-based methods is that damage with different severities at different locations may produce identical changes in the first few natural frequencies, leading to non-unique solutions.

Mode shape-based methods sought to overcome the limitations of the natural frequency-based techniques by utilizing local information. Traditional mode shape methods identified damage using the mode shape change from the healthy to damaged structures. Shi, Law and Zhang [62] extended the Multiple Damage Location Assurance Criterion by examining incomplete measured mode shapes. Lee et al. [63] utilized neural networks and the change in mode shape components before and after damage. The addition of neural network decision making allowed the authors to mitigate the effects of errors in the healthy finite element model.

Modern mode shape methods attempt to utilize modern signal processing techniques in order to identify damage using only experimental data from the damage system. Liew and Wang [64] demonstrated the method by applying a wavelet transform to mode shape data in order to detect the presence of damage through irregularity in the mode shape. The authors were successful in identifying a crack in a simply supported beam. Later, Hadjileontiadis, Douka, and Trochidis [65] located and determined the size of a crack in a cantilever beam using only the first mode shape. While the mode shape methods offered additional accuracy over the natural frequency approaches, this came at the cost of requiring additional sensors. In fact, the precision of the measured mode shapes is directly related to the number of output sensors employed. Obviously, complications in these methods could arise in predicting damage at locations where a sensor is not readily available.

The mode shape curvature, or the first derivative of the mode shape, has been investigated to add additional sensitivity to the mode shape-based methods. Once again, the mode shape curvature method can be divided into traditional, model-based approaches and those which seek to use only experimental data in the analysis. Pandey, Biswas and Samman [66] first investigated the mode shape curvature. The authors demonstrated that changes in the curvature mode shapes are located in the vicinity of the damage. Damage was accurately predicted using finite element analysis and the experimental data for both a cantilever and simply supported beam. Later, Wahab and De Roeck [67] successfully applied the change in modal curvatures to a concrete bridge for damage identification. The technique was advanced through the development of the

curvature damage factor, which tracked the difference in curvature mode shapes for all modes.

Examples of signal processing approaches which sought to identify damage without any modeling information include Ratcliffe [68] and Kim, Park, and Voyiadjis [69]. First, Ratcliffe demonstrated a finite difference approximation of Laplace's differential operator to identify the location of damage. Later, Kim, Park, and Voyiadjis were able to detect, locate, and identify the severity of damage by transforming the problem into a wavelet domain. Similar to the methods that directly utilized the mode shapes, these techniques were shown to be sensitive to the density of the measurement grid.

Lastly, methods were proposed which utilized both the natural frequency and mode shape data. Pandey and Biswas [70] investigated the viability of tracking changes in the stiffness matrix, which is the inverse of the flexibility matrix, to detect and locate damage in a wide-flange steel beam. More recently, Ren and Roeck [71] developed a method which employed an element damage index, defined the ratio of the damaged stiffness to the healthy stiffness of each element. When combined with the damaged mode shapes, this information can be used to find the damage location and severity. In the companion paper [72], Ren and Roeck verified their method on a reinforced concrete beam.

1.4 Dissertation Structure

This work develops model validation for robust control towards a damage identification procedure. To complete this objective, the dissertation proceeds in the following manner:

In Chapter 2, the robust control tools which will be employed in the damage identification technique are introduced. The tools which will be defined include:

uncertainties, the linear fractional transformation, and the structured singular value. The aim of this chapter will be to provide the necessary background required to understand the developed damage identification procedure, as well as provide resources in case the reader should require more information.

In Chapter 3, the framework for the application of the robust control tools to damage identification will be developed. First, the robust model validation technique will be introduced which makes use of the concepts of uncertainties, the LFT structure, and the generalized structured singular value. Next, the model-based identification technique will be presented, which utilizes the LFT structure and the structured singular value to identify a difference in dynamics between a model and experimental data. Next, these two techniques will be combined into a damage identification technique which is robust to external disturbances or uncertainties in the model. Additionally, a simple example is presented to illustrate the technique.

In Chapter 4, the first of two experimental examples of the damage identification technique is presented. The example of an identification of a wire EDM cut in a non-rotating shaft will serve two functions. First, the example illustrates the effectiveness of the damage identification technique in a laboratory setting. Second, the non-rotating shaft may be seen as a generic structure, as it will under the influence of any rotordynamic effects.

In Chapter 5, the identification of a breathing crack in a shaft will be covered. This example will demonstrate the damage identification procedure on a practical damage source which presents difficulty in detection, due to its lower impact on the system dynamics.

In Chapter 6, the contributions of the work will be summarized along with possible directions for future research.

CHAPTER II

ROBUST CONTROL TOOLS

Robust control techniques began in the 1970s in response to optimal control techniques being unable to meet control requirements in some practical systems. For example, Athans et al. [73] studied the application of LQG control on an F-8C Crusader aircraft, which did not meet performance requirements. The authors were critical of the shortcomings of the approach, concluding that the control design contained, “certain theoretical weaknesses... as well as the need for using common sense pragmatic techniques to modify the design based on ‘pure’ theory.” Researchers were able to recognize that inaccurate modeling, as well as a lack of concern for the consequences due to these inaccuracies, was the primary cause for failures in optimal control [74].

Safonov and Athans [75] were the first to adopt the term *robust* to describe quantitative measures of a system’s performance in the presence of modeling errors, otherwise known as uncertainties in modeling. Safonov [76] went on to introduce the diagonal structure for such uncertainties in which the uncertainties are extracted from the system as part of the robust analysis. Later, Doyle [77] would expand this definition to structured uncertainties, which provided a unified structure for both robustness performance analysis, and robust stability analysis, with the structured singular value μ .

Zames [78] developed robust H_∞ control, the first widely used optimal robust control synthesis technique. While this technique was able to solve the problem of uncertainty in optimal controller design, it was not able to analyze structured uncertainties. Finally, application of structured uncertainties to robust H_∞ control gave rise to μ -synthesis control design. Balas [79] provided experimental examples to demonstrate the effectiveness of controllers designed using μ -synthesis.

This chapter will serve as an introduction to the robust tools which will be employed in the damage identification technique. First, the concept of uncertainties in modeling will be presented along with a basic mathematical description for both parametric and dynamic uncertainties. Next, the LFT will be explained along with its application to structured uncertainties and robust control analysis. Finally, the tools for robust stability analysis, namely the structured singular value and its generalized form will be defined and derived. The aim of this chapter is to present the background for all of the tools which will be employed in the robust damage identification procedure.

2.1 Uncertainty

Despite the use of advanced modeling techniques, any model of a physical system still remains inexact. As a result, the field of robust control arose to allow for the design of controllers which are resilient to this imperfection. The differences which cause the mismatching between the physical system and the model are known as model uncertainty.

Model uncertainty may come from a variety of sources. The most general source is parameters in the model which are only approximately known, or whose value is incorrectly defined. Also, measurement of the physical system may contain exogenous

disturbances either from the environment or from imperfections in the measurement device. Additional sources of uncertainties come from dynamics which are left out of the model, or unmodeled. A few examples include a linear model which is an approximation of nonlinear behaviors, and a model with reduced order for ease of control loses information due to the nature of the approximation [80].

The two primary representations for uncertainties are parametric and dynamic. Parametric uncertainties are defined as an unknown value of a specific parameter of the model. For example, consider the stiffness of a spring. While the stiffness is modeled as a linear behavior, it is possible that the stiffness of the spring changes due to the deflection of the spring. Parametric uncertainties provide the ability to define a range of values for the stiffness. To illustrate, an uncertain stiffness is defined in Eq. 2.1 and the block diagram is shown below in Figure 3. The stiffness k is defined by the nominal, i.e. not uncertain, value k_{nom} , the weight of the uncertainty w_k , and the uncertain parameter Δ , which is a real number with $|\Delta| \leq 1$.

$$k = k_{nom} + w_k \Delta \quad (2.1)$$

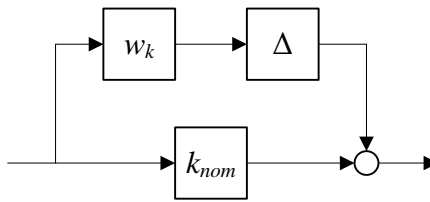


Figure 3 Example of Parametric Uncertainty

Dynamic uncertainties are defined as an unknown behavior which acts on the model due to missing dynamics. Therefore, the uncertainty is not tied to a specific source as with the parametric type. Instead the uncertainty is applied to either the input or output of the system. Additionally, the weight of the uncertainty is defined as frequency-dependent.

For example, model reduction is a common source of dynamic uncertainty. A model's order may be reduced in order to allow for the design of lower order controllers, which are easier to implement due to reduced processing time. Clearly, this uncertainty is unable to be tied directly to one source or parameter, which necessitates the use of dynamic uncertainties. Such an example of dynamic uncertainty is defined in Eq. 2.2 and illustrated in Figure 4. The plant P is defined by the nominal model M and the input multiplicative uncertainty Δ , which is weighted by $w_i(\omega)$. For dynamic uncertainties, the weight is defined as frequency dependent and the uncertainty is a complex number with $\|\Delta\|_\infty \leq 1$, where $\|\cdot\|_\infty$ is defined as the peak value of the maximum singular value across all frequencies [80].

$$P = M(1 + w_i(\omega)\Delta) \quad (2.2)$$

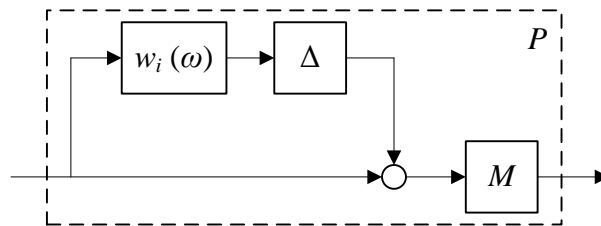


Figure 4 Example of Dynamic Uncertainty

2.2 LFT Formulation

The linear fractional transformation (LFT) is a widely used tool in robust controls. The widespread use is due to the fact that LFTs are important for both defining uncertainties in a common structure and evaluating the stability and performance analysis of robust systems in applications of the structured singular value μ . Consider a plant P which is partitioned:

$$P = \begin{bmatrix} P_{11} & P_{12} \\ P_{21} & P_{22} \end{bmatrix} \quad (2.3)$$

The upper and lower LFTs, F_u and F_l , respectively, are defined by the following equations [81]:

$$F_u(P, \Delta_u) = P_{22} + P_{21} \Delta_u (I - P_{11} \Delta_u)^{-1} P_{12} \quad (2.4)$$

$$F_l(P, \Delta_l) = P_{11} + P_{12} \Delta_l (I - P_{22} \Delta_l)^{-1} P_{21} \quad (2.5)$$

The block diagrams for the LFT formulations are shown below in Figure 5:

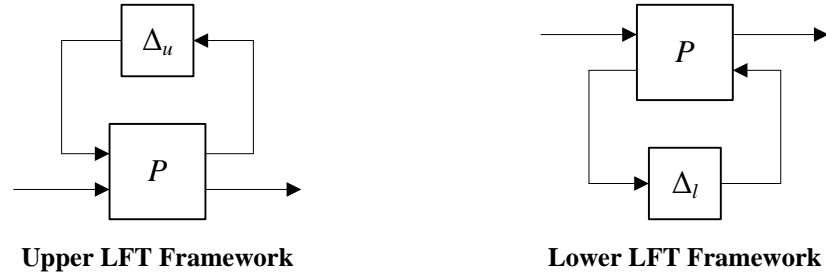


Figure 5 Linear Fractional Transformation Framework

Note that the functions F_u and F_l are transfer matrices between the input and output signals shown in Figure 5.

As previously mentioned, the LFT is an important tool in the analysis of uncertainties. Specifically, LFTs are useful in handling a particular form of uncertainties, known as structured uncertainties. An uncertainty is said to be structured if Δ is defined by [80]:

$$\Delta = \text{diag} \{ \Delta_i \} = \begin{bmatrix} \Delta_1 & & & \\ & \ddots & & \\ & & \Delta_i & \\ & & & \ddots \end{bmatrix} \quad (2.6)$$

with Δ_i defining each source of uncertainty, either parametric or dynamic. Presenting uncertainties in a common form leads to a general framework for robust control, where K is any controller interconnected to the uncertain plant P perturbed by Δ :

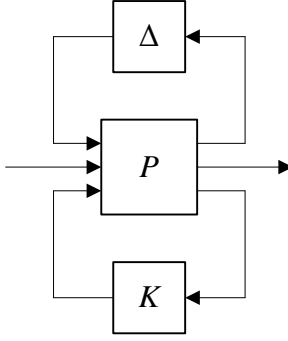


Figure 6 General Framework for Robust Control

As shown, the system is defined by the combination of an upper LFT between the plant and the uncertain perturbations and a lower LFT between the plant and the controller. If a new system is defined which includes the controller, the new closed-loop system N may be defined as:

$$N = F_l(P, K) = \begin{bmatrix} N_{11} & N_{12} \\ N_{21} & N_{22} \end{bmatrix} \quad (2.7)$$

leading to the general framework for robust performance analysis shown below.

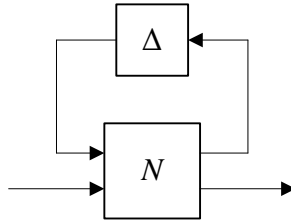


Figure 7 Framework for Robust Performance Analysis

To further illustrate the use of structured uncertainties, the two uncertainty examples from the previous section are cast as upper LFTs, shown below in Figure 8. To check the solution, solve for each of the LFTs, where Eq. 2.8 is for the spring parametric uncertainty example and Eq. 2.9 is for the input dynamic uncertainty example:

$$F_u = P_{22} + P_{21}\Delta(I - P_{11}\Delta)^{-1}P_{12} = k_{nom} + w_k\Delta \quad (2.8)$$

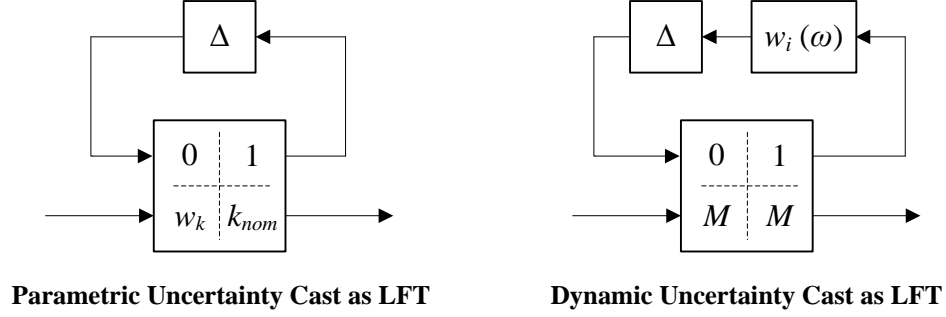


Figure 8 Example Uncertainties Cast as LFTs

$$F_u = P_{22} + P_{21}\Delta(I - P_{11}\Delta)^{-1}P_{12} = M + M\Delta w_i = M(1 + w_i\Delta) \quad (2.9)$$

The LFT form is able to handle multiple uncertainties and is apt for structured uncertainties. The significance of this property will be demonstrated in the next chapter, which covers the application of robust control tools to the robust damage identification technique.

2.3 Structured Singular Value

First introduced by Doyle [77], the structured singular value μ was developed to analyze the stability and performance of systems with structured uncertainties. This value will be utilized as the necessary and sufficient condition for robust stability. The μ value is defined as [80]:

$$\mu(M) = \frac{1}{\min_{\Delta} \{\bar{\sigma}(\Delta) \mid \det(I - M\Delta) = 0 \text{ for structured } \Delta\}} \quad (2.10)$$

In other words, μ answers the question: What is the smallest perturbation Δ , in terms of the maximum singular value $\bar{\sigma}$, which destabilizes the system? If $\mu < 1$ the uncertainty would need to be greater than one for the system to become unstable. If $\mu > 1$ the system could become unstable with an uncertainty magnitude less than one. Therefore, a μ -value less than one guarantees stability for a system containing any combination of parametric

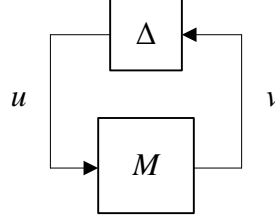


Figure 9 Structure for Robust Stability Analysis

and dynamic uncertainties, and a stable plant M . Note that $\mu = 1$ is classified as marginally stable, and is typically avoided.

The framework for robust performance analysis in Figure 7 can be rearranged into the framework for robust stability in Figure 9 if $M = N_{11}$. This framework leads to the definition of μ as the necessary and sufficient condition for robust stability. Given the structure of the M-loop, the Nyquist criteria define the system as stable as long as [80]:

$$\det(I - M\Delta(j\omega)) \neq 0, \quad \forall \omega, \forall \Delta \quad (2.11)$$

Robust analysis assumes that the nominal system M is stable; therefore the focus of robust stability is on the size of the uncertainty perturbation Δ which causes the system to become unstable. The derivation leads to the structured singular value definition presented above.

Further insight into the structured singular value is offered by returning to the framework for robust performance analysis shown in Figure 7. First, recall that M in the robust stability analysis diagram shown in Figure 9 relates the connection between the uncertainty output and the uncertainty input, analogous to N_{11} in the upper LFT in Figure 7. Solving this upper LFT gives:

$$F_u(N, \Delta) = N_{22} + N_{21}\Delta(I - N_{11}\Delta)^{-1}N_{12} \quad (2.12)$$

Assuming stability of the nominal system and the uncertainty block, the stability of the uncertain system is completely dependent on the interaction between the uncertainty output and input N_{11} , which can be solved with μ .

2.4 Generalized Structured Singular Value

The generalized structured singular value was developed to allow for an extension of the structured singular value to implicitly defined systems, meaning that the output is set to zero, and denoted by $\bar{\mu}$, such as the LFT shown in Figure 10. The formal definition is given by Paganini and Doyle as [82]:

$$\bar{\mu}_{\bar{\Delta}}(M, N) := \left(\min_{\bar{\Delta}} \{ \bar{\sigma}(\bar{\Delta}) \mid \text{Ker} \begin{pmatrix} I - \bar{\Delta}M \\ N \end{pmatrix} \neq 0 \text{ for structured } \bar{\Delta} \} \right)^{-1} \quad (2.13)$$

The above equation holds for complex matrices M and N of appropriate sizes, which will be defined later. Simply put, the generalized structured singular value looks for the smallest uncertain perturbation $\bar{\Delta}$, evaluated by the maximum singular value $\bar{\sigma}$, which provides a nontrivial solution to the implicit LFT in Figure 10.

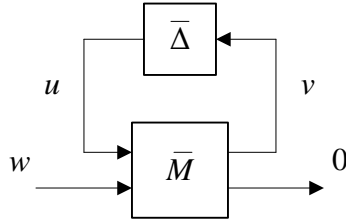


Figure 10 Implicit LFT Structure

Derivation of the generalized structured singular value begins with the implicit LFT structure, shown above and described by the system of equations [37]:

$$u = \bar{\Delta}v \quad (2.14)$$

$$v = \bar{M}_{11}u + \bar{M}_{12}w \quad (2.15)$$

$$0 = \bar{M}_{21}u + \bar{M}_{22}w \quad (2.16)$$

Substitute Eq. 2.15 into Eq. 2.24 to eliminate v :

$$u = \bar{\Delta}\bar{M}_{11}u + \bar{\Delta}\bar{M}_{12}w \quad (2.17)$$

$$0 = \bar{M}_{21}u + \bar{M}_{22}w \quad (2.18)$$

From Eq. 2.18, with $\bar{X}_{22} = \bar{M}_{22}^{-1}$:

$$w = -\bar{X}_{22}\bar{M}_{21}u \quad (2.19)$$

Substituting 2.19 into 2.17 and 2.18 to eliminate w :

$$u = \bar{\Delta}\bar{M}_{11}u - \bar{\Delta}\bar{M}_{12}\bar{X}_{22}\bar{M}_{21}u \quad (2.20)$$

$$0 = \bar{M}_{21}u - \bar{M}_{22}\bar{X}_{22}\bar{M}_{21}u \quad (2.21)$$

Rearranging and factoring out u gives:

$$(I - \bar{\Delta}(\bar{M}_{11} - \bar{M}_{12}\bar{X}_{22}\bar{M}_{21}))u = 0 \quad (2.22)$$

$$(\bar{M}_{21} - \bar{M}_{22}\bar{X}_{22}\bar{M}_{21})u = 0 \quad (2.23)$$

Assuming the non-trivial solution, i.e. $u \neq 0$, the problem becomes checking if there is a zero solution to the factored portions of Equations 2.22 and 2.23:

$$\text{Ker} \begin{bmatrix} I - \bar{\Delta}(\bar{M}_{11} - \bar{M}_{12}\bar{X}_{22}\bar{M}_{21}) \\ \bar{M}_{21} - \bar{M}_{22}\bar{X}_{22}\bar{M}_{21} \end{bmatrix} \neq 0 \quad (2.24)$$

Ker refers to the kernel, a set of all vectors which map to the zero vector. By looking for a nonzero kernel, the solution checks if there is a configuration of the system defined by \bar{M} and $\bar{\Delta}$ which results in the zero vector solution. Therefore:

$$M = \bar{M}_{11} - \bar{M}_{12}\bar{X}_{22}\bar{M}_{21} \quad (2.25)$$

$$N = \bar{M}_{21} - \bar{M}_{22}\bar{X}_{22}\bar{M}_{21} \quad (2.26)$$

Returning to the definition for $\bar{\mu}$ and replacing the matrices M and N provides the more practical expression:

$$\bar{\mu}_{\bar{\Delta}}(\bar{M}_{11} - \bar{M}_{12}\bar{X}_{22}\bar{M}_{21}, \bar{M}_{21} - \bar{M}_{22}\bar{X}_{22}\bar{M}_{21}) \quad (2.27)$$

Therefore, the generalized structured singular value will seek to find the smallest $\bar{\Delta}$ which provides the 0 output for the defined input w as shown in Figure 10.

2.5 Summary

This chapter provides an introduction to three robust control tools which will be utilized in the robust damage identification procedure which will be developed in this work. Namely, the chapter introduces uncertainty, the linear fractional transformation, and the structured singular value. Additionally, the generalized structured singular value, an alternative definition for implicitly defined systems, is derived. Each of these tools will be utilized in the development of the robust damage identification procedure in Chapter 3.

CHAPTER III

APPLICATION OF ROBUST CONTROL TOOLS TO DAMAGE IDENTIFICATION

This chapter will explain how the robust control tools introduced in the previous chapter will be applied to the damage identification technique developed in this work. First, the robust model validation technique will be presented which combines the concepts of uncertainties, the implicit LFT structure, and the generalized structured singular value to evaluate whether or not an uncertain model can explain experimental data. Next, the model-based identification technique will be introduced which combines the LFT structure and uncertainties to identify the dynamics which are missing between the engineering model and the true system. Finally, the combination of these two techniques to a robust damage identification technique is developed.

3.1 Robust Model Validation

As mentioned in Chapter 1, the field of robust model validation developed to provide an assurance of quality for an uncertain model. The essence of the model validation problem is confirming that the system described by the mathematical model accurately

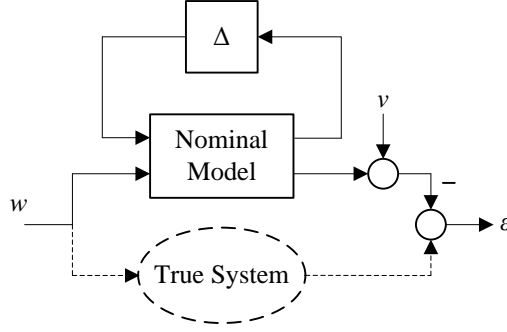


Figure 11 Robust Model Validation

represents the experimental data. Specifically, the technique looks to answer the question: “Does the bounded set include a perturbation and disturbance which account for each measured input-output data?” This concept is illustrated above in Figure 11. In the figure, the engineering model is comprised of the nominal model (created through standard engineering practices), model uncertainty Δ , and additive noise v . The model’s response to a known experimental input w is compared to the true system response, leading to the residual ε . In order for the model to not be invalidated, there must be a combination of uncertainty and noise which result in zero residual for all inputs in question. In other words, the uncertain model must be shown to enclose all observed experimental input-output data. The derivation follows the form first presented in Oomen [37].

The first step in developing the robust model validation problem is to define the uncertain model output:

$$z_e = F_u(M_e, \Delta)w + v \quad (3.1)$$

where z_e is the uncertain model output and M_e is the nominal model, which is obtained using traditional engineering techniques. This definition leads to the solution for the residual ε :

$$\varepsilon = z_e - F_u(M_e, \Delta)w - v \quad (3.2)$$

where z_t is the response of the true system to the same input. Naturally, for a model to be not invalidated the residual must be equal to zero.

At this point, it is necessary to expand on the definitions of the parametric uncertainty Δ and noise v . Due to the nature of the model validation problem, i.e. the question of whether the uncertain system encloses the observed experimental behavior, requires access to the size of the uncertainties. For this reason, the parametric uncertainties will be defined by the structured uncertainty Δ_u scaled by the bound γ and the noise will also be represented as a structured uncertainty Δ_v , scaled by the bound v . Additionally, the true system is expanded to the true plant M_t , which is disturbed by v_{true} . The resulting expanded model validation problem is shown in Figure 12.

While this form contains all of the information required for solution, the structure will be transformed in order to employ the standard robust control tools introduced in the previous chapter. First, M_e is divided into M_{e11} , M_{e12} , M_{e21} and M_{e22} corresponding to the inputs and outputs presented in Figure 12. The problem will be solved in the frequency domain at each frequency $\omega_i \in \Omega^{id}$. Therefore, the signals w , z_e , z_t and v will be evaluated at each frequency as the complex gains W , Z_e , Z_t and V , respectively. Finally, the uncertainties Δ_u and Δ_v are isolated to allow the model validation problem to be cast as an LFT. The complete system is shown in Figure 13. The resulting model validation problem is defined by the equation:

$$F_u(\bar{M}, \bar{\Delta}) = 0 \quad (3.3)$$

where:

$$\bar{M} = \left[\begin{array}{cc|c} 0 & 0 & V \\ 0 & \gamma M_{e11} & -M_{e12}W \\ \hline -1 & \gamma M_{e21} & Z_t - M_{e22}W \end{array} \right] \quad (3.4)$$

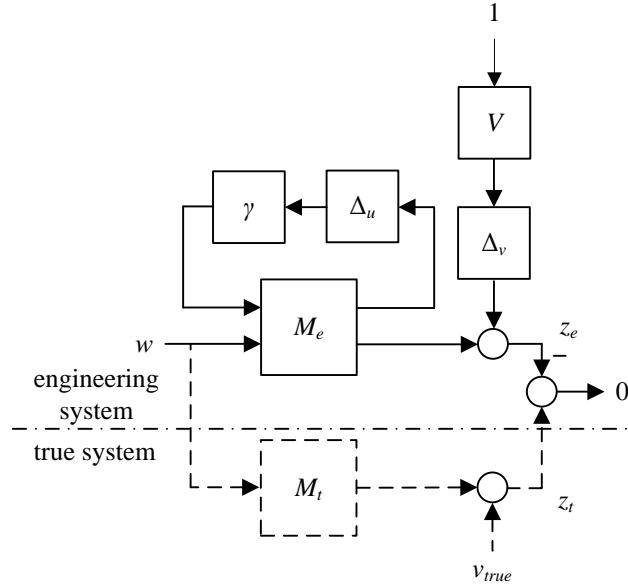


Figure 12 Model Validation Problem

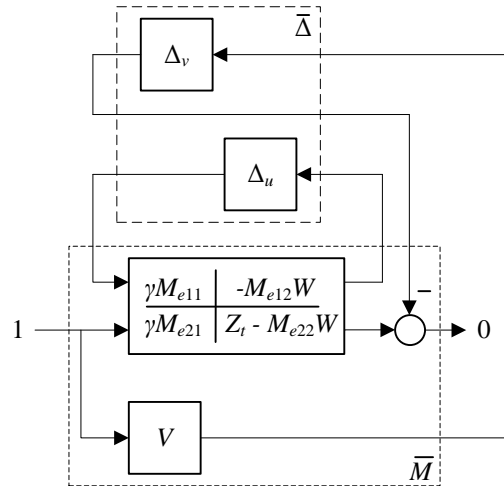


Figure 13 Frequency Domain Model Validation Problem

$$\bar{\Delta} = \begin{bmatrix} \Delta_v & 0 \\ 0 & \Delta_u \end{bmatrix} \quad (3.5)$$

Therefore $\bar{\Delta}$ is structured.

As indicated by Equation 3.3, this structure is in the same form as the implicit LFT shown in Figure 10, as denoted by the over-bars. As a result, the model validation criteria is evaluated using the generalized structured singular value $\bar{\mu}_{\bar{\Delta}}$:

$$\bar{\mu}_{\Delta}(\bar{M}_{11} - \bar{M}_{12}\bar{X}_{22}\bar{M}_{21}, \bar{M}_{21} - \bar{M}_{22}\bar{X}_{22}\bar{M}_{21}) > 1 \quad (3.6)$$

where \bar{M}_{11} , \bar{M}_{12} , \bar{M}_{21} , and \bar{M}_{22} are the partitions of \bar{M} and \bar{X}_{22} is the inverse of \bar{M}_{22} . When $\bar{\mu}_{\Delta} > 1$, the relationship in Figure 12 holds for the maximum singular values $\bar{\sigma}(\Delta_u) < 1$ and $\bar{\sigma}(\Delta_v) < 1$, which are consistent with the definition for structured uncertainties presented in the previous chapter. Particularly, the value of $\bar{\mu}_{\Delta}$ indicates the size of the uncertainties which are required to recreate the implicit condition of the LFT output equaling zero. For example, if $\bar{\mu}_{\Delta} < 1$, the magnitude of one or more of the uncertainties needs to be larger than one in order to produce the zero residual depicted in Figure 12. Conversely, if $\bar{\mu}_{\Delta} > 1$, the magnitude of the uncertainties may be under one and produce the zero residual. Therefore, the bounded model set is guaranteed to be able to recreate the experimental input-output data if and only if $\bar{\mu}_{\Delta} > 1$, leading to an experimentally not invalidated model.

The model validation process incorporating the frequency domain model validation problem is implemented in two steps. First, the noise v is bound by V . This may be completed in a few ways. Oomen and Bosgra [38], [39] developed a technique that employs information about the covariance of the experimental output to create a stochastic bound for the noise, which is then converted to a deterministic representation. However, in this work, the model will be fit with a noise bound scaled to match the experimental data. Manual tuning of the noise is completed by adding a weighted random white noise to the nominal model and adjusting the weight until the level of the noise floor is consistent with the system identification data. This noise is assumed to be

uniform across all frequencies and is attributed to the experimental process in particular, not to the test setup in general.

Second, the model validation criteria in Equation 3.6 is solved as an optimization problem. To begin, define the Model Validation Optimization Problem (MVOP):

Definition 3.1 (MVOP) Let the uncertain model defined by Equation 3.1, noise bound v , and measurements w and z_t be given. Therefore, the MVOP amounts to determining the minimum magnitude of the bound γ for structured Δ_u , resulting in a residual of zero.

Next, the MVOP definition is extended to the Frequency Domain Model Validation Optimization Problem (FDMVOP):

Definition 3.2 (FDMVOP) Let the uncertain model defined in Equation 3.1, noise bound V , and measurements $W(\omega_i), Z_t(\omega_i)$, and $\omega_i \in \Omega^{id}$ be given. Therefore, the FDMVOP amounts to determining the minimum value of $\gamma(\omega_i)$ for structured Δ_u , resulting in a residual of zero.

The FDMVOP is evaluated at each frequency utilizing the structured singular value defined in Equation 3.6, evaluating the system shown in to Figure 13. In other words, γ is checked against the measurements W and Z_t with the Frequency Domain Model Validation Decision Problem (FDMVDP), defined as:

Definition 3.3 (FDMVDP) In the FDMVDP, the model is not invalidated if and only if $\bar{\mu}_{\bar{\Delta}}(\bar{M}_{11} - \bar{M}_{12} \bar{X}_{22} \bar{M}_{21}, \bar{M}_{21} - \bar{M}_{22} \bar{X}_{22} \bar{M}_{21}) > 1$ where \bar{X}_{22} is the inverse of \bar{M}_{22} .

As a result, the FDMVOP amounts to finding the minimum $\gamma(\omega_i)$ which satisfies the FDMVDP at each frequency ω_i . This may be accomplished using any optimization procedure. For this work, a bisection algorithm, which repeatedly halves an interval to

arrive at the optimal solution, is employed. The termination criteria is a sufficiently small sensitivity of the γ value.

A strength of this method is that the validation problem lends itself to being solved by commercially available robust control tools. In particular, MATLAB's *mussv* function is capable of solving the generalized structured singular value problem which is the basis for the FDMVDP.

3.2 Model-Based Identification

This section will explain how the model validation technique is applied to model-based identification to add a quality estimate in the form of an inherited uncertainty bound to the extracted unmodeled dynamics. To begin, the technique of model-based identification, which is utilized for the identification of a known difference in dynamics, is reviewed. The first control schematic, sometimes referred to as model reconciliation in the literature is shown in Figure 14 [45]. In the figure, *true_{sys}* is the true system identified from experimental data, *eng_{sys}* is the nominal engineering model created from traditional techniques, w is the external input to the system, u is the control force, y is the output to the controller K , z_e is the output of the engineering system, z_t is the output of the true system, e is the error or difference between the true and engineering system responses, and K is the controller which attempts to drive the error e to zero.

As shown, model-based identification causes the engineering system response to match the true system response by creating a controller K which minimizes the difference between the two outputs due to a known input. This method is based on two assumptions. First, the structure of the engineering model is correct. Second, there are behaviors which

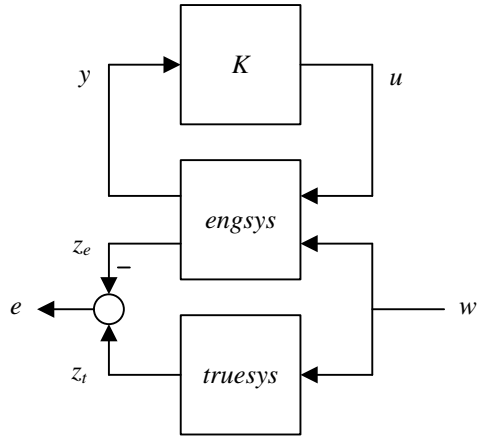


Figure 14 Model Reconciliation Control Schematic

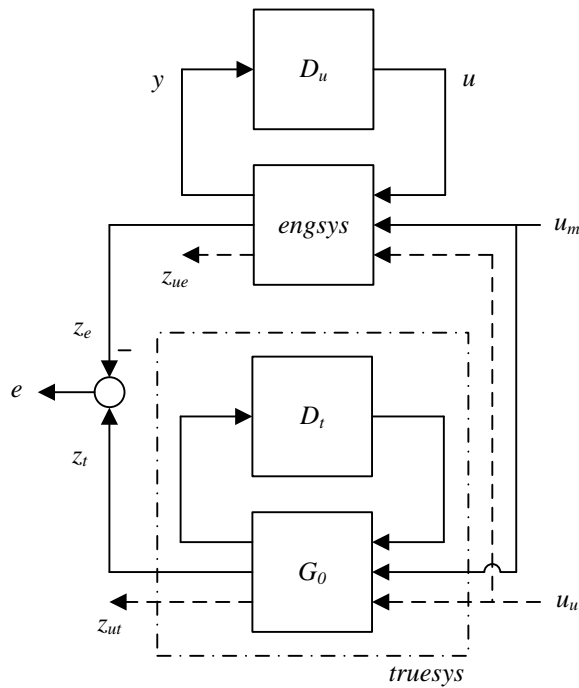


Figure 15 Model-based Identification Control Schematic

are left out of the model, due to either modeling errors or unknown physical phenomena which are related to specific parts of the system, occurring at known locations. Due to these assumptions, model-based identification is able to distinguish between the parts of the system which have a well-defined model and those which are ill-defined.

The solution technique seeks to correct the model by identifying the dynamics which are missing from the engineering model, known as the unmodeled dynamics. First, the unmodeled dynamics is isolated from the rest of the model. Next, the unmodeled dynamics is identified using the control schematic shown in Figure 15 [49]. The figure introduces new parameters, where: u_m is the measured inputs, u_u is the unmeasured inputs, z_{ut} is the unmeasured true system output, z_{ue} is the unmeasured engineering system output, G_0 is the easy to model portion of the true system, D_t is the unmodeled portion of the true system, and D_u is the unmodeled portion of the engineering system.

Similar to the model reconciliation schematic, D_u controls the *engsys* in order to create zero difference between the engineering and true system outputs. As a result, the interconnection of *engsys* and D_u will be equivalent to the combination of G_0 and D_t . Due to the assumptions that the structure of the true system is known and the easy to model portion of the true system G_0 is correctly modeled by *engsys*, i.e. $G_0 = \text{engsys}$, the identified unmodeled dynamics D_u will be equivalent to the true unmodeled dynamics D_t . Additionally, the controlled engineering system may be used to predict the behavior of the true system, as z_{ue} will be equivalent to z_{ut} .

In this work, the model-based identification procedure will be adjusted in two ways. First, the missing dynamics frequency response will be identified through direct calculations instead of the development of a minimizing controller. This adaptation will provide more accurate results due to foregoing the step of fitting a model to the experimental true input-output data [49]. Second, the procedure will be extended to include uncertain elements in the engineering system. As a result, the identified dynamics

will inherit the uncertainties, providing an uncertainty bound and a quality estimation for the identified dynamics.

The use of direct calculations solves the model-based identification control schematic in Figure 15 by first setting $e = 0$ and employing the definition of an LFT:

$$T = E_{22} + E_{21}D_0(I - E_{11}D_0)^{-1}E_{12} \quad (3.7)$$

where T is the transfer function of the true system, D_0 is the nominal, i.e. not uncertain, unmodeled dynamics, E_{11} , E_{12} , E_{21} , and E_{22} are the partitions of the engineering system with inputs and outputs corresponding to the figure, and I is an appropriately sized identity matrix. Rearranging leads to:

$$E_{21}^{-1}(T - E_{22})E_{12}^{-1} = D_0(I - E_{11}D_0)^{-1} \quad (3.8)$$

Inverting both sides of the equation gives:

$$(I - E_{11}D_0)D_0^{-1} = E_{12}(T - E_{22})^{-1}E_{21} \quad (3.9)$$

Distributing D_0^{-1} and rearranging further produces:

$$D_0^{-1} = E_{12}(T - E_{22})^{-1}E_{21} + E_{11} \quad (3.10)$$

One more inversion gives the solution:

$$D_0 = \left[E_{12}(T - E_{22})^{-1}E_{21} + E_{11} \right]^{-1} \quad (3.11)$$

This solution will be employed to identify the missing dynamics through direct calculations at each measured frequency.

Next, the model-based identification procedure is extended to include uncertainties on the engineering system. This process consists of expanding the definition of each element in the *engsys* matrix to include an uncertainty perturbation. For example, \hat{E}_{11} represents

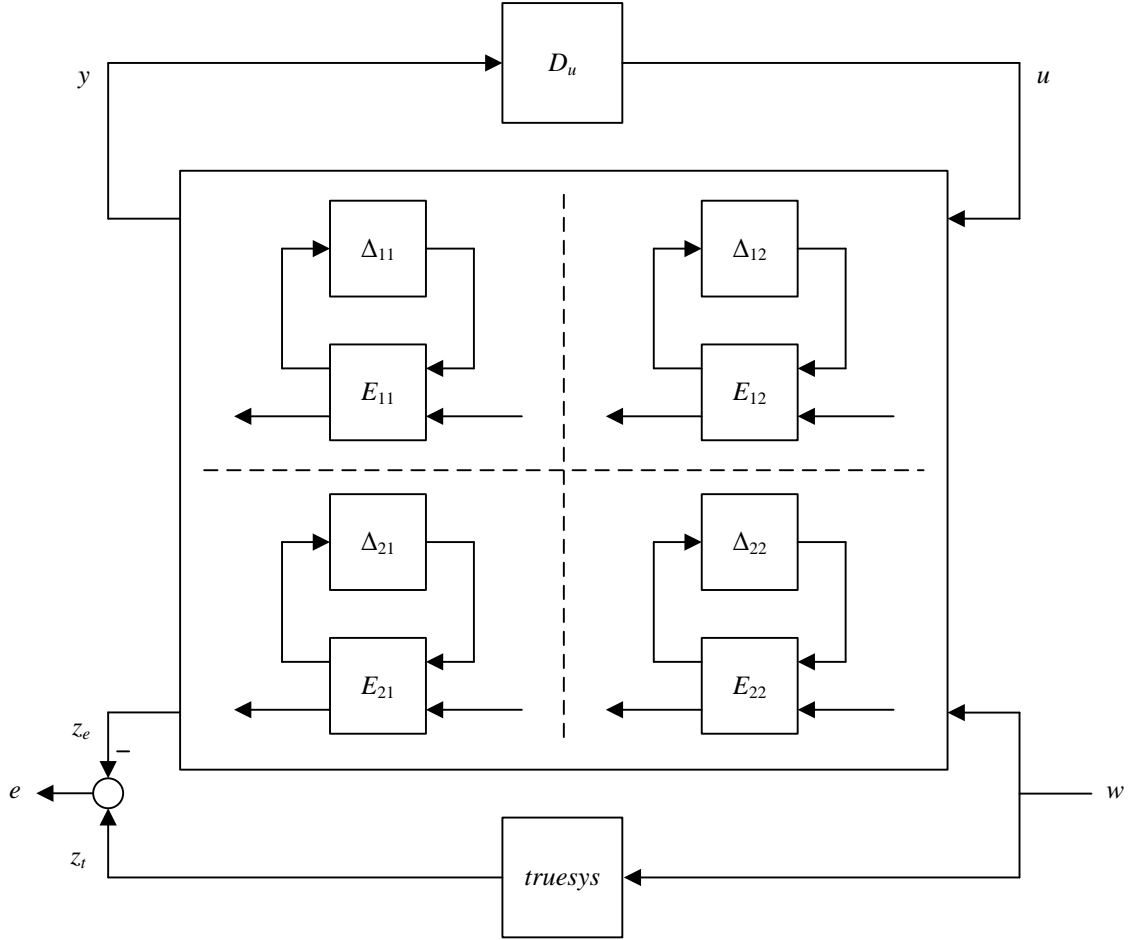


Figure 16 Model-Based Identification Schematic with Uncertainties

the element E_{11} perturbed by the uncertainty Δ_{11} . Repeating this process for each of the elements of the engineering system leads to the updated definition for the unmodeled dynamics [50]:

$$D_u = \left[\hat{E}_{12} (T - \hat{E}_{22})^{-1} \hat{E}_{21} + \hat{E}_{11} \right]^{-1} \quad (3.12)$$

such that D_u is the identified missing dynamics D_0 with the inherited uncertainties found in the model validation procedure. A graphical depiction for this process is shown in Figure 16 illustrating how the unmodeled dynamics will correctly inherit the uncertainties

from the engineering system. The uncertainty bound will indicate the frequencies where the unmodeled dynamics is more and less reliable.

3.3 Application to Damage Identification

In this section, a damage identification method which utilizes the techniques of model validation and model-based identification will be developed. The overview of the technique is to first apply model validation to detection of the presence of damage, followed by the application of model-based identification to decipher the local change in dynamics due to the damage. The resulting methodology can be broken down into five steps:

Step 1 Develop the nominal model. This can be completed using standard engineering techniques such as finite element modeling.

Step 2 Fit the noise to the model. The noise is fit for the particular experiment by matching the noise magnitude V to the noise floor in the data, as explained in the previous section.

Step 3 Bound the uncertainty of the nominal model by solving the FDMVOP. By employing the FDMVOP as illustrated in Figure 13 at each frequency of interest $\omega_i \in \Omega^{id}$, this procedure utilizes the healthy system input W and output Z_t and the nominal healthy model M_e to optimize the permissible uncertainty bound γ . This procedure will experimentally not invalidate the uncertain healthy, i.e. not damaged, system. As a result, any difference between the nominal model and the healthy physical system will be captured in the definitions for the noise and uncertainties, and the uncertain system will be assumed to be suitable for accurately predicting any future behavior of the physical system.

Step 4 Compare the data from a potentially damaged system to the healthy uncertain model. Similar to the previous step, this step also utilizes the FDMVDP illustrated in Figure 13. The difference is that instead of attempting to identify the uncertainty bound to enclose the data, this step will utilize the not invalidated system from the previous step to perform the inverse model validation problem. The uncertain healthy system definition from Step 3 will provide the definition for the model M_e and the uncertainty and noise bounds γ and V , respectively. The inverse problem is to utilize a new set of data Z_t and the healthy uncertain model to check if any frequency points are invalidated. This procedure leads to the definition of the Frequency Domain Inverse Model Validation Decision Problem (FDIMVDP):

Definition 3.4 (FDIMVDP) In the FDIMVDP, given the bounds γ and V , the model is invalidated if $\bar{\mu}_\Delta(\bar{M}_{11} - \bar{M}_{12}\bar{X}_{22}\bar{M}_{21}, \bar{M}_{21} - \bar{M}_{22}\bar{X}_{22}\bar{M}_{21}) \leq 1$ where \bar{X}_{22} is the inverse of \bar{M}_{22} , indicating a change in dynamics in the system not explained by the permissible amount of uncertainty and noise.

Basically, the FDIMVDP is indicating that the uncertainty bounds are no longer large enough to enclose the experimental data. Therefore, there is a difference between the data and nominal model which is not explained by the uncertainty bound and noise. The cause of this difference is a change in dynamics in the system which occurred after the uncertainty bounding of the healthy system in Step 3. For this work, such a change in dynamics is assumed to be due to the presence of damage in the system.

Step 5 Identify the change in dynamics due to the damage. This step follows the model-based identification procedure covered in the previous section as illustrated in Figure 15. For this case, the *engsys* is the healthy engineering model, *true_sys* is the

damaged system and z_t is the data from the damaged system utilized in the previous step. Therefore, D_u becomes the change in dynamics due to the damage. Additionally, the engineering system inherits the uncertainty and noise definitions from the model validation procedure. The uncertain healthy system is utilized as \hat{E}_{22} in Equation 3.12 and illustrated in Figure 16. As a result, the identified change in dynamics due to damage will contain an uncertainty bound which can be utilized as a quality measure for the identified dynamics.

3.4 Illustrative Example of Damage Identification

In this section, a three degree of freedom mass spring damper example is presented to illustrate the robust damage identification method to detect and identify the local change in dynamics due to an imposed damage. The purpose of this example is to demonstrate on a simple system how the method can be applied to robustly detect the presence of damage and identify the contribution of the damage dynamics to the system. Three trials will be completed in order to illustrate the effect of various amounts of modeling uncertainties on the identified damage dynamics.

3.4.1 Experimental Apparatus

The three-mass example covered in this section is an Educational Control Products (ECP) Model 210a Rectilinear Control System. Figure 17 shows the system in the configuration for this experiment and Figure 18 shows the labeled schematic [83]. The plant is a mass and spring setup which consists of three masses connected by two springs, with the end mass connected to ground with a final spring (right-most in Figure 17). Additionally, the system contains an excitation motor, a position encoder on each mass,

and an air damper. The mass carriages are designed to carry adjustable added masses in configurations ranging from 0 to 2 kg. Each of these carriages rides slides on linear stages. The carriages themselves add a non-negligible amount of mass and damping to the masses, and the exact values for these parameters have been identified in a previous work [52]. The motion of the masses is limited by travel stops in each direction which act as safeties containing circuit breakers that shut down the excitation when triggered. Mass position data is obtained through three optical encoders connected to the carriages. The damper, attached to the final mass, is an adjustable air-damper controlled by opening and closing the damper's air flow valve.

The setup is driven by a brushless DC servo motor that drives a rack and pinion. This pinion is connected to the first mass by a rigid link as shown in Figure 17. The attached signal processor serves a dual purpose as both the real-time controller to the motor and the data acquisition. A personal computer is utilized to control the executable program. This program was utilized to obtain the system identification results which were presented in [52] and will be utilized here for the parametric values in the simulation presented in the following sections.



Figure 17 Educational Control Products Model 210a Rectilinear Control System

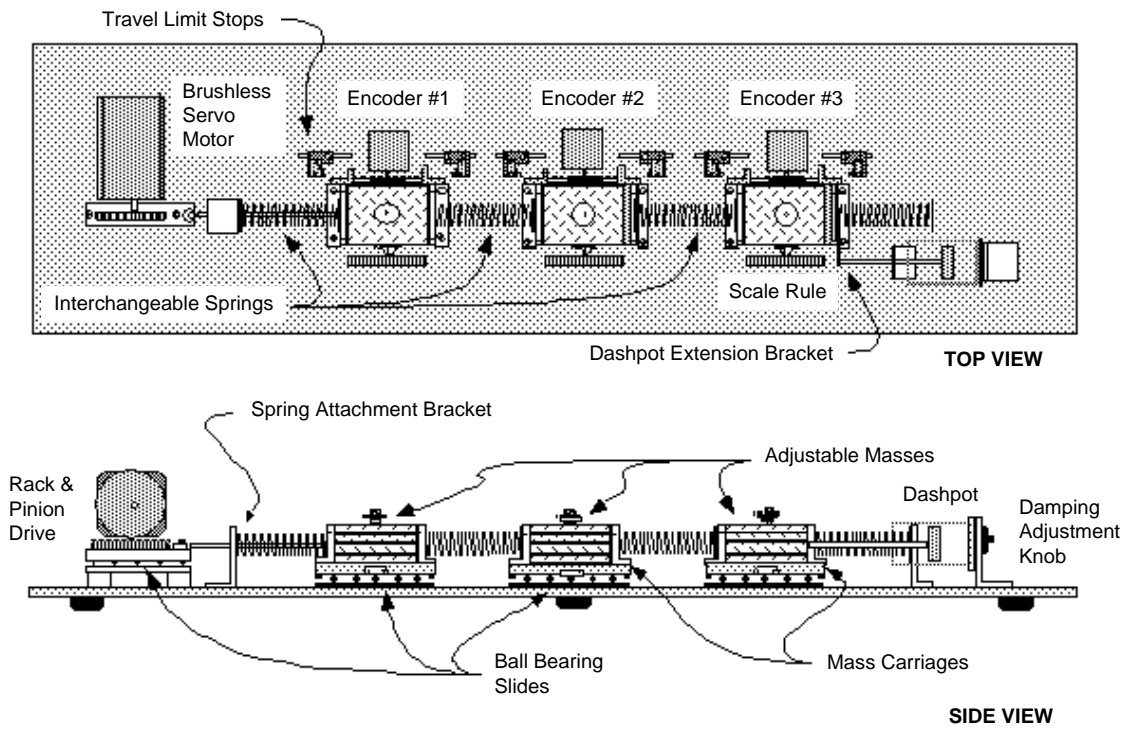


Figure 18 ECP Model 210a Rectilinear Control System Labeled Schematic [83]

3.4.2 Problem Description

In this experiment, damage on the third mass element will be simulated by a loss of stiffness in the third spring. This damage will be detected in the presence of uncertain modeling of the first mass due to the interaction with the rack and pinion drive. The healthy system will be known from previous system identification work on the test rig [52] and is illustrated in Figure 19. Note that damping is modeled between each of the masses to attribute it to the spring material, but this will also account for all other sources of damping, such as the contribution of the cartridges or the motor. Therefore, the damping c_3 is the sum of the effects due to the carriage and dashpot. Meanwhile, the engineering system will be associated with an estimated nominal model. This necessitates the inclusion of the new variable m_{1e} , which represents the modeled value of the first mass. Note that this value will change between trials. Finally, the simulated damaged data will be generated from a similar model with reduced stiffness between the third mass and ground. The new variable k_d is employed to model this change. All of the healthy and shared parameters are listed in Table 1. The healthy, engineering, and damaged systems are illustrated in Figures 19, 20, and 21, respectively.

The first two steps of the damage identification procedure are completed through the definition of the various trials of the example. First, Step 1 is completed by defining m_{1e} ,

Table 1 Three-Mass System Parameters

	Mass (kg)	Stiffness (N/m)	Damping (Ns/m)
Element 1	$m_1=2.8113$	$k_1=842.3$	$c_1=5.992$
Element 2	$m_2=2.6396$	$k_2=806.5$	$c_2=1.9467$
Element 3	$m_3=2.6074$	$k_3=386$	$c_3=10.7375$
Damage	-	$k_d=350$	-

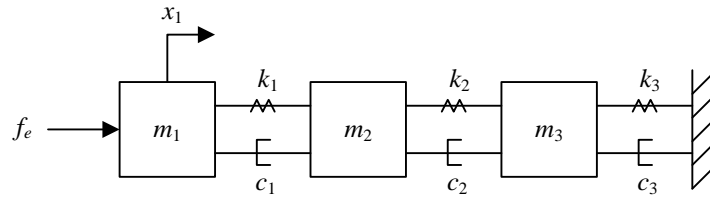


Figure 19 Three-Mass Healthy System (True)

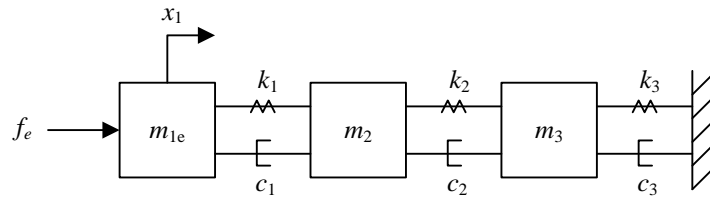


Figure 20 Three-Mass Engineering System Model

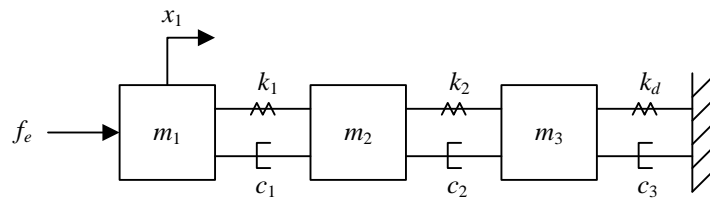


Figure 21 Three-Mass System Model with Damage

which fully defines the engineering system that is used as the nominal model. Next, Step 2 is left out due to the simulation being absent of noise, resulting in the trial case of $V=0$.

For the third step of the damage identification procedure, recall the simple schematic for model validation originally shown in Figure 11, and reproduced with experiment-specific labels in Figure 22. As shown in the diagrams for the healthy and engineering system, both the excitation input f_e and sensor output x_1 are taken at the first mass. Additionally, the uncertainty acts at the first mass due to the known modeling deficiencies. This uncertainty is modeled as a parametric effect on the first mass. The nominal model is rearranged to isolate the effect of the mass uncertainty. Such

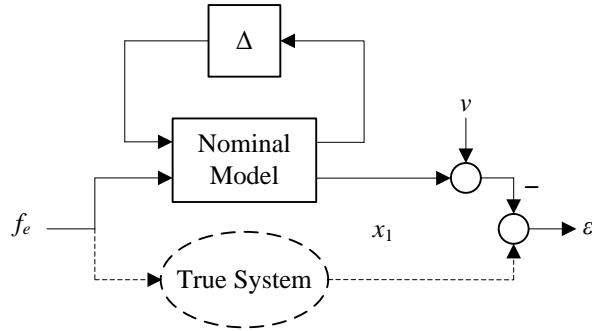


Figure 22 Three-Mass Model Validation

rearranging is easily accomplished through the *lftdata* function in MATLAB. The rearranged engineering system is taken as the nominal model, while the healthy system is utilized for the true system. The healthy data is obtained through a simulation of the frequency response of the healthy system from 0.5 to 8 Hz, which includes the first three natural frequencies. Finally, the nominal model can be decomposed into the various portions of M_e and the FDMVOP illustrated in Figure 13 can be completed. As a result, the healthy uncertain model is obtained by connecting the uncertainty block Δ scaled by γ in LFT with the engineering system.

For Step 4, the same simple model validation schematic may be utilized. Similar to the previous step, the input and output locations for the external excitation and output and uncertainty LFT are utilized. In contrast, the damage detection step utilizes the damaged system as the true system. Also, the healthy uncertain model is used in order to include the identified uncertainty bound.

Finally, for Step 5 of the identification procedure, the model-based identification schematic from Figure 14 is updated as shown in Figure 23. For this example, the two systems being compared are the damaged data and the healthy engineering model. These are represented as *truesys* and *engsys* in the figure, respectively. The known difference in dynamics is the damage occurring at the third mass. Therefore, the virtual controller input

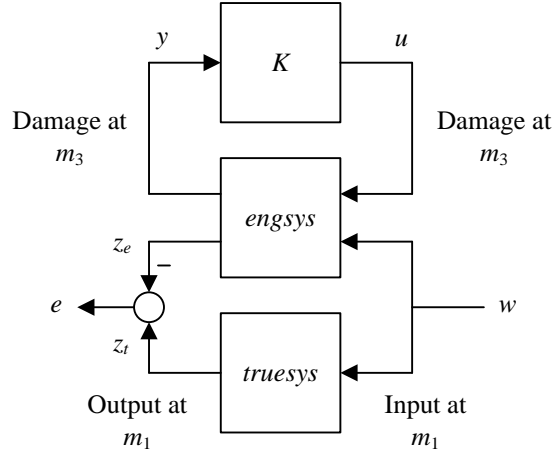


Figure 23 Three-Mass Model-Based Identification

y and output u are taken at the third mass. Similar to the previous steps, the simulated experimental input and output are taken at the first mass. The procedure solves for a D_u which returns zero difference between the true and engineering system outputs z_t and z_e , respectively. As a result, D_u will solve for the difference in dynamics between the two systems, which is the local change in dynamics due to the damage.

Due to the creation of the uncertainty bounds in the model validation steps, the identified damage dynamics D_u will contain a quality estimate in the form of an uncertainty bound. The parametric uncertainty will be defined for all input-output combinations of *engsys*, i.e. \hat{E}_{11} , \hat{E}_{12} , \hat{E}_{21} and \hat{E}_{22} in Equation 3.12, by using the uncertain healthy model developed in Step 3.

3.4.3 Trial 1 Results

For the first trial, the mass of the first element m_{1e} is modeled as 2.6 kg, an 8% departure from the true value of 2.8113 kg. The true values defined in Table 1 are used for all of the other system parameters as illustrated in Figure 20. This definition

completes Step 1 of the damage identification procedure, while Step 2 is omitted due to the simulation containing no noise.

This disparity in the first mass value leads to a nominal model which appears to be less stiff at the first natural frequency and at high frequencies, as illustrated in Figure 24. The plot illustrates the response in mm due to an excitation in N occurring and observed at the first mass over the indicated frequency range of 0.5-8 Hz. For additional insight, the phase response is plotted in Figure 25. The plot indicates the phase difference between the excitation input and the sensor output at each frequency over the indicated range. The phase plot shows that the nominal model lags behind the healthy data due to the difference in mass on the first element.

The results from Step 3 of model validation procedure are also plotted in Figures 24 and 25. The uncertainty bound indicates the range in magnitude and phase which needs to be covered to compensate for the difference between the model response and the healthy data. A larger bound indicates a larger difference between the model and data at that frequency, whereas a smaller bound indicates less of an effect due to the mismodeling. This bound is evaluated in both magnitude and phase due to the model validation technique handling the complex frequency response. For this case, the size of the uncertainty bound in the phase response closely follows the size of the bound in the magnitude.

The results for the damage detection in Step 4 are also indicated in Figures 24 and 25 where the damaged data falls outside of the uncertainty bound. Clearly, the reduction in stiffness from 386 to 350 N/m in the third spring is easily detected through the FDIMVP as indicated by invalidation occurring at the vast majority of the frequency points.

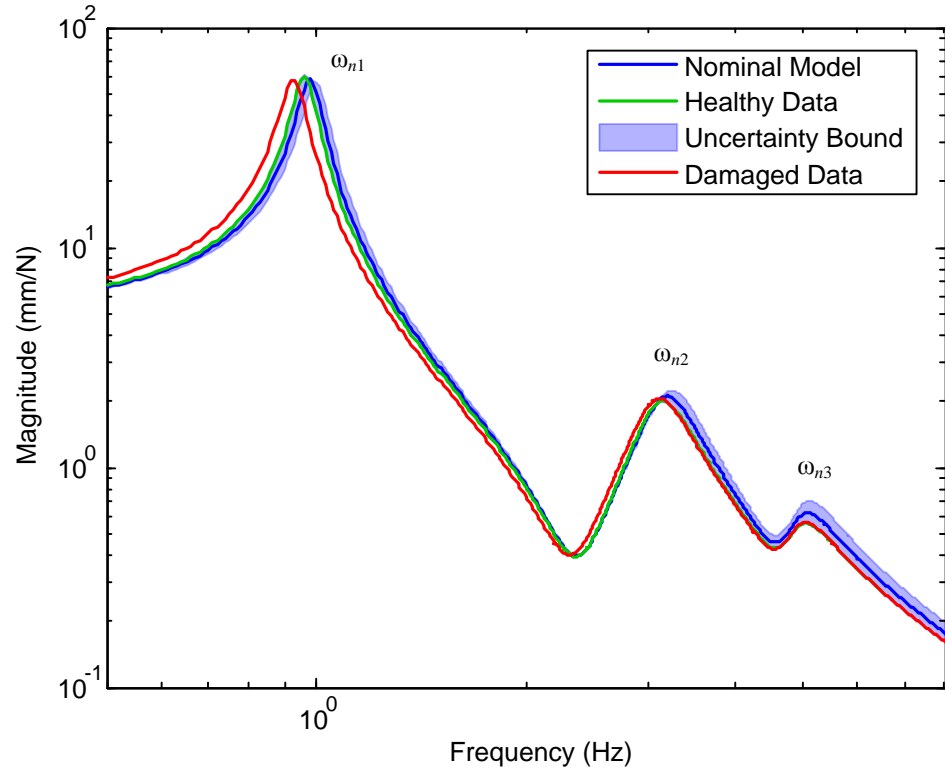


Figure 24 Three-Mass Trial 1 Model Validation Results (Magnitude)

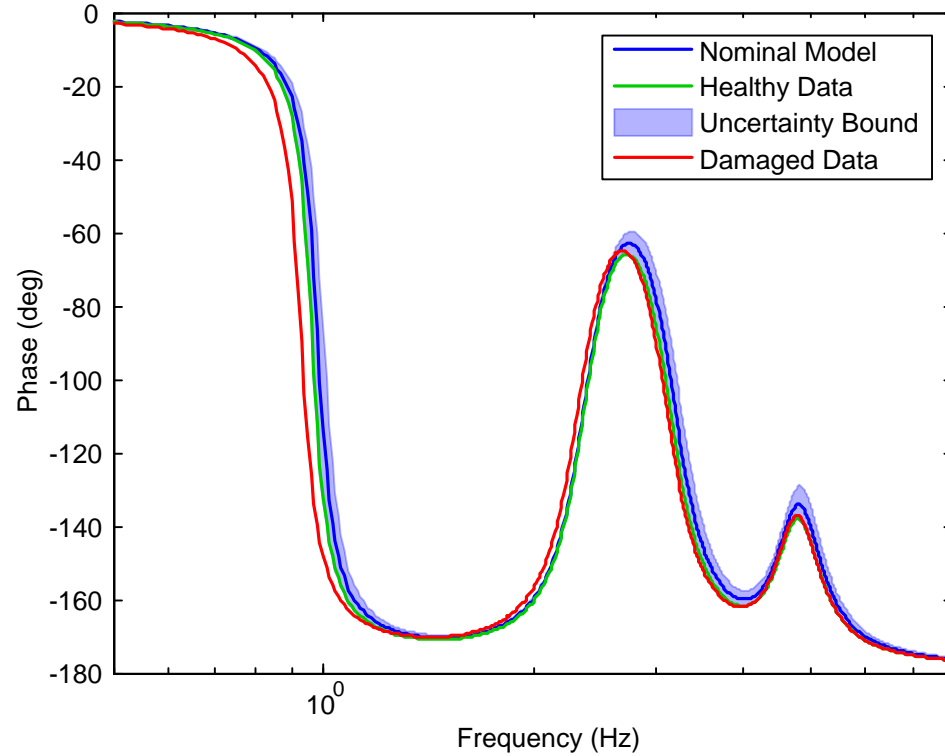


Figure 25 Three-Mass Trial 1 Model Validation Results (Phase)

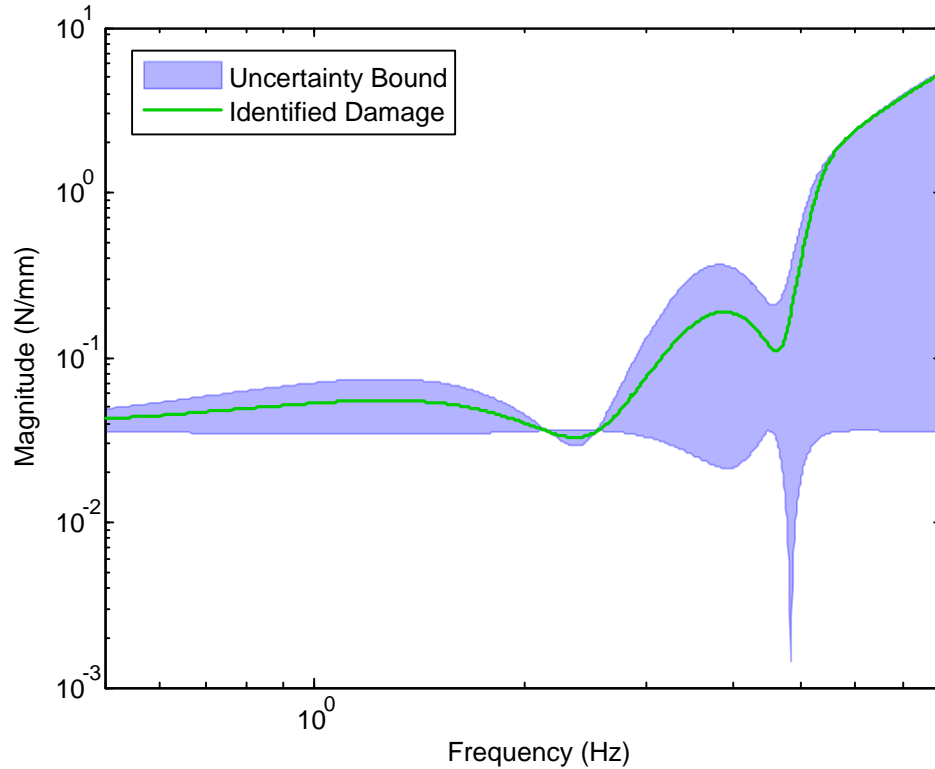


Figure 26 Three-Mass Trial 1 Identified Damage Dynamics

Notably, at higher frequencies the healthy and damaged data begin to act very similarly and data points cease to be invalidated.

Finally, the results from the Step 5 identification of the local damage dynamics are plotted in Figure 26. The figure indicates the response in N due to an input displacement in mm over the indicated frequency range for the identified damage. Additionally, the plot illustrates the uncertainty bound for the identified damage, indicating the quality in the identified damage for each frequency. The size of the uncertainty bound is inherited from the identified uncertainty bound from Step 3 of the method, due to the uncertainty on the first mass. The effect of the size of this uncertainty will be explored by varying the accuracy of the first mass in the nominal engineering model m_{1e} in the trials that follow.

3.4.4 Trial 2 Results

For this trial, the accuracy on the modeling of the first mass is increased. Specifically, the value is increased to 2.75 kg, which is a 2.2% error from the true value. Figure 27 illustrates the accuracy of the nominal model to the healthy data in the same format as Figure 24.

The higher fidelity of the nominal model to the healthy data is reflected in the results of the model validation procedure, Step 3 of the damage identification procedure. As shown in Figure 27, the magnitude of the uncertainty bound remains close to the nominal model response, which naturally follows the behavior of the healthy data overlapping the nominal model at most frequencies. The only significant difference in the dynamics is in the vicinity of the first natural frequency, which occurs around 1 Hz, as indicated by the visibility of the uncertainty bound.

The results from the damage detection step are also presented in Figure 27. Similar to the previous trial, the vast majority of the frequency points are invalidated in the FDMVP. Additionally, two more points are invalidated at the higher end of the frequency. This result is intuitive as more invalidation points are expected due to the increased accuracy of the model in Trial 2. In other words, with smaller uncertainty bounds, damage is more easily detected.

The identified difference in dynamics between the damaged system and the engineering model, or the effect of the damage, is plotted in Figure 28. Once again, the figure indicates the force on the third mass induced by a displacement over a range of frequencies. The shape of the damage appears to be similar to that from the first trial. Interestingly, both the identified damage and uncertainty bound appear to be compressed on the magnitude axis relative to the results from the first trial. For the difference in the

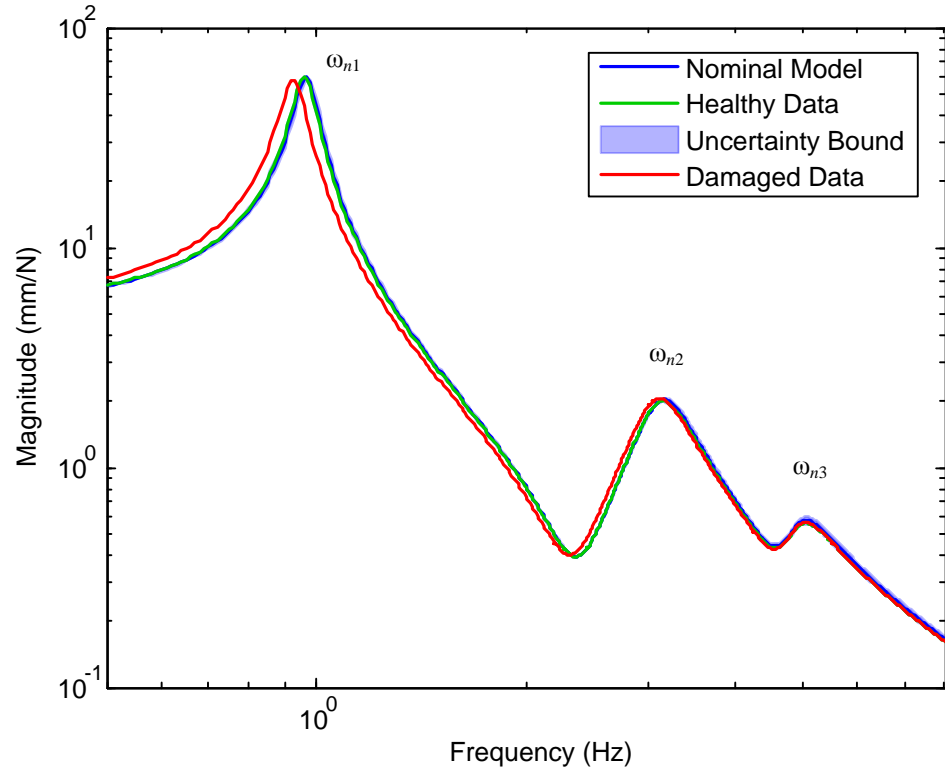


Figure 27 Three-Mass Trial 2 Model Validation Results

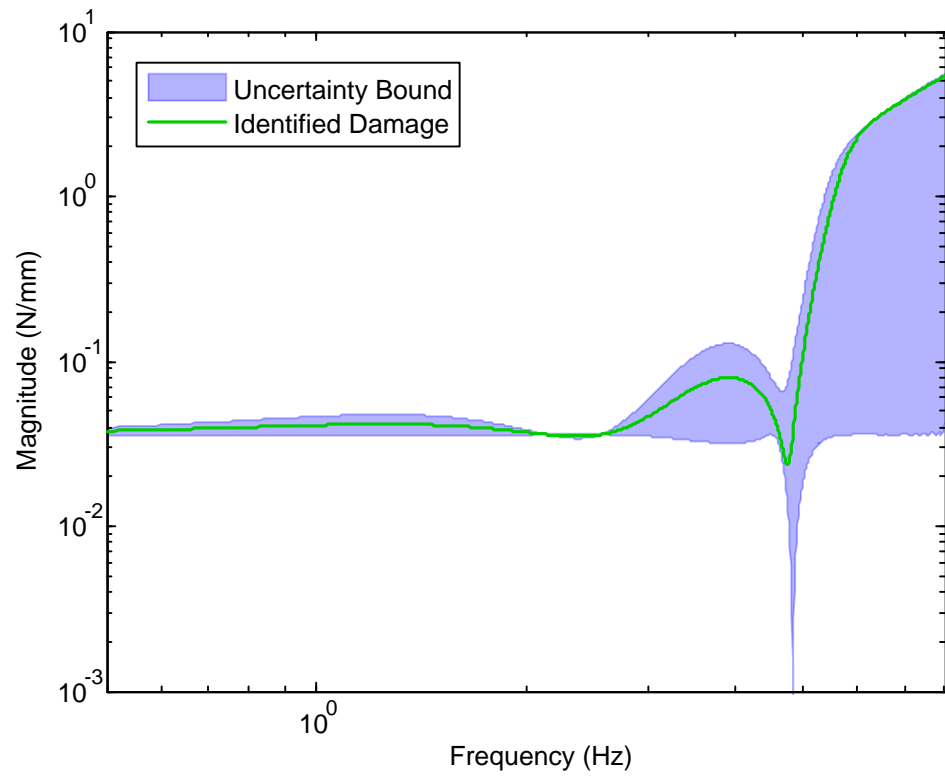


Figure 28 Three-Mass Trial 2 Identified Damage Dynamics

identified damage, this change is due to the difference in the nominal model. For the uncertainty bound on the damage, this difference is due to the increase accuracy of the nominal model, which results in a smaller uncertainty bound in the validation step. Overall, the increased model accuracy is the cause of this trend. In the final trial, the accuracy of the model will be pushed to the limit to investigate damage identification under ideal conditions.

3.4.5 Trial 3 Results

The third trial is a special case of the damage identification procedure. For this case, an engineering model with all parameters matching those of the true healthy system, as defined in Table 1, will be utilized. This is the perfect model trial, i.e. $m_{1e} = m_1$.

For this trial, the majority of the damage identification procedure is completed by simply defining the engineering system as the perfect model. All that is left of the procedure is to identify the difference in dynamics between the damaged and healthy systems. The reason for the steps being omitted follows. First, the engineering system is defined as the healthy system, which makes Step 1 unnecessary. Second, this trial, similar to the previous two, is assumed to contain no noise which removes the need for Step 2. Third, there is no need to bound the uncertainty between the healthy data and the engineering system, because the nominal engineering model is defined to match the system which defines the healthy data. In other words, the model is certain. Therefore, Step 3 is unnecessary. Fourth, the damage detection step, Step 4, is omitted. The reason for this is that any deviation from the healthy data will be detected because there is no uncertain bound for the damaged data to fall into. With all of these reasons considered, it

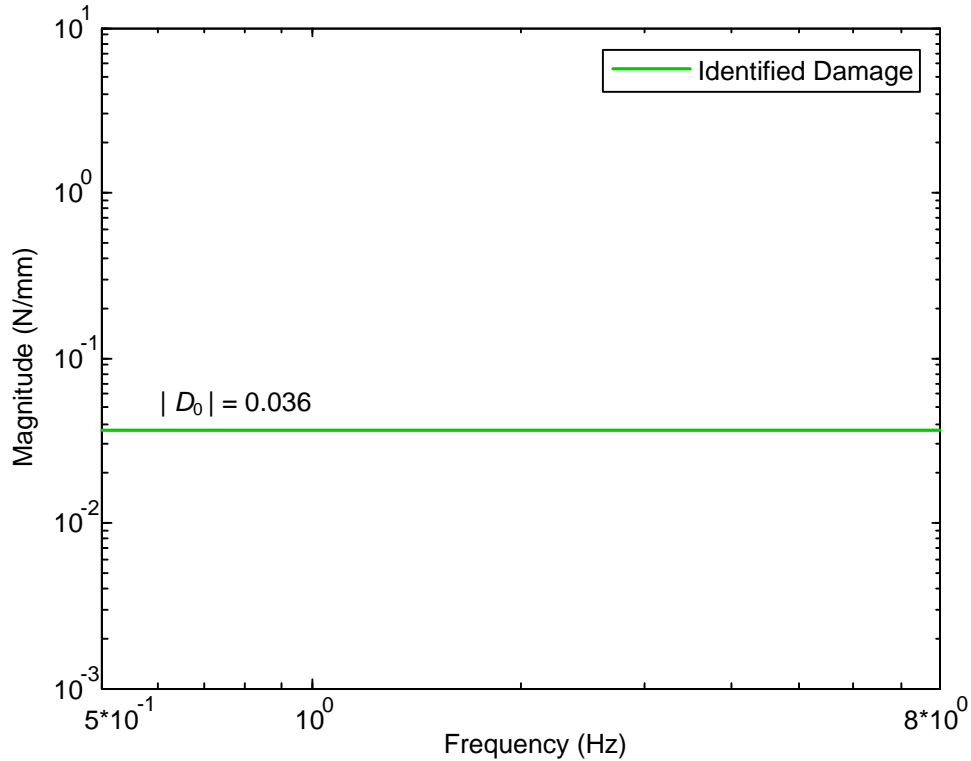


Figure 29 Three-Mass Trial 3 Identified Damage Dynamics

is acceptable to skip directly to Step 5: identifying the change in dynamics due to the damage.

The identified change in dynamics due to the damage is plotted in Figure 29, which shows the force response of the damage due to a displacement for the indicated frequency range. Clearly, the identified damage dynamics illustrated in this figure are much simpler than the previous trials. In fact, the damage directly follows the behavior of a spring with a stiffness of .036 N/mm (36 N/m). This number matches the difference in stiffness of the spring connecting the third mass to ground in the healthy and damaged systems, which is the only difference between the two systems, and is the expected result: $D_0 = k_3 - k_d$.

It is important to note that the identified damage for this trial does not contain an uncertainty bound. This is due to the fact that the model validation step is not necessary for this case. As a result, no uncertainty bound is defined to be carried into the model-

based identification calculation for the missing dynamics. While this may seem like an oversight, the lack of bound can be seen as indicative of the exact accuracy of the engineering system. It can be considered that there is an uncertainty bound associated with the identified damage in Figure 29 and this uncertainty bound has a magnitude of zero at all frequencies. There is evidence that this uncertainty definition is valid in the fact that the results match the expected behavior of a 36 N/m spring being removed from the third mass. In fact, this definition naturally follows the assumption that there are no uncertainties present in the perfect, nominal engineering model. The relationship between the uncertainty bounds for all three trials will be explored in more depth in the following section.

3.4.6 Comparison of the Trials

In this section, the results from the three trials of the three-mass example will be compared in order to gain additional insight into the methodology. The purpose for these three trials was to first give a simple demonstration for the damage identification methodology in order to illustrate the method, and second to vary the models in order to investigate the impact of the model fidelity on the damage identification results. The three models used varied from a significant 8% error on the first mass value, to a smaller 2% error on the first mass, to finally, a perfect engineering model. The impact from this variance is seen in both the model validation and damage detection steps as well as the identified change in dynamics due to the damage.

First, the effect of varying the model accuracy can be seen in Figure 24 and Figure 27. As illustrated, the uncertainty bound on the second trial is smaller due to the increased fidelity of the model to the healthy data. Furthermore, in the third trial, the perfect model

requires no such uncertainty bound as there is no under-modeling or inaccuracies in the model's parameters. Additionally, the effect of the model accuracy can be seen in the damage detection step. As previously mentioned, an additional two frequency points are invalidated when the model is improved from the first to second trial. This is to be expected as the smaller uncertainty bound leads to a smaller change in dynamics being required for a frequency to indicate damage. Though it is not shown, the perfect model would invalidate at every point that is different from the healthy data up to the calculation tolerance of the method.

Second, the effect of the model accuracy in the identified change in dynamics due to the damage can be seen in Figure 30. In general, the closer the nominal model is to the healthy system, the tighter the uncertainty bound. This is clearly illustrated with Trial 1 having the largest bound, Trial 2's bound having about the half of the size for the majority of frequencies, and Trial 3 having no bound. In fact, the entire uncertainty bound from the second trial occurs below or equal to the nominal identified damage from the first trial. Another conclusion from this plot is that it confirms that the uncertainty bounds of the identified damage are correct. This is true because the true identified damage from Trial 3 falls within the bounds of both of the previous trials. Clearly, as the model becomes more accurate, the identified damage trends closer to the true value with the bound in tow. Interestingly, despite the second model being closer to the actual behavior, the damage tends toward the first trial results above 5 Hz. This could be due to the difference in mass dominating the behavior at high frequencies. In conclusion, the uncertainty bound is an appropriate measure of the quality of the identified damage dynamics.

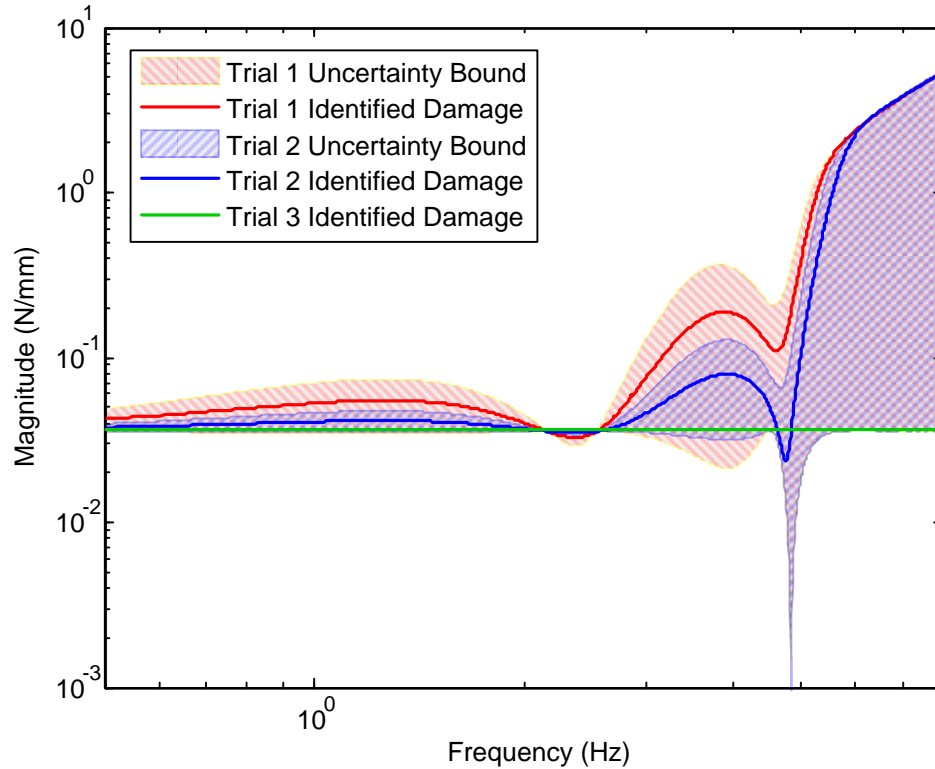


Figure 30 Three-Mass Identified Damage Comparison

3.4.7 Conclusions

This example was developed to demonstrate the steps of the damage identification procedure and to compare the results to a known difference in dynamics simulating damage. In addition to demonstrating the method, three trials were completed which varied the accuracy of the model in order to demonstrate the effect of the model's fidelity on the damage identification results. The results showed improvement in the accuracy of the identified damage as the model became closer to the actual behavior, demonstrating both the importance of an accurate model and the validity of the uncertainty bound as a quality measure of the identified damage. In the next two chapters, the technique will be applied to experimental structural health monitoring examples.

CHAPTER IV

IDENTIFICATION OF A WIRE EDM CUT IN A NON-ROTATING SHAFT

In this chapter, the first of two experimental examples of the developed damage identification technique will be covered. For this example, the effect of an electrical discharge machining (EDM) cut in a rotor will be investigated. The EDM cut is filled with a shim in order to mimic the behavior of a crack in the rotor, though this chapter presents the non-rotating shaft, which will not include the opening and closing of the crack. The goal of this chapter is to demonstrate the identification technique on a physical system with a known damage example in machinery. To begin, the experimental apparatus will be introduced along with some details on the active magnetic bearing (AMB) which are utilized as both the sensor and actuator in the experimental procedure. Second, the seeded damage will be introduced, covering both its creation and the resulting effect on the system. Third, the nominal engineering model which will be used to represent the healthy system will be developed. Fourth, the experiment will be simulated in order to generate baseline results for comparison purposes. Next, the experimental results of the various steps of the damage identification experiment will be

covered. Finally, the chapter will be concluded with some closing remarks on the efficacy of the technique along with some other novel observations.

4.1 Experimental Apparatus

The experimental demonstration is performed on a test rig at the Center for Rotating Machinery Dynamics and Control (RoMaDyC) at Cleveland State University. The test rig was custom-made by SKF Magnetic Bearings, a division of SKF Canada Limited. A photo of the test rig, along with a schematic labeling the key elements, is shown in Figure 31. The AMB rotor and steel disk are mounted on the 660 mm long, 16 mm diameter shaft, 416 stainless steel shaft. For rotation tests (in the next chapter), the rotor is driven by a 48 volt DC brush-type motor. Also shown is the flexible coupling which connects the motor to the shaft and allows both axial and radial displacement. The components are mounted on an aluminum base plate which rests on a Technical Manufacturing Corporation 780 Series Vibration Isolation Table.

System identification experiments are completed utilizing the SKF model MB340g4-ERX digital controllers, which operate both the motor and magnetic bearing exciter. Both the excitation force and the position sensor for the system identification trials are contained in the second magnetic bearing housing. Specifically, excitation is non-contact magnetic force on the rotor in the radial direction; response is measured by non-contact variable reluctance position sensors. A PC is connected to the setup which controls the motor speed and excitation through the MBScope2000 version 4.07 software package. The motor speed is regulated by a PI controller, while the system identification experiments are completed through a programmed sine sweep which regulates the excitation and collects the position data.

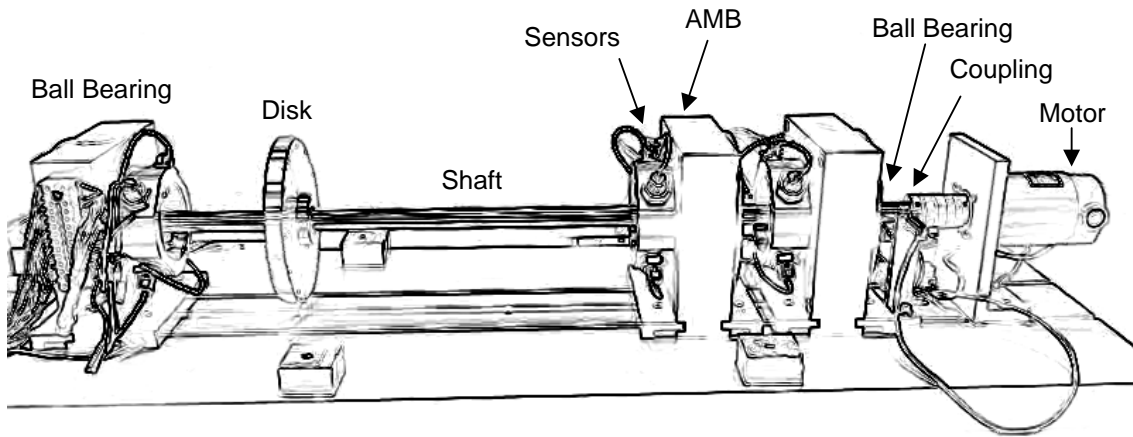
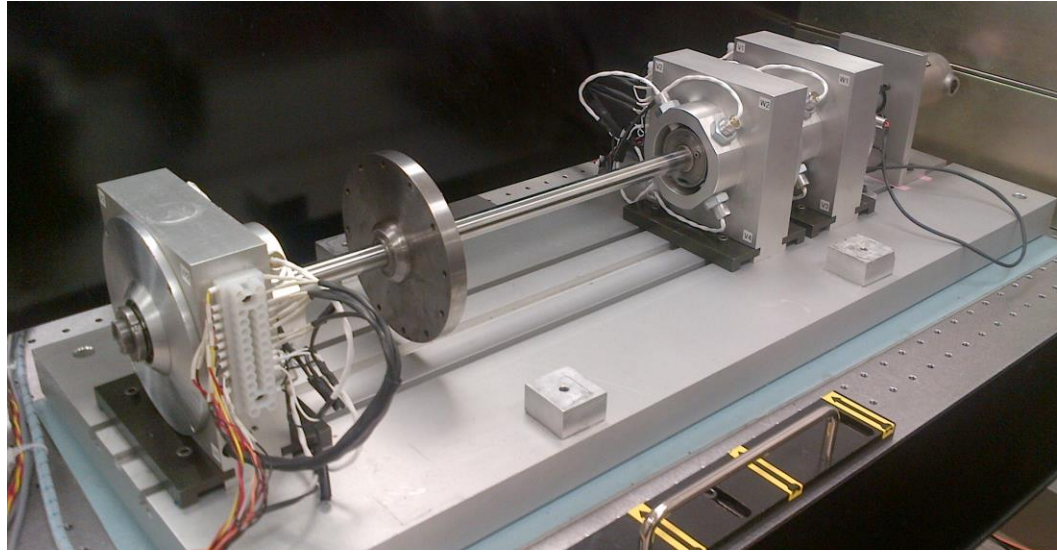


Figure 31 Crack Detection Test Rig Photograph (Top) and Schematic (Bottom)

While the setup contains 3 AMB housings, the first and third are only utilized for conventional, rolling-element bearing support. For this experiment, deep-groove Conrad type rolling element bearings are put in place of the magnetic bearings' touchdown bearings to provide support. Typically, the touchdown bearings are oversized and serve as a safety to support the rotor in case of delevitation. For this trial, the rolling element bearings are snug in order to provide traditional support for the rotor. The rotor

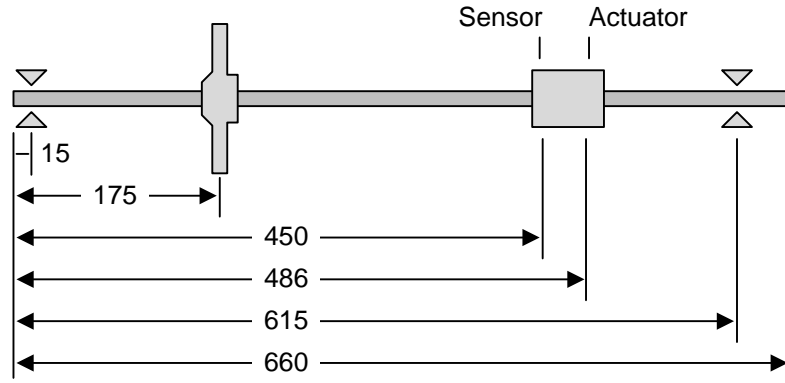


Figure 32 Crack Detection Test Rig Dimensions (mm)

configuration for the experiment is illustrated in Figure 32, indicating the motor-end and non-motor-end supports at 615 and 15 mm, respectively.

As previously mentioned, the center AMB is utilized as both the sensor and actuator for the system identification experiments. The bearing is composed of a stator, sensor, touchdown bearing, and target rotor. The stator, sensor and touchdown bearing are contained in the housing as shown in Figure 33. Four variable reluctance sensors are oriented in two perpendicular axes in order to measure the rotor displacement relative to the center. Figure 34 shows a photograph of the AMB with the cover plate removed to show the stator coils. Actuation force is generated by the radial stator coils attracting the target rotor. The force for one axis is described by the relationship:

$$f = c \left[\frac{i_y^2}{(g - y)^2} - \frac{i_y^2}{(g + y)^2} \right] \quad (4.1)$$

where c is the calibration factor which is dependent on the AMB geometry, i_y is the excitation current in the coils, g is the gap between the rotor and magnetic poles when the rotor is at the center point of the sensors/stators, and y is the displacement from the center point. In the equation, the first term refers to the force produced by the top coil, whereas

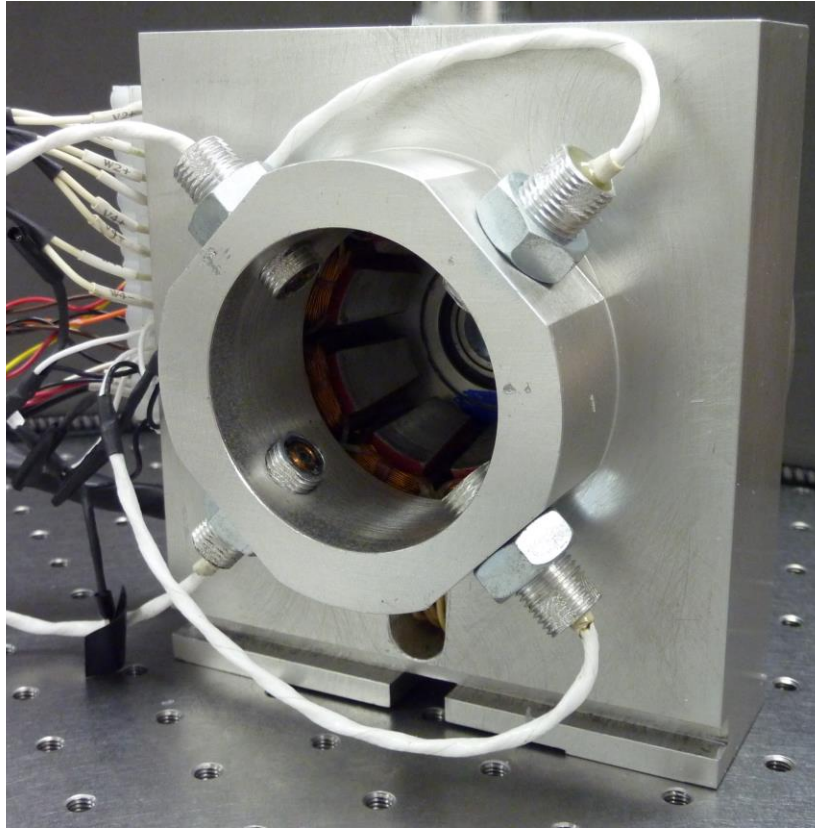


Figure 33 Photograph of Active Magnetic Bearing

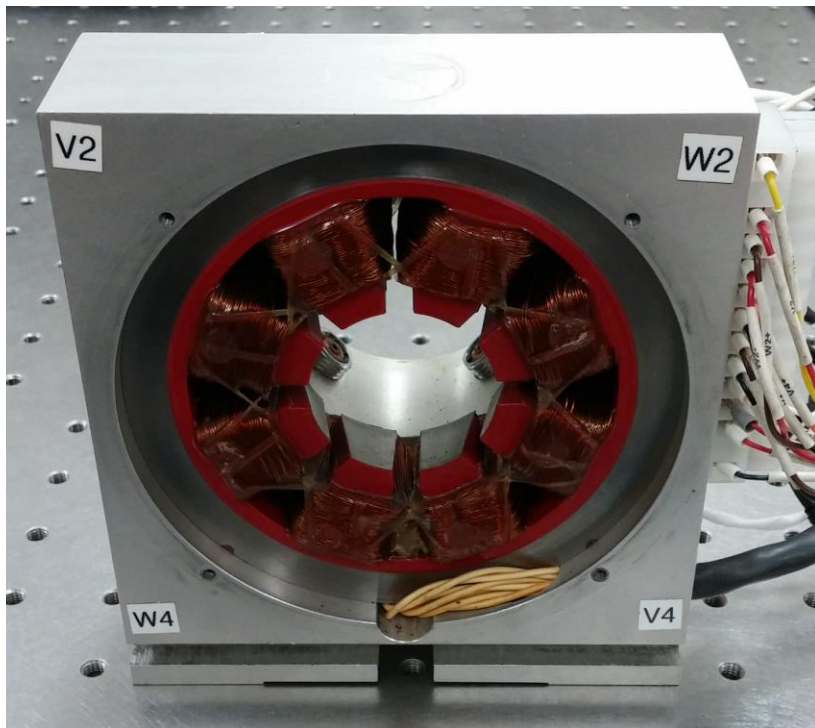


Figure 34 Photograph of Active Magnetic Bearing Coils

the second term refers to the bottom coil. This definition is important in converting the experimental sine sweeps from current in and position out to force in and position out.

4.2 Damage Description

For this work, the experimental damage is created using a wire EDM cut. The cut is placed at the bearing mid-span, with a depth of 40% of the shaft diameter, and a width of 114 μm . A diagram of the cut location and a close-up view of the edge of the cut is shown in Figure 35. In order to achieve a more accurate representation of the behavior of a theoretical crack, i.e. zero width, the cut is filled with a metal shim. Figure 36 shows the filled cut, or “crack”, next to a U.S. penny for scale.

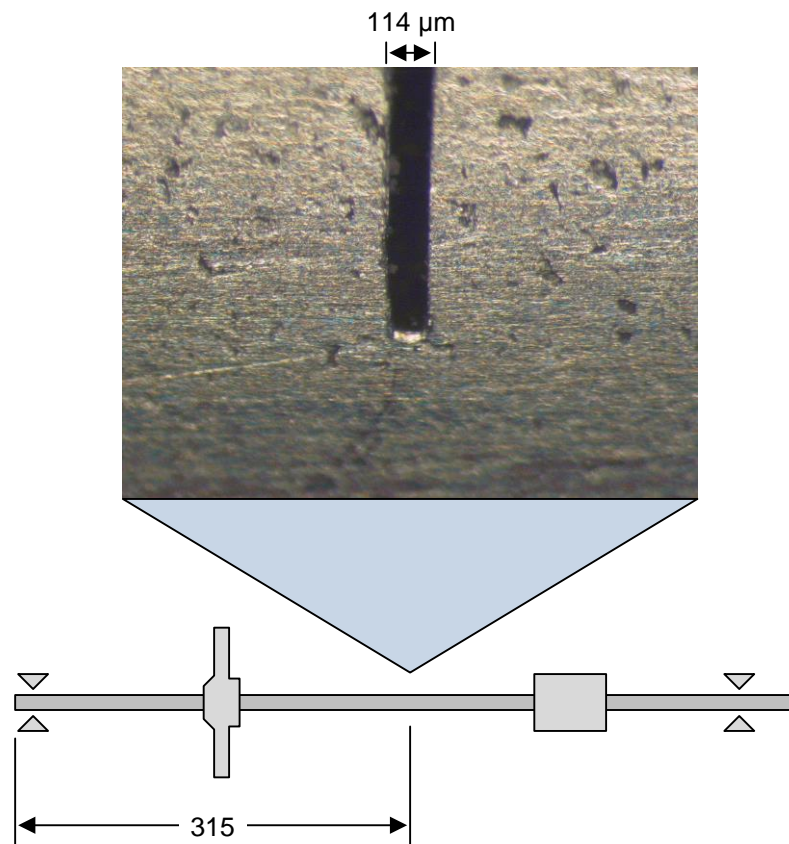


Figure 35 EDM Cut with Location (mm)

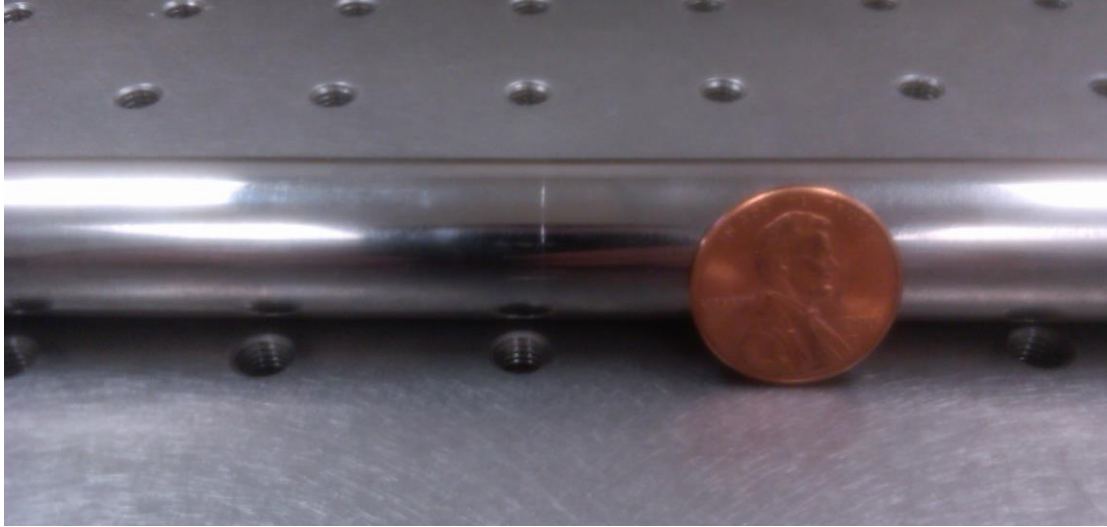


Figure 36 Photograph of the Filled EDM Cut

4.3 Modeling

For the damage identification experiment, an accurate model of the healthy rotor-bearing system is required. This model is generated using a finite element modeling code which originally appeared in the supplemental materials from [84]. The method utilizes Timoshenko beam elements

Both the disc and AMB rotor are defined by their mass and polar and transverse moments of inertia, and each of these components act at FE nodes at their respective centers of mass. Finally, the support bearings are modeled by axisymmetric stiffnesses and damping acting at their geometric centers. The complete schematic for the rotor-bearing system is shown in Figure 37. All modeling parameters for the rotor-bearing system are listed in a table in the Appendix.

Additionally, the first three mode shapes of the rotor-bearing system are illustrated in Figure 37. These mode shapes indicate the shape that the healthy rotor will deflect when the system is excited at each of the first three natural frequencies, which are predicted to occur at 54, 173 and 534 Hz. As a result, the relative effect of each element on the

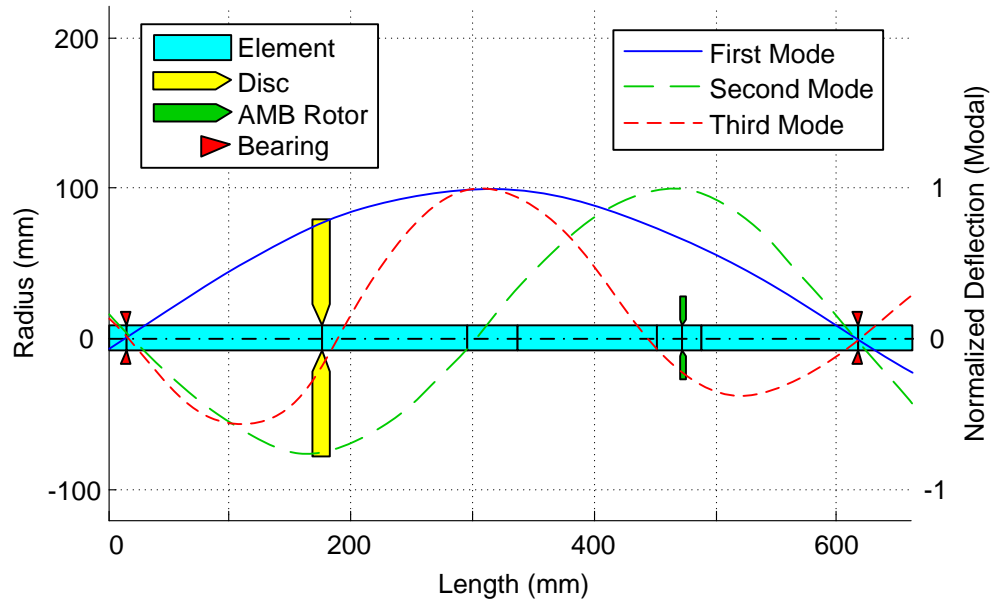


Figure 37 Finite Element Discretization of Rotor System with Mode Shapes

behavior of each natural frequency is predicted when generating these plots. For example, a change in the disc's mass is predicted to have the largest effect on the second natural frequency due to its proximity to the maximum of the second mode shape. Conversely, the disc would have less of an effect on the first mode, where it appears closer to the middle of the mode shape's magnitude. Finally, the disc is predicted to have a small effect on the second vibration mode, due to its proximity to the mode shape crossing the zero at 190 mm.

Next, the accuracy of the model is confirmed with the healthy experimental data as illustrated in Figure 38. The figure indicates the frequency response magnitude in μm due to an excitation force in N over the indicated frequency range. This data was obtained by applying a current in the form of a sine wave at a given frequency to the magnetic bearing actuator and averaging the maximum response magnitude over several cycles and repeating for each frequency point. As shown, the model is accurate to the healthy data overall. Particularly, the first natural frequency matches at 54 Hz, while the second

misses the experimental value by only 1.14%. As the frequency increases, the model becomes less accurate, as the third natural frequency misses the experimental value by 3.56%. Any modeling inaccuracies must be carefully noted, as this damage identification methodology is model-based. For example, despite the fact that the location of the anti-resonance between the first two natural frequencies is generally not of particular concern in rotor design, this discrepancy will appear in the results of the damage identification procedure and may become important.

Similar to the magnitude response plot, the phase response plot in Figure 39 confirms the accuracy of the model through the first three natural frequencies. This figure illustrates the phase difference between the input force and output displacement for the indicated frequency range. Additionally, the plot mirrors the effect of incorrectly locating the first anti-resonance in the model, lagging behind the phase shift in the data at just above 100 Hz.

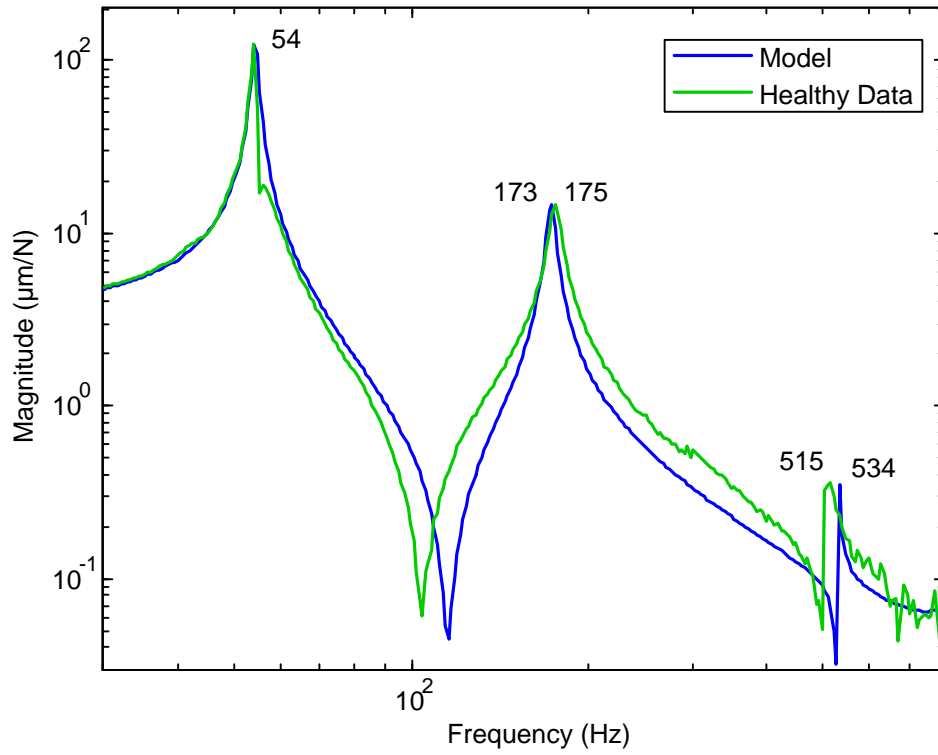


Figure 38 Magnitude Response of the Nominal Model Compared to the Healthy Data

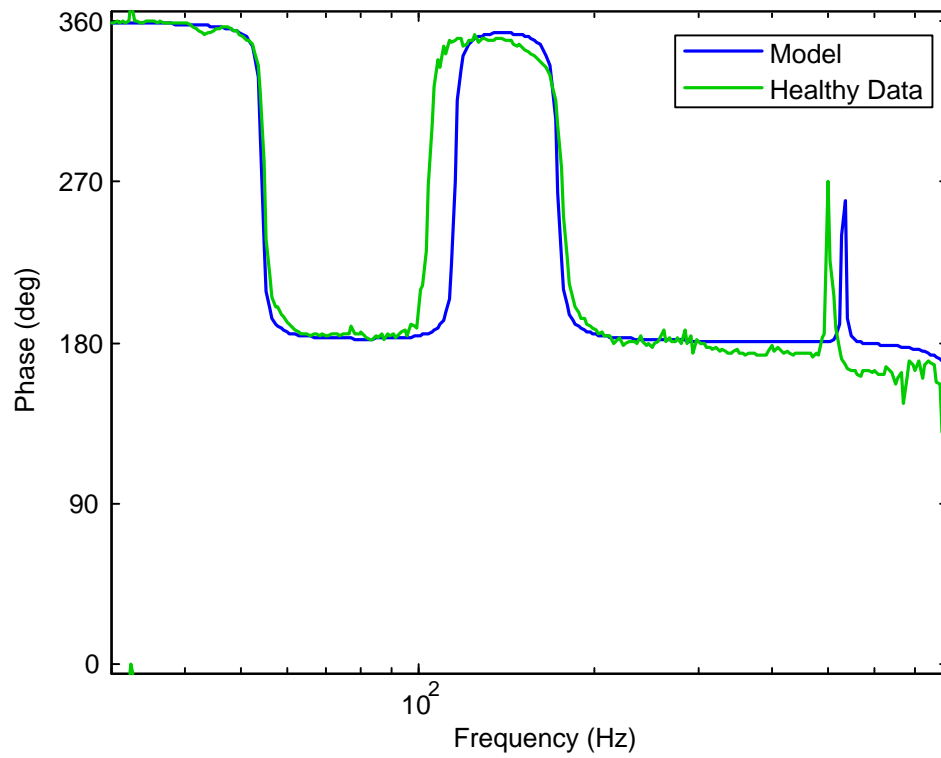


Figure 39 Phase Response of the Nominal Model Compared to the Healthy Data

4.4 Simulation of a Non-Rotating Crack

A simulation of the study is completed in order to gain a frame of reference for the experimental damage identification study. The aim of this simulation is to compare the experimental results to accepted methods for modeling the damage source. To begin, a model for the filled EDM cut is generated.

The model used to generate the damaged data begins as the healthy nominal model presented in the previous section. All of the parameters are kept the same as those shown in the Appendix with the exception of the material properties of the damaged element, indicated in Figure 40. The simplest way to model the non-rotating crack is a reduction in the stiffness by altering the Young's modulus of the element. For this experimental simulation comparison, the elastic modulus is tuned such that the first natural frequency of the model matched the experimental damaged data, as the healthy model and data match at this point and the maximum bending for the first mode occurs within the damaged element. Experimental data was obtained using the same sine sweep method for the healthy data introduced in Section 4.3 with the damaged experimental setup presented in Section 4.2 with the crack facing downward, i.e. fully open. The resulting value for the Young's modulus is 46% of the nominal value for the 40% depth cut.

The accuracy of the resulting damaged model is illustrated in Figure 41. The plot shows the frequency response magnitude of the damaged model and damaged experimental system due to an input force in the frequency range of 30 to 800 Hz. As shown, the first natural frequency of the model is effectively tuned to match the data. The natural frequency is easily matched using the modulus of elasticity, i.e. the Young's modulus, due to the element being located near the maximum bending of the first mode, as shown in 36. Conversely, the second natural frequency was little affected by the

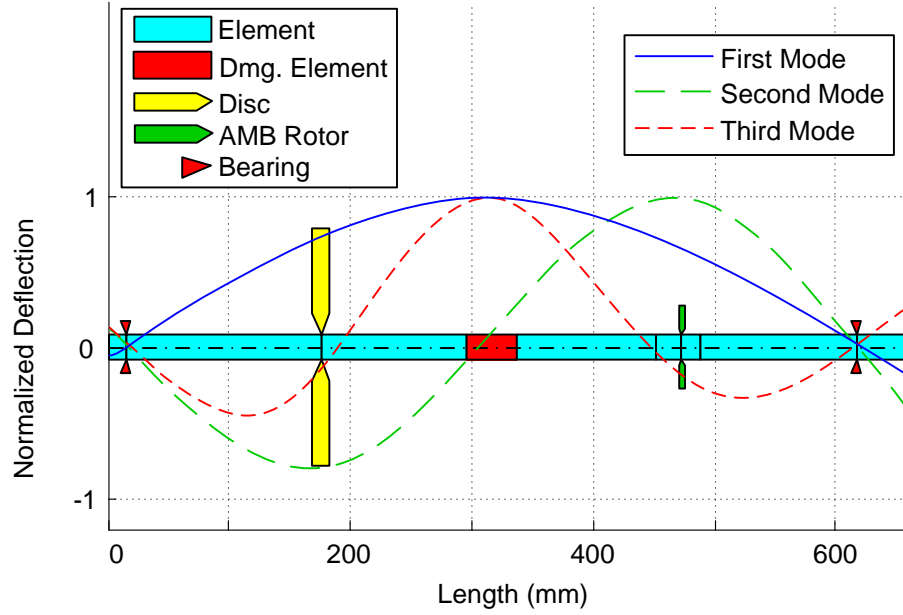


Figure 40 Location of Damaged Element in Simulated Damaged Model

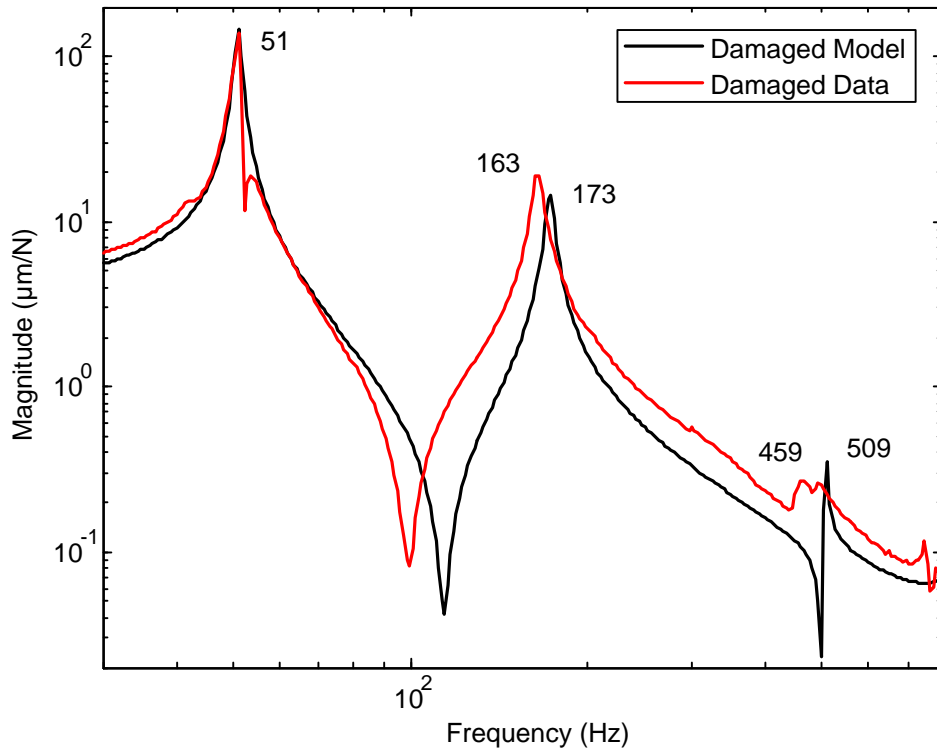


Figure 41 Comparison of the Simulated and Experimental Non-rotating Crack Responses

change in Young's modulus. Similarly, this is also due to the mode shape, which contains a node which passes through the damaged element. The third natural frequency shares similar issues in tracking the experimental data. Particularly, the resonance peak is not showing the same decrease in stiffness as the experimental data. While this error may be attributed to the model incorrectly estimated the undamaged third natural frequency, the relative amount of reduction is not the same. In particular, the data shows a 10.9% reduction in the peak, whereas the model only moves the peak 4.7%. Once again, the simulation is showing decreasing accuracy as the frequency increases.

4.5 Simulated Damage Identification

The damage identification experiment is completed in order to identify the change in dynamics due to the simulated approximation of the damage. Recalling the procedure outlined in Section 3.3, the first step of defining the nominal model was completed in Section 4.3. Next, the noise was fit to match the healthy data. This is completed by tuning the noise magnitude to match the noise floor that is observed from the system identification experiment. The result is Gaussian white noise with a standard deviation of $0.02 \mu\text{m}$. While this number is significantly lower than what would be expected from a single frequency-dependent sweep, the nature of the sine sweep works to minimize this effect. In order to observe the true input-output behavior of the system, the sine sweep averages the results from several cycles at each frequency point. For this experiment, 64 periods per convolution were recorded and averaged. Clearly, the effect of the noise on the data is very slight, and only becomes problematic at frequencies above 600 Hz, as shown in Figures 38 and 39.

Next, the uncertainty of the healthy system is bound to enclose the experimental healthy data. For this experiment, a dynamic uncertainty structure is selected to act on the system identification input-output. This representation is chosen due to the parameters of the healthy finite element model matching the material properties, making parametric uncertainties less appropriate.

The resulting uncertainty bound is illustrated in Figure 42, which summarizes the model validation steps of the damage identification approach through a frequency-dependent magnitude input-output response. As shown, the uncertainty bound encloses the healthy data and is centered about the nominal model. Naturally, the size of the uncertainty bound reflects the fidelity of the model to the healthy data. The uncertainty bound indicates that the model is most accurate through the first natural frequency and around the second natural frequency. Conversely, the mismodeling of the first anti-resonance is reflected in the size of the uncertainty bound. Fortunately, the lower bound has a relatively low total magnitude, which appears exaggerated due to the log scale. Additionally, the bound is larger past the second natural frequency as the data remains above the model magnitude. Finally, the bound reflects the difference in the predicted and actual values of the third natural frequency.

Additional insight into the uncertainty bound is provided by the phase response shown in Figure 43. The figure illustrates the phase difference between the input force and displacement output between 30 and 600 Hz. While this figure offers much of the same interpretation as the magnitude response, it provides more information on the mismodeling of the anti-resonance. Specifically, the complete phase range is covered by the uncertainty bound for frequencies in the vicinity of the experimental and modeled

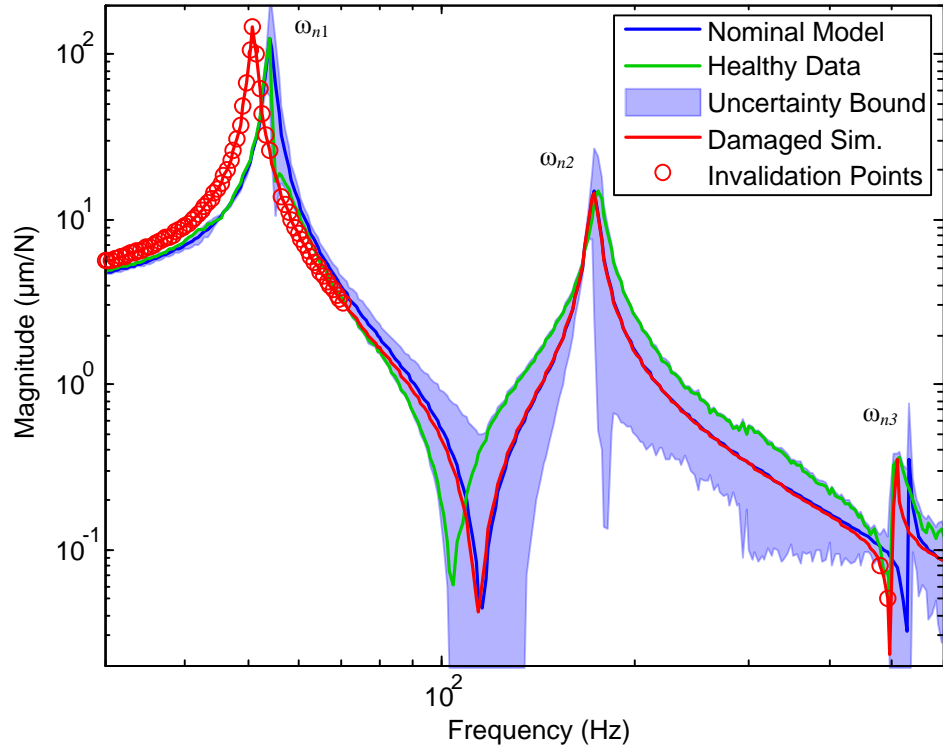


Figure 42 Simulated Non-Rotating Crack Damage Model Validation Results (Magnitude)

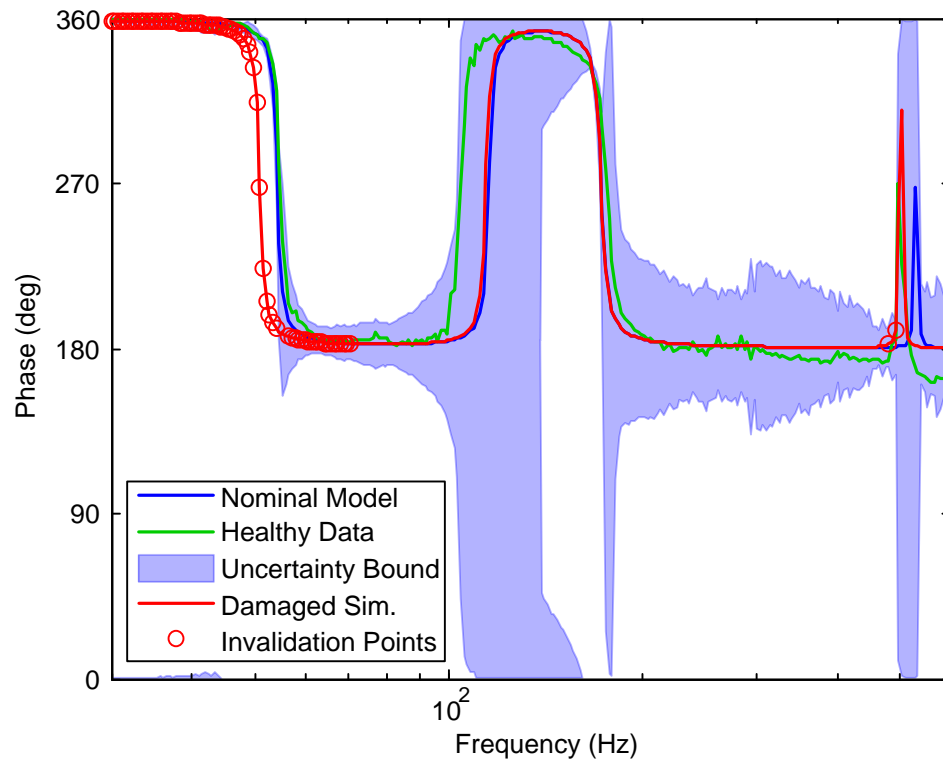


Figure 43 Simulated Non-Rotating Crack Damage Model Validation Results (Phase)

anti-resonances. This is due to the uncertainty bound encompassing zero in the complex plane. As a result, the bound encloses the entire 360 degree phase shift range.

Note that the frequency has been cut off at 600 Hz, just after the third natural frequency, where the effect of the noise on the data becomes more apparent. The reason for this choice is that an inaccurate model will produce an unreliable estimate for the local change in dynamics due to the damage.

Subsequently, the damaged system is compared to the uncertain healthy system in order to detect a change in dynamics which is indicative of the presence of damage. These results are also summarized in Figure 42 and Figure 43. As illustrated, the damage is detected primarily due to the movement of the first natural frequency peak. Interestingly, there are two points before the third natural frequency which also indicate the presence of damage. Despite the mismatching between the nominal model and the healthy data in this area, the difference between the nominal and damaged third natural frequency is high enough to cause the anti-resonance preceding the third damaged natural frequency to fall out of the uncertainty bound.

Clearly, the damage is primarily detected around the first natural frequency. This is due to these frequencies meeting two criteria. First, the damage causes the response to change at these frequencies. Second, the model is accurate in this area. Of the three resonance peaks, only the first meets both criteria. While the second is modeled accurately in the area, the damage does not cause a significant change; therefore there is nothing invalidated. Finally, the third peak shows a detectable change in dynamics, but the healthy data is so far from the nominal model that the damaged system is held within the uncertainty bounds for the most part.

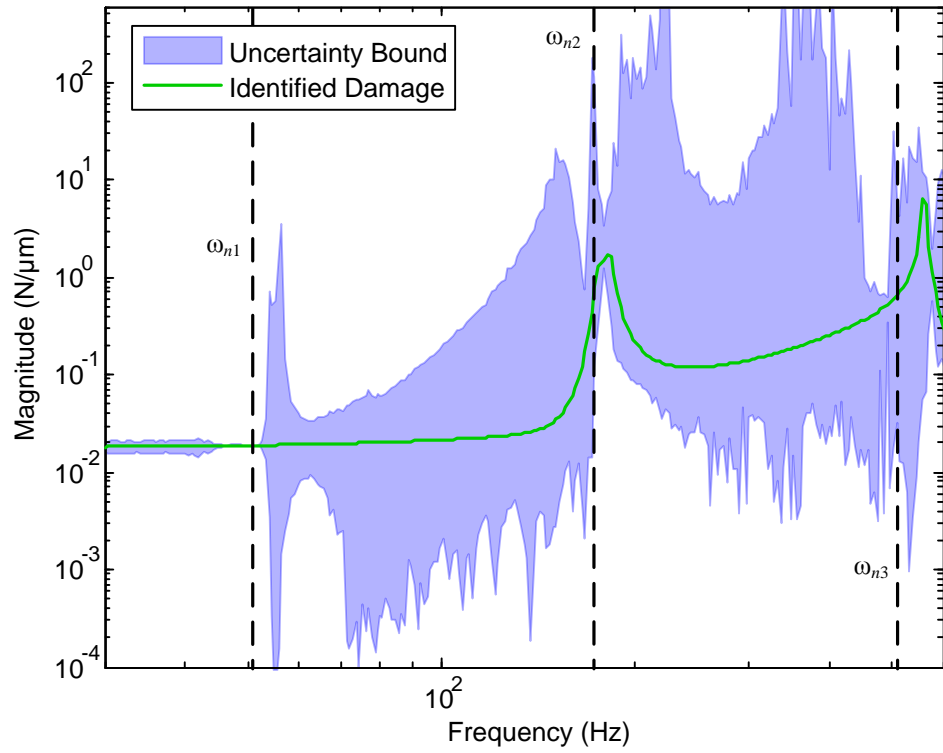


Figure 44 Simulated Non-Rotating Crack Identified Damage Dynamics (Magnitude)

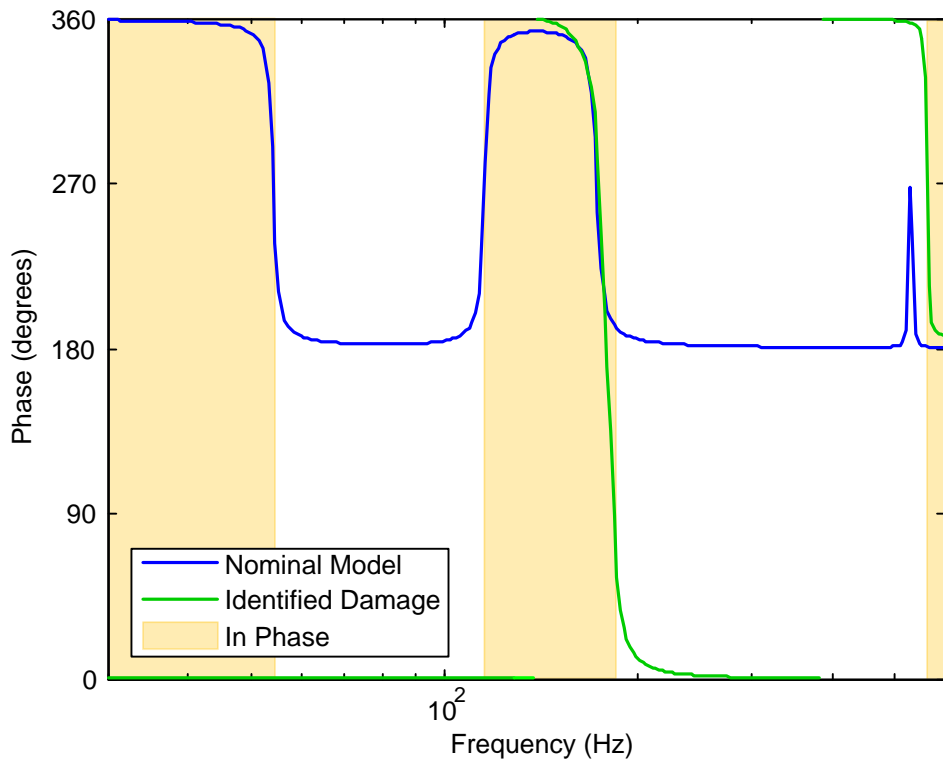


Figure 45 Simulated Non-Rotating Crack Identified Damage Dynamics (Phase)

Finally, the change in dynamics due to the simulated, non-rotating, filled EDM cut is identified, as shown in Figure 44. The plot indicates the frequency-dependent magnitude response of the identified damage dynamics in N due to a displacement in μm , presented this way in order to relate to a change in stiffness. This is consistent with the problem formulation as D_u in feedback. A few observations can be made about the damage behavior. First, the damage acts as a flat change in stiffness through the first natural frequency ω_{n1} up until just before the second natural frequency. This equates to the change in a spring stiffness at the damage location. Second, the damage indicates peaks of its own. These occur at frequencies trailing the second and third damaged data natural frequencies ω_{n2} and ω_{n3} , respectively. Third, in the area between the peaks, the stiffness magnitude is ramping upward. This is likely due to the roll-off in the magnitude response at higher frequencies requiring a larger stiffness to achieve the same change in dynamics.

The final indicator of the identified damage behavior is the phase. The phase of the identified damage will indicate whether the stiffness is reduced or increased based on its value relative to the healthy model and is shown in Figure 45. In regions where the damage dynamics is in phase with the model, there is a reduction in stiffness, whereas when the two are out of phase, there is an increase in stiffness. These phase regions change due to the nominal model switching phase as it passes through natural frequencies and anti-resonances. Specifically, the two responses begin in phase, and switch to out of phase at the first damaged natural frequency ω_{n1} . Next, the two return to being in phase after the first anti-resonance, and become out of phase after the second natural frequency ω_{n2} . Note that the second anti-resonance does not cause the phase relation to change. As shown in Figure 43, this is due to the closeness of the third natural frequency, which

doesn't allow for the phase of the damaged data to fully shift to 180 degrees out of phase, instead returning it to zero degrees. This behavior can be verified by inspection of the damaged data and nominal model magnitudes in Figure 42. In areas where the stiffness is reduced, the damaged data shows an increase in compliance, the inverse of stiffness. Alternatively, when the stiffness is increased, the compliance decreases.

The uncertainty bound illustrated in Figure 44 indicates the quality of the identified damage dynamics. While most of the conclusions that can be drawn from this bound follow the uncertainty bound on the healthy model, there still remain a few important observations. First, the peak maxima of the nominal identified damage, occurring just after the second and third natural frequencies, do not necessarily lead to larger uncertainty bounds. While the first peak corresponds to a peak in the uncertainty bound, the second does not follow this trend. Also, the peak in the uncertainty bound at 54 Hz occurs independently of the nominal identified damage. Second, the missed location of the healthy model anti-resonance does not lead to a noticeable peak in the uncertainty bound. Therefore, this modeling accuracy will not be a major concern in future trials. Finally, the size of the uncertainty bound above 200 Hz does not instill confidence in the identified damage dynamics in that region. A more accurate model in this region would alleviate this issue.

4.6 Experimental Results

The damage identification procedure is completed in order to identify the change in dynamics due to the presence of the experimental non-rotating EDM cut. Once again, this procedure will repeat the process for damage identification outlined in Section 3.3. The first step, creating the nominal model, was covered in Section 4.3. The next two steps of

fitting the noise and bounding the uncertainties mirror the process completed for the simulation. In fact, both the simulation of and the actual experiment utilize the same nominal model and healthy data. As a result, the same noise fit and uncertainty bound are obtained. The result of these two steps is illustrated in Figure 46. The figure illustrates the displacement response of the nominal model and healthy data due to a force input acting over frequencies ranging from 30 to 600 Hz. As shown, the uncertainty bound is successfully constructed to enclose the healthy data response. The model is shown to be most accurate, i.e. having the tightest uncertainty bound, in the region before and after the first natural frequency and at the second natural frequency. Conversely, the model is less accurate around the first anti-resonance and after the second natural frequency, indicated by a larger uncertainty bound. Additionally, a noise level of $0.02 \mu\text{m}$ is fit from the data.

Additional insight into the creation of the uncertainty bound is provided by the comparison of the phase responses of the nominal model, healthy data, and uncertainty bound, as shown in Figure 47. This figure illustrates the frequency-dependent phase difference between the input force and output displacement for each of the data sets. For the most part, the phase results mirror the magnitude response results. For example, the bound is tighter in the frequencies below the anti-resonance. Interestingly, the plot shows that the uncertainty bound encloses the entire phase range in the frequencies around the anti-resonance. This is a result of two factors. First, the healthy data points are close to the zero in the complex plane. Second, the structure of the uncertainty is complex additive. As a result, the uncertainty is drawn as a circle in the complex plane around the nominal response in order to enclose the healthy response, at each frequency point. This leads to an uncertainty bound circle enclosing the zero, and, therefore, providing a 360

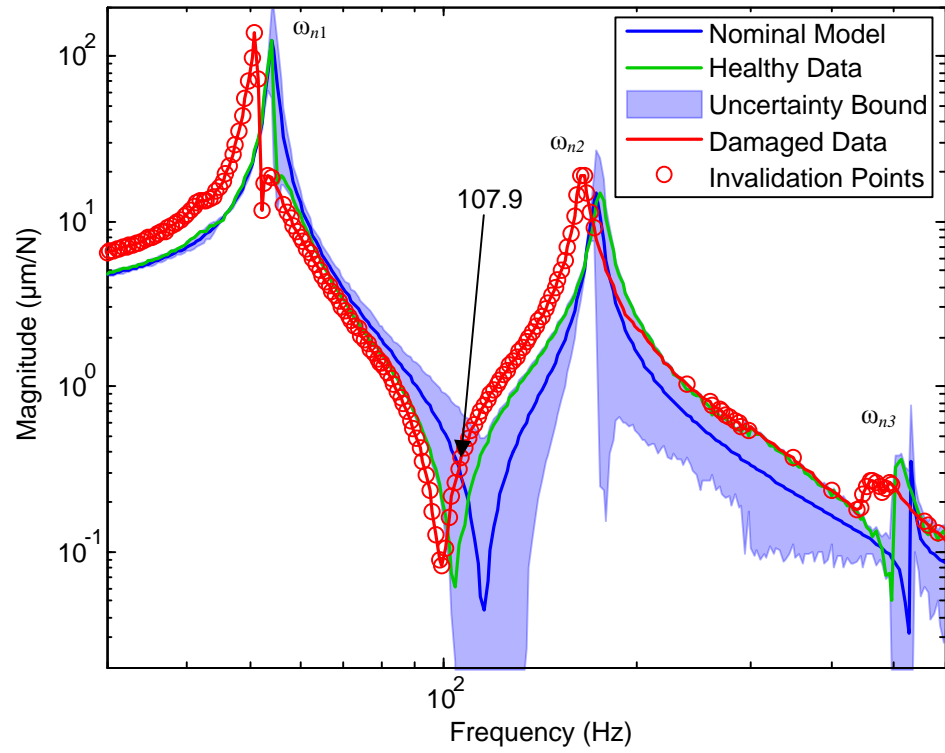


Figure 46 Experimental Non-Rotating Crack Damage Model Validation Results (Magnitude)

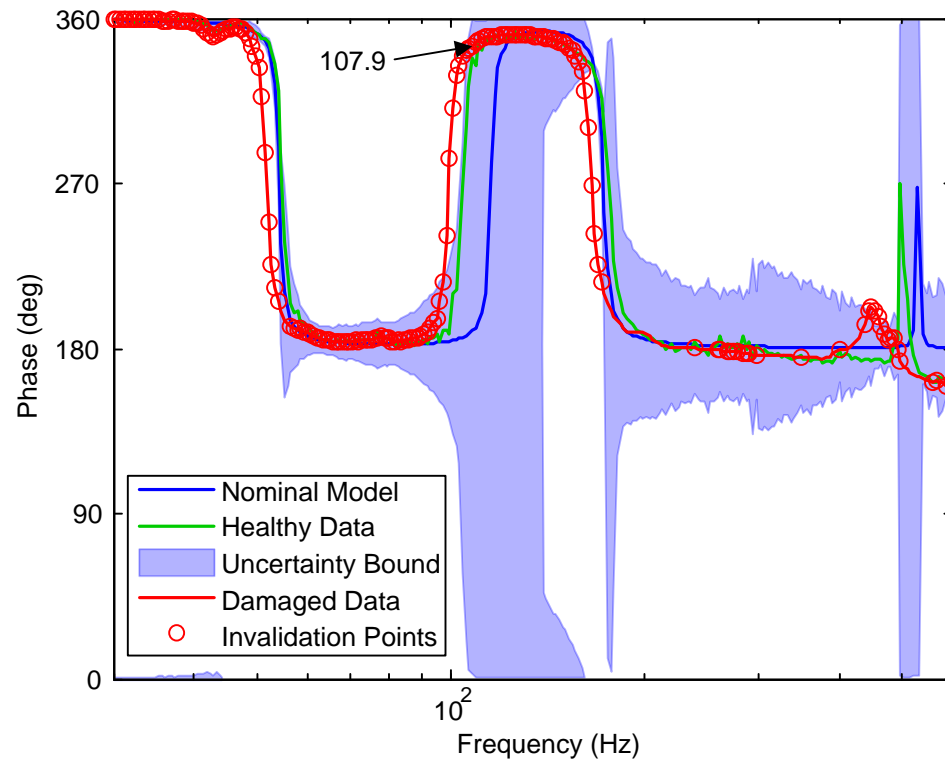


Figure 47 Experimental Non-Rotating Crack Damage Model Validation Results (Phase)

degree uncertainty phase bound. The phase bound also indicates the increased inaccuracy of the model past the second natural frequency.

Next, the damage detection process is completed using the data from the damaged system. The results of this step are also shown in Figures 46 and 47. As shown in the magnitude plot, the damage data indicates a uniform reduction in stiffness across the entire frequency range, reducing all three of the natural frequencies and shifting the entire plot up and to the left. Similarly, the phase response shows the damage data leading the healthy data. As a result, the damage detection step is very successful in indicating the presence of damage at all frequencies up to the second natural frequency. Note that the damage is only detected sporadically at higher frequencies. This is due in most part to the nominal model being less accurate with regards to the healthy data. As a result, the uncertainty bound is larger and is therefore less likely to invalidate a damaged system.

An interesting result of the damage detection step is the presence of points that are identified as fault points which are located within the uncertainty bound on both the magnitude and phase plots. One such point occurs at 107.9 Hz, located just after the frequency where the healthy data crosses over the nominal model in the magnitude plot. The explanation is provided by plotting the complex response of the nominal model, healthy data and damaged data, as shown in Figure 48. The plot illustrates how the uncertainty bound is generated as a circle around the nominal model response, with a radius, or magnitude, large enough to enclose the healthy data at that frequency. Clearly, the damaged data falls outside of the bound. The reason why the point is enclosed on the magnitude and phase plots is two-fold. First, the uncertainty bound extends to a larger magnitude, i.e. is further from the origin, than the damaged data point. Second, the bound

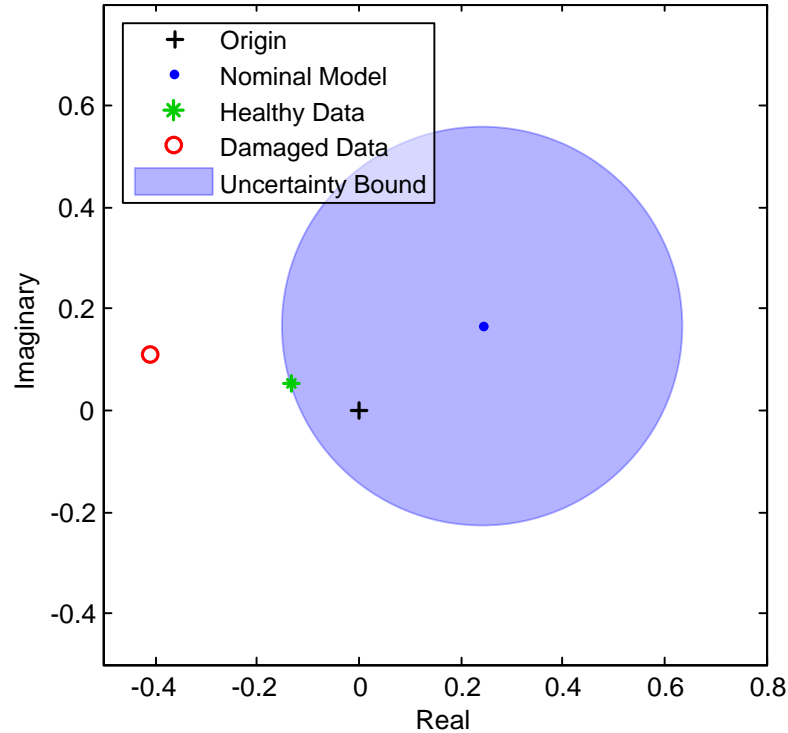


Figure 48 Complex Response at 107.9 Hz

surrounds the origin, meaning that it covers all 360 degrees of the phase plot. Therefore, a response point is able to reside within the bounds in both magnitude and phase but still be indicative of a change in dynamics, or damage. On the contrary, a point will never be considered valid for the model if it falls outside of the bounds. For this case, the issue is a result of the nominal model having a much different phase than the healthy data due to the slight mismodeling of the first anti-resonance. Fortunately, this issue does not have a major impact on the identified change in dynamics due to the damage, as concluded from the simulation.

Finally, the local change in dynamics due to the non-rotating crack is identified through the model-based identification procedure. Recalling the finite element model of the damaged system in Figure 40, the model-based identification is completed with the exogenous input at the eighth node, output at the sixth node, and virtual controller input

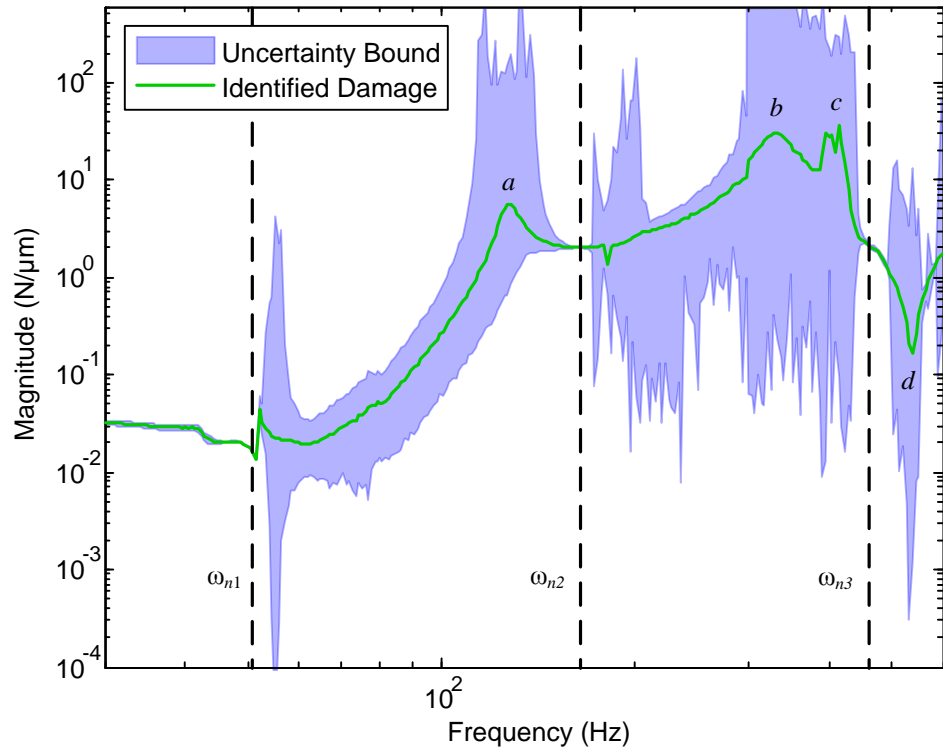


Figure 49 Experimental Non-Rotating Crack Identified Damage Dynamics (Magnitude)

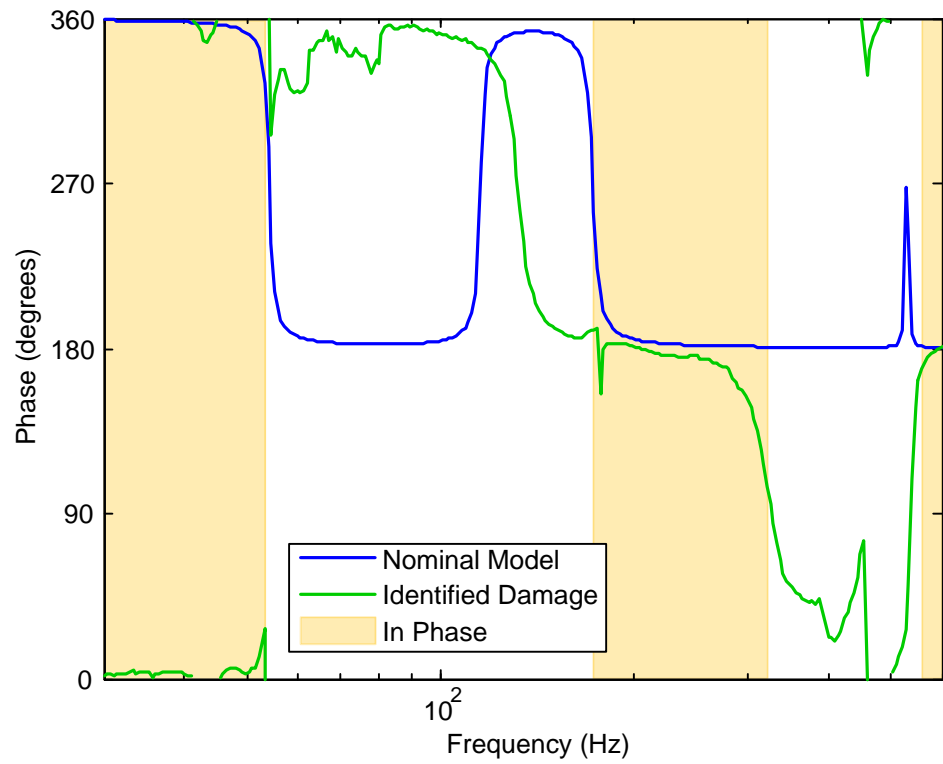


Figure 50 Experimental Non-Rotating Crack Identified Dynamics (Phase)

and output acting at the fourth node, corresponding to the AMB actuator, AMB sensor, and damaged element locations, respectively. Figure 14 shows the control schematic of the technique, for reference. Once again, the technique is completed by direct application of the damaged data as the true system and the nominal model with the addition of the bound uncertainties as the engineering system.

The resulting local change in dynamics due to the crack is shown in Figure 49, which indicates the behavior in the magnitude domain. The magnitude plot illustrates the force response due to a displacement input, similar to the behavior of a spring, across the indicated frequency range. The identified damage dynamics begins similarly to the simulation, shown first in Figure 44. First, the damage acts as a flat reduction in stiffness before the first natural frequency ω_{n1} , similar to a change in spring stiffness. After this point, the experimental behavior begins to deviate from what was predicted by the model. This is expected, due to the simulated damage not matching the experimental observed data, as indicated in Figure 41. After the first natural frequency, the identified damage begins to slope upward in magnitude until reaching the peak a . Between the first and second peak b , the magnitude behavior remains on the increasing trend. This behavior may be indicative of a change in mass along with stiffness. The area between the second and third peak c shows similar behavior. Interestingly, the magnitude falls off at the third natural frequency ω_{n3} before reaching the local minima d . Finally, the dynamics return to the increasing trend.

The local minimum and maximum points a , b , c , and d are of particular interest. These points actually behave as natural frequencies and anti-resonances in the local damage estimate, and the corresponding changes in phase are important in determining whether

or not the damage would represent as an increase or decrease in stiffness at a particular frequency. Specifically, this behavior is determined by the relative phase between the nominal model and the damage dynamics. When the two are in phase, the stiffness of the system decreases, and when the two are 180 degrees out of phase, the stiffness increases. For this case, the phase changes at the indicated frequency points of interest: ω_{n1} , ω_{n2} , b , and d . As shown in Figure 50, the identified damage begins in phase with the nominal model. After the first natural frequency, the two are out of phase until the second natural frequency. At the peak b , the identified damage falls out of phase and enters a region where the phase shifts due to local maxima and minima occur close enough together that they are not able to complete the expected 180 degree phase shifts. The phases finally resettles to back in phase after the local minimum d .

Finally, consider the uncertainty bound. Recall that this uncertainty bound is inherited from the model validation procedure through the direct calculation of the local change in dynamics due to the damage from the uncertain healthy model. As a result, this uncertainty bound may be interpreted as an estimate for the quality of the damage dynamics identification. In conclusion, the estimate appears to be extremely accurate before the first natural frequency as well as at all of the natural frequency locations ω_{n1} , ω_{n2} , and ω_{n3} . Conversely, the identified dynamics seems to be the least reliable at its own peaks a , b , and c . An additional point of inaccuracy occurs where the healthy data abruptly dips after the first natural frequency. Despite these inaccuracies, these bounds appear to be tighter overall than those provided by the simulated results, which will be reviewed in Figure 51. This is due to the experimental damage having a larger effect in

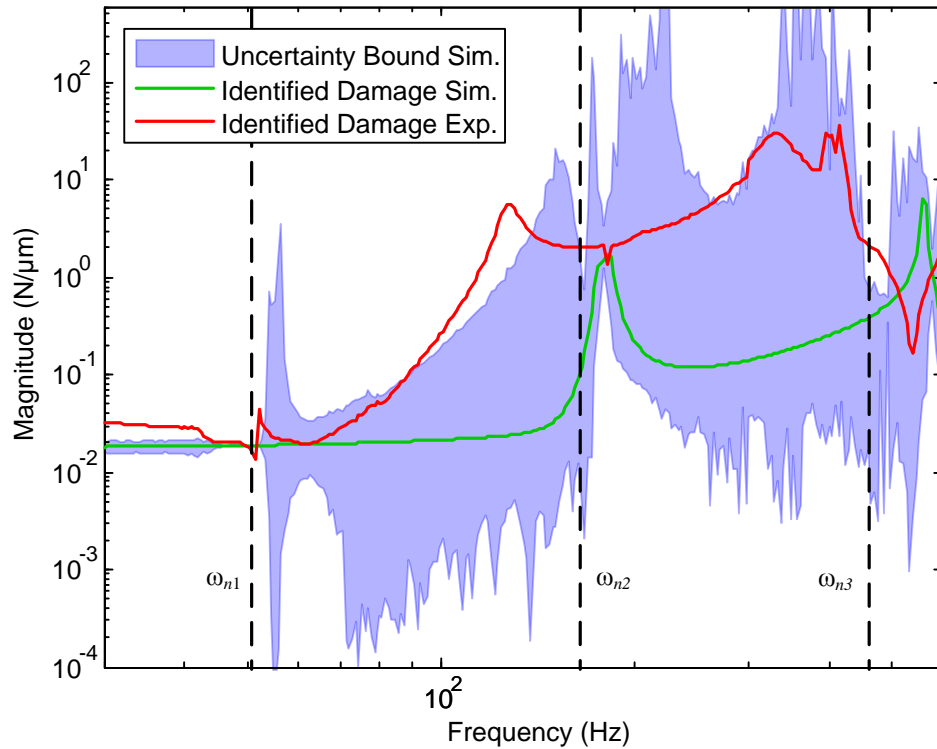


Figure 51 Non-Rotating Crack Identified Damage Dynamics Comparison

the regions where the healthy model is inaccurate. In fact, the larger effect of the damage appears to drown out these errors.

The final plot for this experiment provides a comparison between the magnitude responses of the experimentally identified damage and the simulated identified damage. Additionally, the uncertainty bound obtained from the simulation is included for reference. Once again, this plot indicates the change in force due to a displacement over the indicated frequency range. The first conclusion that can be drawn from this figure is that the simulation does not accurately predict the effect of the cut in the shaft. However, the overall trends are similar. First, both the experimental and simulated damages exhibit a mostly flat reduction in stiffness below the first natural frequency. Next, the behaviors deviate greatly between the first natural frequency and the first peak in the experimental damage dynamics. While the simulation shows a flat reduction of stiffness in this region,

the experiment reveals a large positive slope. This appears to be due to the model incorrectly predicting the change in stiffness in this region, as shown by the comparison of the damaged model and the damaged data in Figure 41. Finally, the region between the first and second peaks in damage dynamics indicates a slight upslope in magnitude. So aside from the behavior in the second region, the damages appear to follow the same trends, with the peaks for the experimental case moved to lower frequencies, presumably following the difference in the peak locations of the simulated and experimental damaged data sets.

In addition to comparing the magnitude responses, the experimental identified damage may be compared to the simulated uncertainty bound. Such a comparison indicates where the simulated damage estimate deviates from the experimental to a greater extent than is predicted by the inaccuracy of the healthy model. Again, this discrepancy is most apparent between the first and second natural frequencies.

4.7 Conclusion

This experiment illustrated the practical application of the developed damage identification approach. The method was shown to be effective at detecting and identifying the change in dynamics due to an EDM cut in a non-rotating shaft. The next chapter will add rotating to the experiment, which will reduce the effect of the crack on the shaft, leading to a more difficult to detect source of damage.

CHAPTER V

IDENTIFICATION OF A BREATHING CRACK IN A SHAFT

This chapter will cover the second experimental damage identification example: identification of a breathing crack in a rotating system. However, before the damage identification procedure is presented, the breathing crack will be introduced in Section 1 and simulated in Section 2. Section 3 will cover illustrative results from the breathing crack simulation in order to present some key effects that a breathing crack will have on a rotor. Following the breathing crack introduction, the structure will follow the damage identification procedure as outlined in Section 3.3. First, in Section 4, the nominal model will be developed. This will cover the design of the rotating finite element model. Next, the damage identification problem procedure will be reviewed in Section 5. After that, the results of the identification of a simulated breathing crack are presented in Section 6. In Section 7, the experimental results will be presented and compared with the simulation results. Finally, the conclusions from the two trials will be covered in the closing section.

For the analog to the damage identification procedure as outlined in Section 3.3: Step 1- creation of the nominal model, is covered in the development of the healthy system in Section 4. Step 2- fitting the noise to the healthy data, is covered in the simulation results

in Section 6. Step 3- bounding the uncertainty to create the uncertain healthy model, is covered in simulation in Section 6 and in experiment in Section 7. Step 4- detecting the damage, is also covered in Sections 6 and 7 for the simulation and experiment, respectively. Step 5- identifying the local damage dynamics, is also split into Sections 6 and 7 for the simulation and experiment, respectively.

No change has been made to the experimental apparatus used for the non-rotating case. As a result, the reader is referred to Section 4.1 for a complete description of the test setup. Also, the damage imparted on the system is the same filled, wire electrical discharge machining cut. Therefore, Section 4.2 should be referred to for the damage description. Despite the fact that the same damage source is utilized, the novelty in the experiment is provided by the rotation of the shaft, which provides the crack's breathing behavior.

5.1 Introduction to a Breathing Crack

An understanding of the definition of a breathing crack is tied to the concept of weight dominance. The assumption of weight dominance proposes that the static deflection of the rotor due to its own weight is greater than the magnitude of any vibrations seen during operation. A conceptual sketch for this concept is illustrated in Figure 52. As shown, the rotor rests below the bearing center line, causing a bow in the shaft and a differing axis of rotation. As a result of this bow, the transverse crack will be fully open when facing downward. Conversely, the bow will cause the crack to close when it faces upward. When weight dominance is not the case and vibrations in the rotor exceed the static deflection of the rotor, the crack will not open and close in a predictable, cyclical manner.

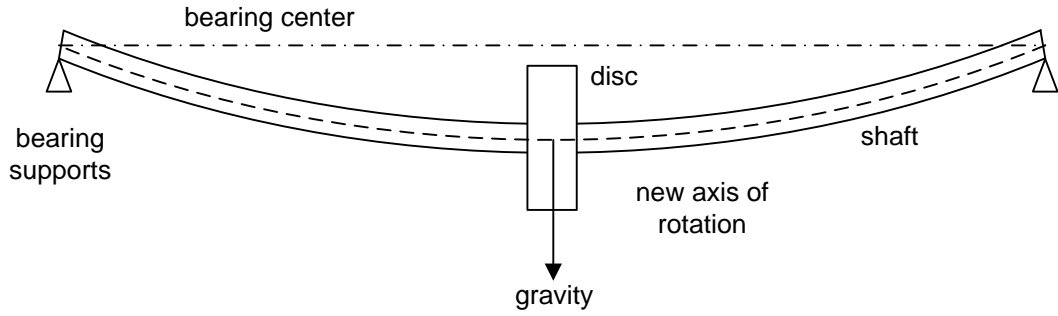


Figure 52 Illustration of Weight Dominance Concept

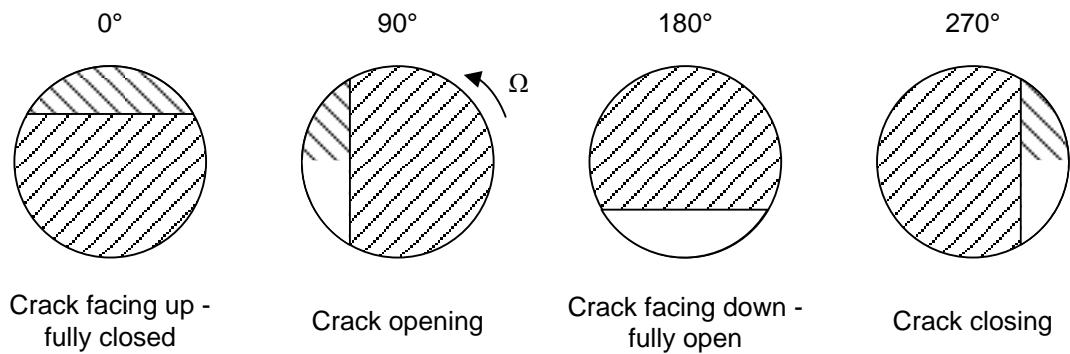


Figure 53 Crack Breathing in a Rotation Cycle

The full cycle of crack opening to closing is presented in Figure 53. For this case, 0 degrees is taken as the positive vertical direction and rotation occurs counter-clockwise. As shown, the crack begins the rotation cycle at 0 degrees fully closed due to the bend in the shaft causing the compression which forces the cracked faces together. At 90 degrees, the crack begins to open as the cracked surface leaves the top center contact point. At 180 degrees, the crack becomes fully open as the bend in the shaft causes enough tension between the crack faces to separate them completely. At 270 degrees, the crack closes as the surfaces are split between tension and compression. Finally, the cycle is completed as the crack returns to the fully closed position.

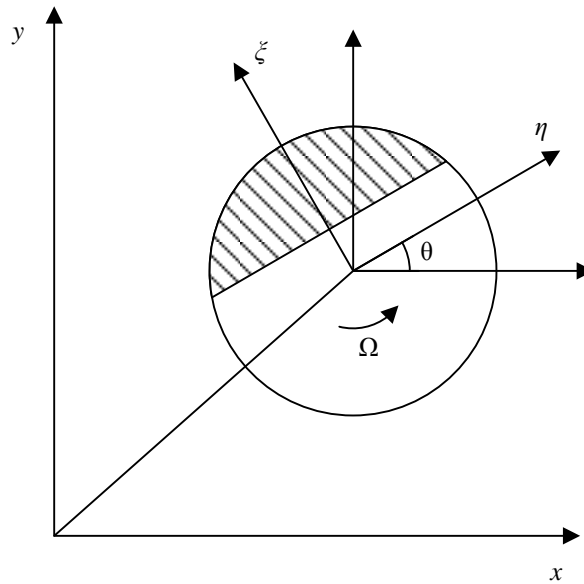


Figure 54 Crack Shown in Rotating (η, ζ) and Fixed (x, y) Coordinates

The analytical equation of motion for a rotor-bearing system with a breathing crack may be expressed in rotating or fixed coordinates, with rotating coordinates being the most common choice. The reason for this choice is that the crack is opening and closing about the new axis of rotation, as seen in Figure 52. A more detailed look at the rotating and fixed coordinate definitions is shown in Figure 54. In the figure, the x and y axes define the fixed coordinate system, whereas the ζ and η axes define the rotating coordinate system as the directions perpendicular and parallel to the crack edge, respectively. The coordinate systems are related by the angle of rotation of the shaft θ , rotating at the speed Ω . For the analysis of typical systems, the rotating crack behavior is transformed to the fixed coordinate system. This is mainly due to axisymmetric rotors and asymmetric supports being commonplace.

The solution for the rotor with a breathing crack begins with a fundamental equation which is an expression of Newton's 2nd law for the rotor's FE matrices:

$$\mathbf{M}\ddot{\mathbf{q}} + (\mathbf{D} + \mathbf{G})\dot{\mathbf{q}} + \mathbf{K}\mathbf{q} = \mathbf{Q}_u + \mathbf{W} \quad (5.1)$$

where \mathbf{M} , \mathbf{D} , \mathbf{G} , and \mathbf{K} are the system mass, damping, skew-symmetric gyroscopic, and stiffness matrices, respectively, and \mathbf{Q}_u and \mathbf{W} are the unbalance and weight force vectors, respectively. The crack dynamics will manifest itself in a change in the stiffness matrix. Derivation will follow the form presented in [84].

Particularly, the stiffness of the cracked rotor in the rotating coordinates is defined by the relationship:

$$\tilde{\mathbf{K}}_{cr} = \tilde{\mathbf{K}}_0 - \tilde{\mathbf{K}}_c(\theta) \quad (5.2)$$

where $\tilde{\mathbf{K}}_0$ is the healthy stiffness and $\tilde{\mathbf{K}}_c(\theta)$ is the reduction in stiffness due to the crack, both defined in rotating coordinates as denoted by $\tilde{\cdot}$. Note that the definition for θ is consistent with Figure 54 and determines the extent to which the crack is open. More details on specific models for $\tilde{\mathbf{K}}_c(\theta)$ will be given in the following section.

Transformation from the rotating to fixed coordinate system is defined by the matrix:

$$\mathbf{T}(\Omega t) = \begin{bmatrix} \cos(\Omega t) & -\sin(\Omega t) \\ \sin(\Omega t) & \cos(\Omega t) \end{bmatrix} \quad (5.3)$$

where Ωt provides an alternative definition for the angle of rotation as a function of time.

Applying this transformation to the cracked stiffness matrix leads to:

$$\mathbf{K}_{cr} = \mathbf{T}(\Omega t)\tilde{\mathbf{K}}_0\mathbf{T}(\Omega t)^T - \mathbf{T}(\Omega t)\tilde{\mathbf{K}}_c(\theta)\mathbf{T}(\Omega t)^T \quad (5.4)$$

Therefore, the cracked stiffness in fixed coordinates may be expressed as:

$$\mathbf{K}_{cr} = \mathbf{K}_0 - \mathbf{K}_c(\theta, t) \quad (5.5)$$

Combining the cracked stiffness definition with Equation 5.1 leads to the equation:

$$\mathbf{M}\ddot{\mathbf{q}}_{dy} + (\mathbf{D} + \mathbf{G})\dot{\mathbf{q}}_{dy} + (\mathbf{K}_0 - \mathbf{K}_c(\theta, t))(\mathbf{q}_{st} + \mathbf{q}_{dy}) = \mathbf{Q}_u + \mathbf{W} \quad (5.6)$$

In this definition, the displacement vector \mathbf{q} has been separated into the static and dynamic components \mathbf{q}_{st} and \mathbf{q}_{dy} , respectively, in order to isolate the static contribution due to gravity. As a result $\ddot{\mathbf{q}} = \ddot{\mathbf{q}}_{dy}$ and $\dot{\mathbf{q}} = \dot{\mathbf{q}}_{dy}$.

In order to simplify the equation of motion, two assumptions are utilized. First is the assumption that the steady state deflection is assumed to be constant. While the deflection due to gravity is actually changing due to the stiffness \mathbf{K}_c varying in time, the stiffness reduction due to the crack is typically much less than the healthy stiffness $\|\mathbf{K}_c(\theta, t)\| \ll \|\mathbf{K}_0\|$. Therefore, it is assumed:

$$\mathbf{K}_0 \mathbf{q}_{st} = \mathbf{W} \quad (5.7)$$

leading to the removal of the static deflection and weight terms from the full equation:

$$\mathbf{M}\ddot{\mathbf{q}}_{dy} + (\mathbf{D} + \mathbf{G})\dot{\mathbf{q}}_{dy} + (\mathbf{K}_0 - \mathbf{K}_c(\theta, t))\mathbf{q}_{dy} = \mathbf{Q}_u \quad (5.8)$$

Second, the weight dominance assumption is employed. Recall that the assumption states that the static deflection is much larger than the deflection due to the vibration of the system. As a result, the opening and closing of the crack is guaranteed by the static deflection and the rotation angle, which is defined by the constant rotation speed. This gives the final, simplified form of the equation of motion as:

$$\mathbf{M}\ddot{\mathbf{q}}_{dy} + (\mathbf{D} + \mathbf{G})\dot{\mathbf{q}}_{dy} + (\mathbf{K}_0 - \mathbf{K}_c(t))\mathbf{Q}_{dy} = \mathbf{Q}_u \quad (5.9)$$

The final step in finding the frequency response is to provide a definition for the time-dependent reduction in stiffness due to the crack, also known as the breathing crack model. The hinge model for a breathing crack was first proposed by Gasch [85]. In addition to being the first model, it is also the simplest. The hinge model switches between the stiffness of the shaft when the crack is open and the stiffness when the crack is closed, with each lasting for half of the rotation. The result is the stiffness definition:

$$\mathbf{k}_R(\theta) = \begin{bmatrix} k_\xi(\theta) & 0 \\ 0 & k_\eta(\theta) \end{bmatrix} \quad (5.10)$$

$$k_\xi(\theta) = \begin{cases} k_0 & -\frac{\pi}{2} \leq \theta < \frac{\pi}{2} \\ k_\xi & \frac{\pi}{2} \leq \theta < \frac{3\pi}{2} \end{cases} \quad (5.11)$$

$$k_\eta(\theta) = \begin{cases} k_0 & -\frac{\pi}{2} \leq \theta < \frac{\pi}{2} \\ k_\eta & \frac{\pi}{2} \leq \theta < \frac{3\pi}{2} \end{cases} \quad (5.12)$$

with the rotating stiffness \mathbf{k}_R , nominal healthy stiffness for when the crack is closed k_0 , and stiffnesses k_ξ and k_η for the open crack.

Later, Mayes and Davies [86][87] refined the breathing crack model to include a cosine function allowing for a smoother transition between the fully-open and fully-closed crack states. This change allowed for intermediate behavior between the crack being fully-opened and fully-closed, resulting in increased accuracy for deeper cracks. The resulting rotating stiffness is defined by the following equation:

$$k_R(\theta) = \frac{1}{2}(k_0 + k_c) + \frac{1}{2}(k_0 - k_c) \cos \theta \quad (5.13)$$

with different k_c values for the ξ and η -directions.

Finally, the method of Jun et al. [88] found an intermediate steering function with numerical evaluation of fracture mechanics theory. The result was a definition for the crack which included both cross-coupling and coefficients calculated for individual crack geometries. The general rotating stiffness was defined as:

$$\mathbf{k}_R = \begin{bmatrix} k_{\xi\xi}(\theta) & k_{\xi\eta}(\theta) \\ k_{\eta\xi}(\theta) & k_{\eta\eta}(\theta) \end{bmatrix} \quad (5.14)$$

with directional stiffness coefficients $k_{\xi\xi}$ and $k_{\eta\eta}$ defined in rotating coordinates, as shown in Figure 54, for the ξ - and η -directions, along with the similarly defined cross-coupled coefficients $k_{\xi\eta}$ and $k_{\eta\xi}$. The element $k_{\xi\xi}$ is defined by the series:

$$k_{\xi\xi}(\theta) = b_0 + b_1 \cos \theta + b_2 \cos(2\theta) + b_3 \cos(3\theta) + b_4 \cos(4\theta) + \dots \quad (5.15)$$

with the coefficients b_0, b_1, b_2, b_3, b_4 , etc. defined for a particular cut geometry. Additionally, $k_{\eta\eta}$ was defined by a similar series with different coefficients due to asymmetry in the cut geometry. Similarly, the cross-coupled stiffness coefficients are defined by the series:

$$k_{\xi\eta}(\theta) = a_1 \sin \theta + a_2 \sin(2\theta) + a_3 \sin(3\theta) + a_4 \sin(4\theta) + \dots \quad (5.16)$$

Once again, the coefficients a_1, a_2, a_3, a_4 , etc. were defined for the particular cut geometry. The definition for the final off-diagonal element $k_{\eta\xi}$ was equivalent, maintaining symmetry in the stiffness matrix.

For comparison to this experiment, the Mayes and Davies breathing definition is employed for three reasons. First, the Mayes and Davies model has been shown to be accurate with deep cracks, such as the 40% diameter cut in the present study. Second, the breathing function is generalized for all crack depths, so individual derivation is not required. Third, comparisons to the experimental damaged results have been favorable as will be demonstrated later in this chapter. For additional information, a detailed comparison for the different crack models may be found in Penny and Friswell [89].

5.2 The Breathing Crack in Simulation

Simulation of the rotor-bearing system with a breathing crack begins with updating the healthy model to include the effect of the crack. To begin, recall the full cracked rotor equation developed in the previous section, Eq. 5.6. In simulation, the easiest way to

apply this change in stiffness is to append the rotor system state-space obtained from the rotordynamic finite element technique. For reference, the healthy state-space model is presented:

$$\begin{aligned}\dot{\mathbf{q}} &= \mathbf{A}\mathbf{q} + \mathbf{B}\mathbf{u} \\ \mathbf{y} &= \mathbf{C}\mathbf{q}\end{aligned}\tag{5.17}$$

where the unbalance, gravity, and experimental sine sweep force have been combined into a vector of external inputs \mathbf{u} . The change in stiffness is applied by first modifying the input and output matrices \mathbf{B} and \mathbf{C} , respectively, to act as location selector matrices. In other words, these matrices will provide the mapping required to manipulate the stiffness portion of the rotor system's dynamic \mathbf{A} matrix. For this case, the change will be induced on the zeroth order term of the system dynamics, i.e. the \mathbf{q} term in Equation 5.17, acting at the two nodes of the damaged element. As a result, this will impart a change on the stiffness contribution of the cracked element. The state-space model is updated to include the crack dynamics:

$$\begin{aligned}\dot{\mathbf{q}} &= [\mathbf{A} + \mathbf{B}_c \mathbf{K}_c(t) \mathbf{C}_c] \mathbf{q} + \mathbf{B}\mathbf{u} \\ \mathbf{y} &= \mathbf{C}\mathbf{q}\end{aligned}\tag{5.18}$$

where \mathbf{B}_c and \mathbf{C}_c indicate the crack locations in the \mathbf{B} and \mathbf{C} matrices. Furthermore, the state-space model may be redefined to include the cracked dynamic matrix \mathbf{A}_c as:

$$\begin{aligned}\dot{\mathbf{q}} &= \mathbf{A}_c \mathbf{q} + \mathbf{B}\mathbf{u} \\ \mathbf{y} &= \mathbf{C}\mathbf{q}\end{aligned}\tag{5.19}$$

Finally, the opening and closing of the crack is defined by the equation:

$$\mathbf{K}_c(t) = f(t) \mathbf{T}(\Omega t) \tilde{\mathbf{K}}_c \mathbf{T}(\Omega t)^T\tag{5.20}$$

This breathing function is defined by three new terms. The first is the steering function $f(t)$, which dictates the opening and closing of the crack. For this experiment, the

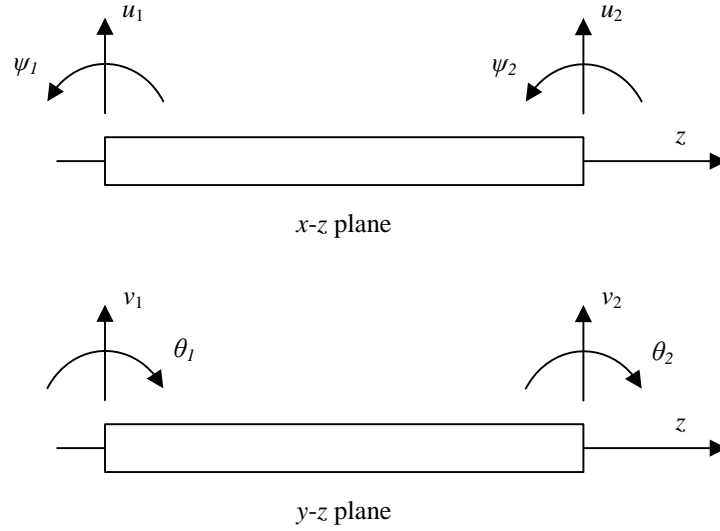


Figure 55 Local Coordinates of the Finite Element [84]

Mayes and Davies model is employed, which is consistent with Equation 5.10. Alternatively, the breathing function can be expressed on its own such that the reduction of stiffness due to the crack follows:

$$f(t) = \frac{1 + \cos(\theta)}{2} \quad (5.21)$$

The next term is the change in stiffness due to the fully open crack in the rotating frame $\tilde{\mathbf{K}}_e$. For application to a finite element model, consider the stiffness matrix for an Euler-Bernoulli shaft element as defined in Friswell et al. [84]:

$$\mathbf{K}_e = \frac{E_e I_e}{l_e^3} \begin{bmatrix} 12 & 0 & 0 & 6l_e & -12 & 0 & 0 & 6l_e \\ 0 & 12 & -6l_e & 0 & 0 & -12 & -6l_e & 0 \\ 0 & -6l_e & 4l_e^2 & 0 & 0 & 6l_e & 2l_e^2 & 0 \\ 6l_e & 0 & 0 & 4l_e^2 & -6l_e & 0 & 0 & 2l_e^2 \\ -12 & 0 & 0 & -6l_e & 12 & 0 & 0 & -6l_e \\ 0 & -12 & 6l_e & 0 & 0 & 12 & 6l_e & 0 \\ 0 & -6l_e & 2l_e^2 & 0 & 0 & 6l_e & 4l_e^2 & 0 \\ 6l_e & 0 & 0 & 2l_e^2 & -6l_e & 0 & 0 & 4l_e^2 \end{bmatrix} \quad (5.22)$$

with element stiffness \mathbf{K}_e , modulus of elasticity E_e , second moment of inertia I_e , and length l_e . The stiffness matrix is defined for the coordinate vector illustrated in Figure 55:

$$[u_1, v_1, \theta_1, \psi_1, u_2, v_2, \theta_2, \psi_2]^T \quad (5.23)$$

The next step is to define the change in stiffness for a particular crack depth. To this end, Mayes and Davies [87] proposed defining the stiffness reduction as a change in second moment of inertia for the directions perpendicular and parallel to the crack faces I_ξ and I_η , respectively. Using these values in Equation 5.22 results in the updated stiffness matrix:

$$\tilde{\mathbf{K}}_c = \frac{E_e}{l_e^3} \begin{bmatrix} 12I_\xi & 0 & 0 & 6l_e I_\xi & -12I_\xi & 0 & 0 & 6l_e I_\xi \\ 0 & 12I_\eta & -6l_e I_\eta & 0 & 0 & -12I_\eta & -6l_e I_\eta & 0 \\ 0 & -6l_e I_\eta & 4l_e^2 I_\eta & 0 & 0 & 6l_e I_\eta & 2l_e^2 I_\eta & 0 \\ 6l_e I_\xi & 0 & 0 & 4l_e^2 I_\xi & -6l_e I_\xi & 0 & 0 & 2l_e^2 I_\xi \\ -12I_\xi & 0 & 0 & -6l_e I_\xi & 12I_\xi & 0 & 0 & -6l_e I_\xi \\ 0 & -12I_\eta & 6l_e I_\eta & 0 & 0 & 12I_\eta & 6l_e I_\eta & 0 \\ 0 & -6l_e I_\eta & 2l_e^2 I_\eta & 0 & 0 & 6l_e I_\eta & 4l_e^2 I_\eta & 0 \\ 6l_e I_\xi & 0 & 0 & 2l_e^2 I_\xi & -6l_e I_\xi & 0 & 0 & 4l_e^2 I_\xi \end{bmatrix} \quad (5.24)$$

where the change in second moment of inertia for each axis is defined as:

$$\Delta I = I_0 \left(\frac{\frac{R}{l}(1-\nu^2)F(\alpha)}{1 + \frac{R}{l}(1-\nu^2)F(\alpha)} \right) \quad (5.25)$$

where I_0 is the healthy second moment of inertia, R is the shaft radius, l is the length of the section, ν is the Poisson's ratio of the material, α is the non-dimensional crack depth defined as the ratio of the depth to the shaft radius, and $F(\alpha)$ is the compliance function.

The compliance function is defined for different depths of cut with $F_\xi(\alpha) = 3.0$ and

$F_\eta(\alpha) = 0.47$ for a 40% diameter cut. The material properties for the test rig are included

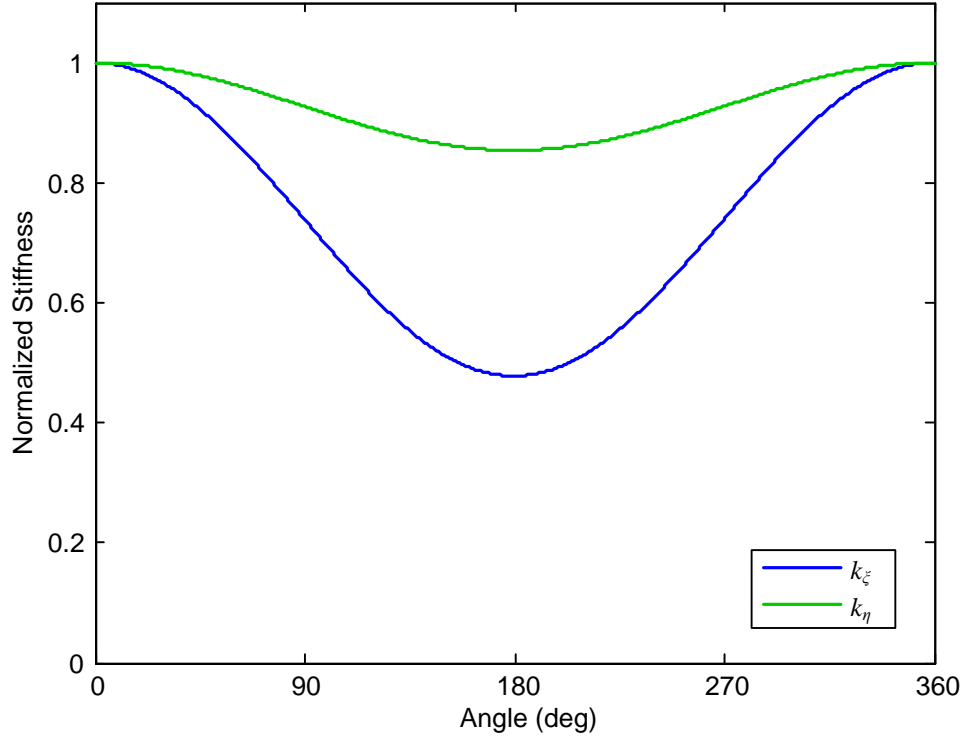


Figure 56 Change in Normalized Stiffness due to Mayes and Davies Breathing Model

with the FE definition in the Appendix. Using these values in Equation 5.25 leads to reductions of 52.2% in the ζ -direction and 14.6% in the η -direction.

The final term in the breathing function is the transformation from rotating to stationary coordinates $\mathbf{T}(\Omega t)$. Due to size of $\tilde{\mathbf{K}}_c$, the transformation matrix needs to be expanded to an eight by eight matrix. This is done by expanding the matrix and repeating the two by two $\mathbf{T}(\Omega t)$ defined in Equation 5.3 four times as a block diagonal:

$$\mathbf{T}(\Omega t) = \begin{bmatrix} \mathbf{T}_{2 \times 2} & 0 & 0 & 0 \\ 0 & \mathbf{T}_{2 \times 2} & 0 & 0 \\ 0 & 0 & \mathbf{T}_{2 \times 2} & 0 \\ 0 & 0 & 0 & \mathbf{T}_{2 \times 2} \end{bmatrix} \quad (5.26)$$

The resulting change in stiffness due to the breathing crack in rotating coordinates is illustrated in Figure 56 for one full rotation cycle. The plot indicates maximum normalized stiffness reductions of 52.2% in the ζ direction and 14.6% in the η direction. Note that the plot indicates the convention that the crack will begin as fully closed in simulation.

5.3 Illustrative Results from the Simulation

This section will present some results illustrative of the effect of a breathing crack in a rotor. All parameters for the simulation of the cracked rotor model previously discussed are taken from the experimental system. A detailed explanation of the model and the simulation parameters will be presented in Section 5.4. While a particular model is presented, the purpose of this section is to give an introduction to the behaviors typical of a breathing crack in a rotor.

The first set of results from the simulation is the effect of the crack on the orbit. Figure 57 below shows the horizontal and vertical displacements at the AMB sensor location in μm for one full rotation. Note that the static deflection due to gravity has been removed from the plot. A 0.2 g*m unbalance is placed at the disc node. The unbalance begins facing downward, whereas the crack is facing upward and closed at $t=0$. The healthy orbit is a perfect circle, as one would expect from an axially symmetric rotor system excited only with an unbalance. Conversely, the crack causes a noticeable deformation in the orbit shape. Interestingly, the cracked orbit alternates between being within and outside of the healthy rotor orbit, with the majority of the time being spent outside of the original, healthy orbit. The particular cracked orbit shape is due to both the unbalance magnitude and offset angle relative to the crack. A larger unbalance magnitude smooths out the

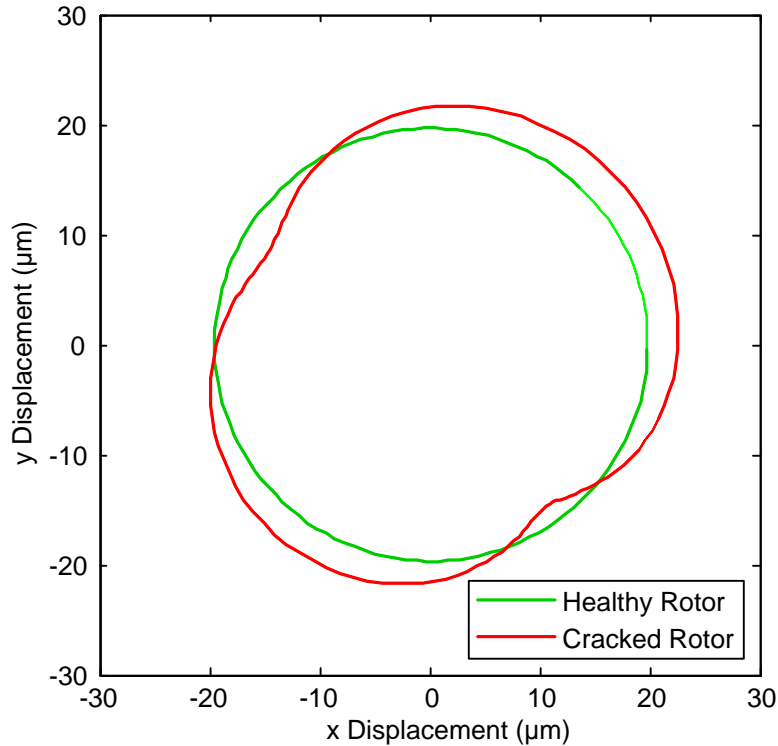


Figure 57 Simulated Healthy and Cracked Orbits at 1000 rpm

cracked behavior, whereas a smaller unbalance magnitude would lead to interior loops in the cracked orbit.

Additional insight into the effect of the crack on the rotor motion is provided by the frequency spectrum plots in Figure 58. The figure shows the response for three different operating cases: the healthy shaft rotating at 1000 rpm, the damaged shaft rotating at 1000 rpm in log and linear magnitude scales, and the damaged shaft rotating at 750 rpm.

The first plot shows the frequency spectrum of the healthy shaft. As expected, the healthy shaft response has a non-zero magnitude occurring at the running speed, 1X. This is due to the healthy rotor being a linear system, meaning that the frequency of the output response will mirror the input frequency, which, in this case, is the running speed. This frequency response is consistent with the circular orbit shown in Figure 57.

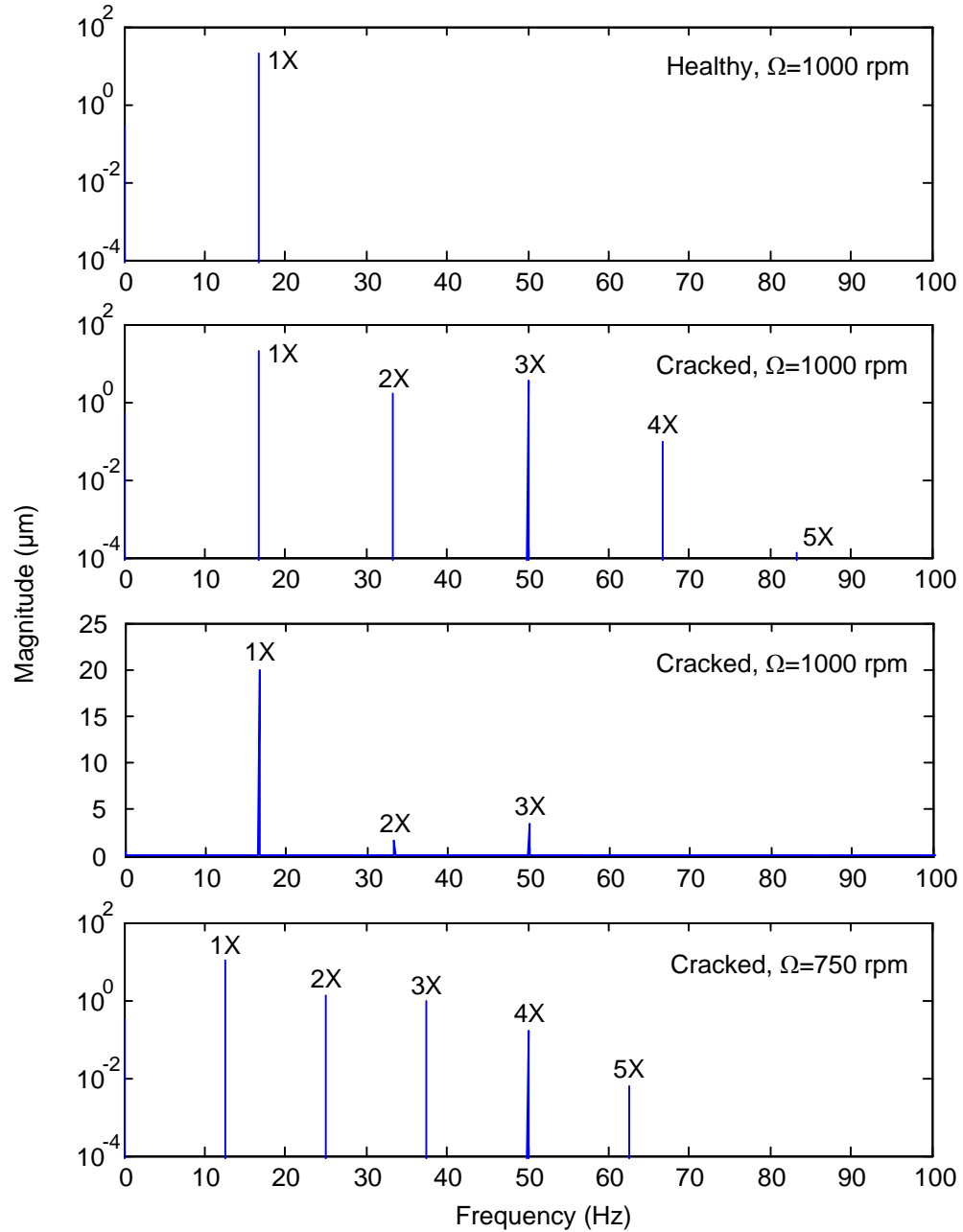


Figure 58 Simulated Healthy and Cracked Frequency Spectrum

The second plot shows the frequency response of the cracked shaft at 1000 rpm. In addition to the magnitude at the running speed, this output contains non-zero magnitudes which occur at integer multiples of the running speed. This behavior is typical of cracked rotors, with nonlinearity brought on by the asymmetry in shaft due to different reductions

in stiffness perpendicular and parallel to the rotating crack face. In fact, these integer multiples will propagate indefinitely, generally following a trend of decreasing magnitudes, though only a limited number will be visible in experiment due to the noise floor.

For a different view of the effect of these integer multiples, the third plot shows the same magnitudes on a linear scale. This plot clearly indicates that the 1X component is the predominant frequency feature, with the contributions of the 2X and 3X remaining as the only other responses distinguishable from the 0 magnitude line. Therefore, these are the only effects which will be visible in the orbit plot. Interestingly, this magnitude plot illustrates a larger contribution from the 3X component than the 2X, which deviates from the decreasing magnitude trend. While this is somewhat counter-intuitive, the reason for this occurrence is a simple one: the 3X frequency is approaching the first critical speed of the damaged system, predicted at 55 Hz.

In order to present a more typical frequency result, the rotor is simulated at 750 rpm and the magnitude response is included in the fourth plot. As shown, this response exhibits the expected decreasing magnitude as frequency increases. Interestingly, the 4X magnitude does not see as large of an excitation from being near the first critical speed. This is likely due to decreased energy in the higher integer multiples.

5.4 Reviewing the Healthy Model

To begin the damage identification experiment, an accurate model of the nominal healthy system is required. Similar to the previous chapter, the nominal model is created using finite element software from [84]. The shaft is comprised of Timoshenko beam

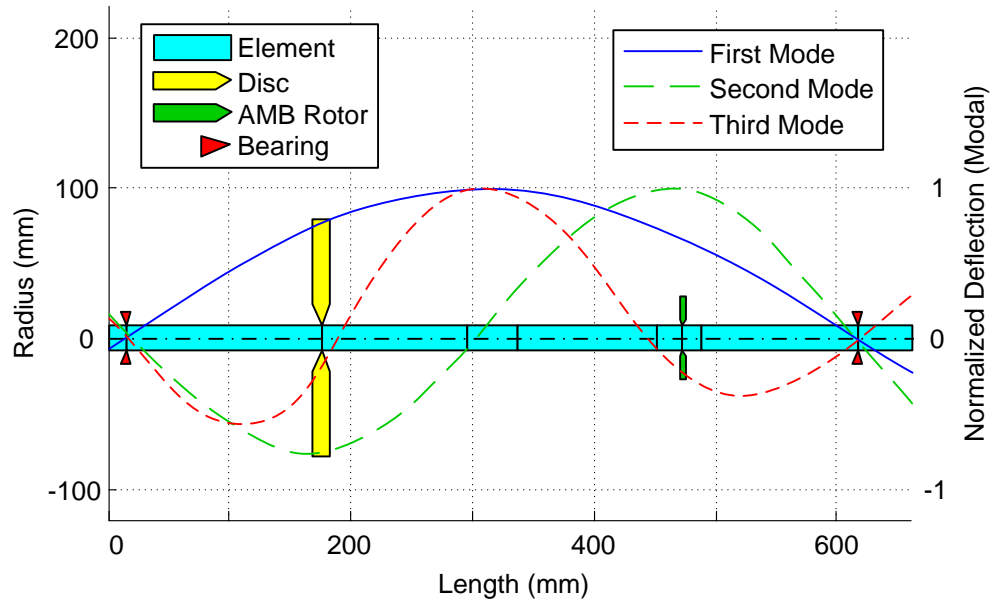


Figure 59 Finite Element Discretization of Rotor System with Mode Shapes

elements. Modal damping is utilized, and is manually tuned to each natural frequency peak individually.

The disc, AMB rotor, and bearings are defined as additional features in the model. The support bearings are defined by axisymmetric point stiffness and damping. Both the disc and AMB rotor are defined by mass and transverse and polar moments of inertia. These elements are applied at the nodes located at their centers of mass. The layout for the finite element model, including the first three mode shapes for reference, is shown in Figure 59. More details on this figure can be found in Section 4.3, where it was first introduced.

Up to this point, the model contains the same components as the non-rotating case from the previous chapter, which can be taken as a general structure. However, running speed is now taken into account. This change allows for the gyroscopic effect to be included in the model. The result is the standard rotordynamic equation of motion:

$$\mathbf{M}\ddot{\mathbf{q}} + (\mathbf{D} + \mathbf{G}(\Omega))\dot{\mathbf{q}} + \mathbf{K}\mathbf{q} = \mathbf{Q}_e \quad (5.27)$$

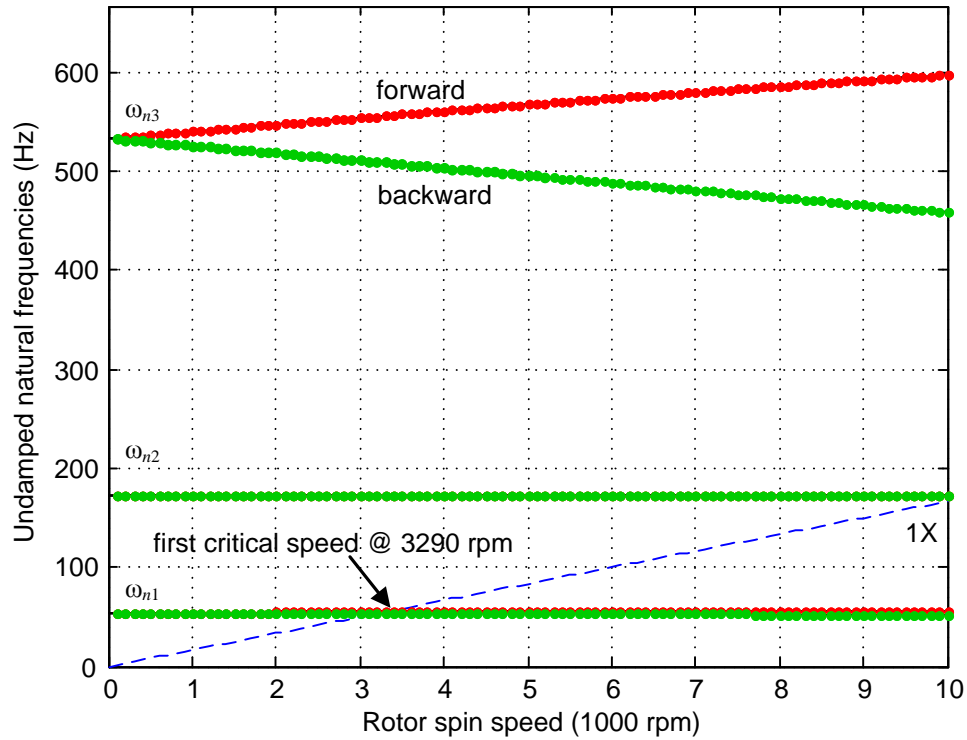


Figure 60 Campbell Diagram with Forward Modes (Red) and Backward Modes (Green)

where \mathbf{M} is the mass matrix, \mathbf{C} is the damping matrix, $\mathbf{G}(\Omega)$ is the speed-dependent gyroscopic matrix, \mathbf{K} is the stiffness matrix, and \mathbf{Q}_e is the external excitation, along with the displacement \mathbf{q} , velocity $\dot{\mathbf{q}}$ and acceleration $\ddot{\mathbf{q}}$ vectors.

The effect of including the gyroscopic effect to the model is shown by the Campbell diagram in Figure 60. In general, the Campbell diagram illustrates the relationship between the rotating speed and the natural frequencies. As shown, the gyroscopic effect leads to a bifurcation in the natural frequencies between the forward and backward modes. Additionally, multiples of the running speed are shown. Of particular interest are the points where the natural frequencies of the forward modes cross the running speed, known as the critical speeds. These critical speeds represent the operating conditions where the machine is predicted to see the largest vibrations due to unbalance. Only the

forward modes are of particular interest due to the fact that the backward modes are rarely observed, and are only reported to be seen under special circumstances.

This particular Campbell diagram provides some insight into the behavior of the model. First, very little bifurcation occurs in the first two natural frequencies. This is due to the location of the disc relative to the mode shapes - occurring where the mode shapes have less curvature. In fact, the disc nearly occurs at a curvature minimum for the second mode, leading to nearly zero curvature and no measurable splitting. Alternatively, the third mode shows significant splitting, which can be attributed to the disc being located close to a zero in the mode shape which would be the position of maximum curvature. Finally, the only critical speed occurring within the 0-10,000 rpm running speed range is the first, which is predicted to occur at 3290 rpm.

The accuracy of the model is checked with the experimental healthy data as shown in Figure 61 and Figure 62. Figure 61 shows the magnitude displacement response due to a sine wave force input acting over the 30 to 800 Hz frequency range for the rotor spinning at 1000 rpm. Figure 62 completes the Bode plot pair, illustrating the phase difference between the external excitation and output signal over the same frequency range and at the same operating speed. The results indicate that the model is very accurate through the first two natural frequencies. Conversely, the first anti-resonance is inaccurately located. As a consequence, the magnitudes between the first two natural frequencies hold the correct height, but are shifted to higher frequencies in the model. Additionally, the 180 degree phase shift due to the anti-resonance lags in the model.

Overall, the model is sufficient to use in the damage identification procedure through the 30 to 600 Hz range. The discrepancy in the lower magnitude behavior at the first anti-

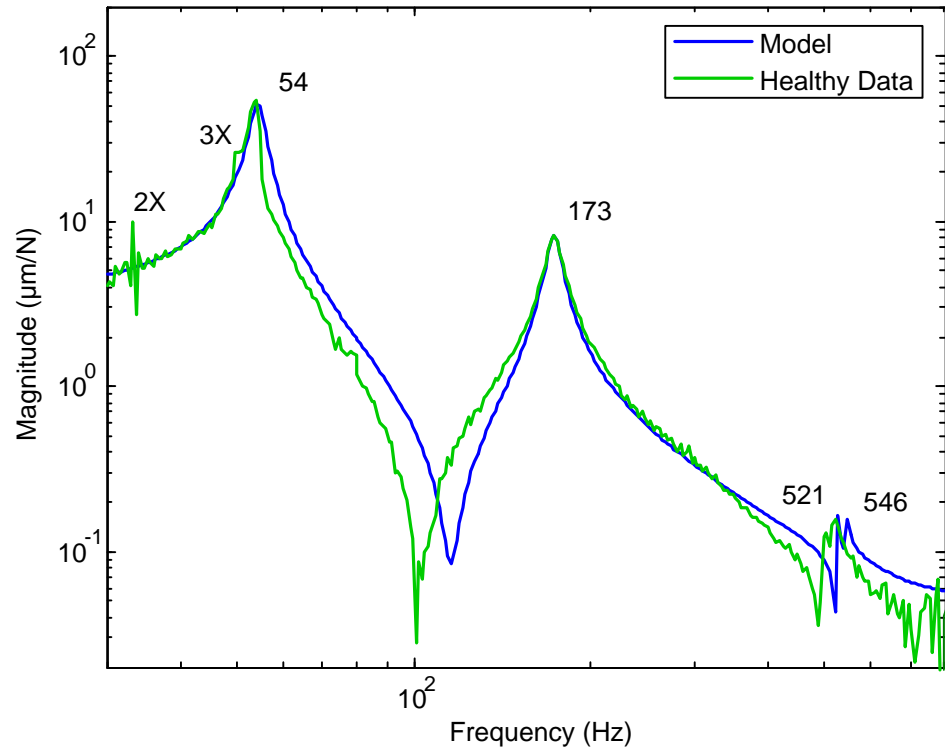


Figure 61 Magnitude Response of the Nominal Model Compared to the Healthy Data at 1000 rpm

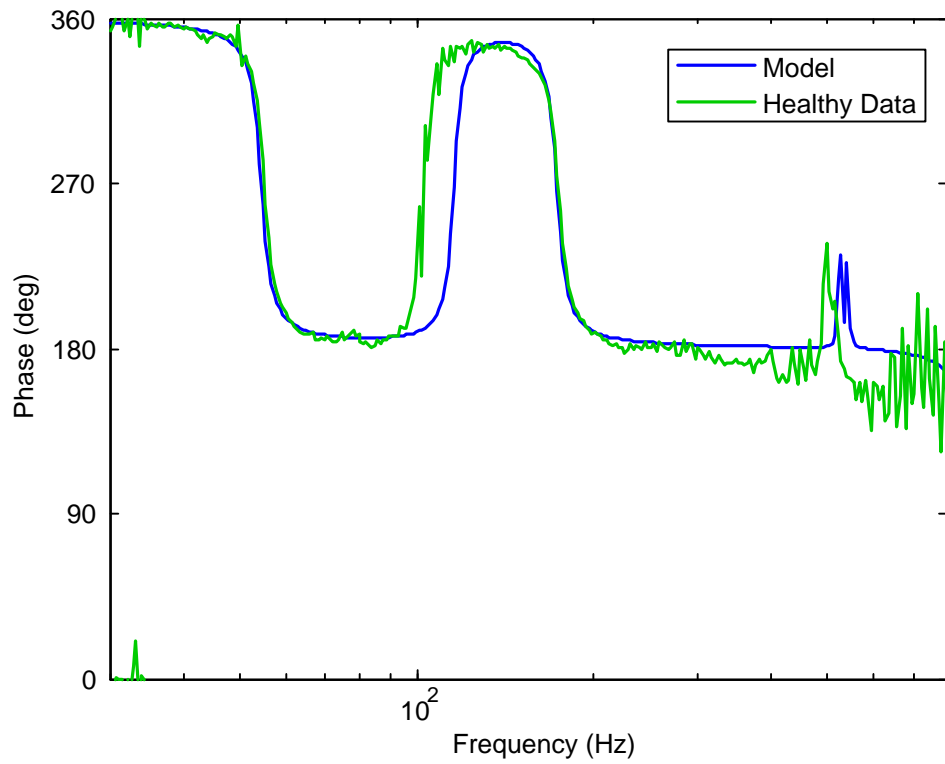


Figure 62 Phase Response of the Nominal Model Compared to the Healthy Data at 1000 rpm

resonance will be covered by the uncertainty, and should not have a large effect on the identified damage dynamics as shown in the previous experiment.

5.5 Damage Identification Problem Description

In the following sections, the damage identification procedure will be applied to a breathing crack in a rotor-bearing system. This will be completed first in simulation and then experimentally, with the aim of using the simulation to verify that the experimental results are within reason. The procedure will be completed through the steps outlined in Section 3.3: 1. Create the nominal healthy model. 2. Fit the noise to the data. 3. Bound the uncertainty to enclose the healthy data. 4. Detect the presence of damage. 5. Identify the local damage dynamics.

The model layout is illustrated in Figure 63. As indicated, the model is composed of nine finite elements, with bearing supports at nodes two and nine, and lumped masses for the disc and AMB rotor occurring at nodes three and seven, respectively. The external input is applied at node eight while the output is located at node 6. Finally, the damage is located in the fourth element, between nodes four and five.

The model validation schematic, which will be used for bounding the uncertainty on the healthy model as well as detecting the presence of damage, is illustrated in Figure 64. Both the external input and output locations are consistent with the rotor-bearing model. An additive uncertainty is applied to the same input and output locations for reasons which will be discussed later. The true system varies between the damage identification steps, with the healthy data being utilized during the uncertainty bounding step and the damaged data being utilized during the damage detection step.

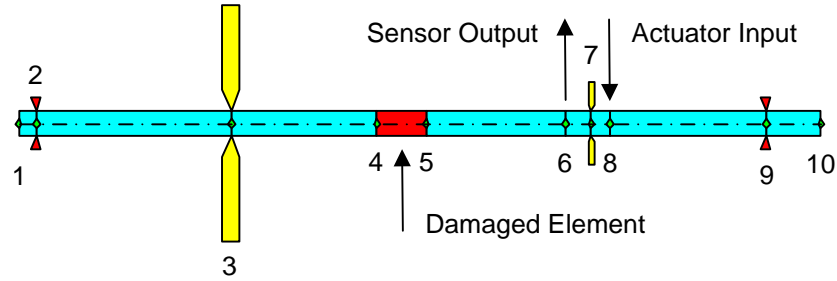


Figure 63 Rotor-Bearing Model Layout

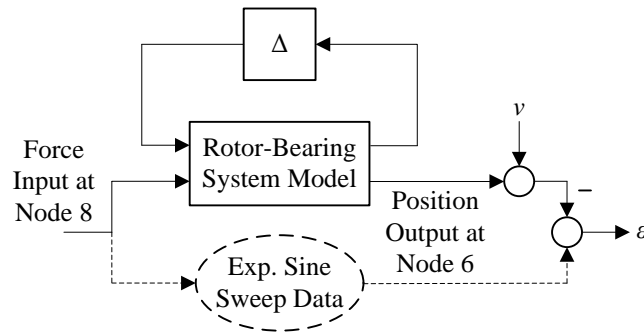


Figure 64 Model Validation Schematic for the Rotating Crack Example

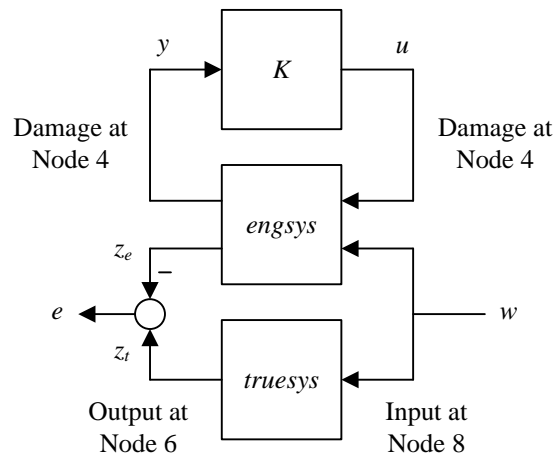


Figure 65 Model-Based Identification Schematic for the Rotating Crack Example

Finally, the model-based identification schematic, used for identifying the local change in dynamics due to the presence of the damage, is illustrated in Figure 65. For this example, the sine sweep data from the damaged system is the *truesys*, while the uncertain healthy rotor-bearing model is the *engsys*. The known difference in dynamics K is the

effect of the rotating EDM cut. The excitation input and sensor output are applied at nodes eight and six, respectively, to remain consistent with the model and experiment. Likewise, the damage input and output are applied at the fourth node; the first node of the damaged element. As a result, the local effect of the damage will be identified.

5.6 Simulation Results

The simulation results for the identification of a breathing crack are generated using the nominal healthy model, healthy data, and the simulated damaged data. The healthy model and healthy data were presented in Section 5.4, whereas the simulated damaged data is generated using the modeling presented in Section 5.2. This simulation is completed in order to obtain a reasonable estimate for the identified change in dynamics due to the breathing crack, which will confirm the accuracy of the experimental procedure.

Following the damage identification procedure detailed in Section 3.3, creating the nominal model is the first step. This was completed in Section 5.4, resulting in a model accurate enough to reliably identify damage in the 30 to 600 Hz frequency range. Next, the noise bound is fit by manually tuning the noise bound to match the noise floor of the healthy data. The result is a bound of 0.02 μm . Similar to the results in the previous chapter, this noise floor is lower than anticipated due to the sine sweep procedure. During the sine sweep averaging was implemented to reduce the influence of noise on the data. In particular, 64 periods of data are taken at each excitation frequency and averaged to obtain the magnitude and phase responses. Interestingly, the identified noise bound is the same for the non-rotating and rotating experiments. While more noise can be expected in

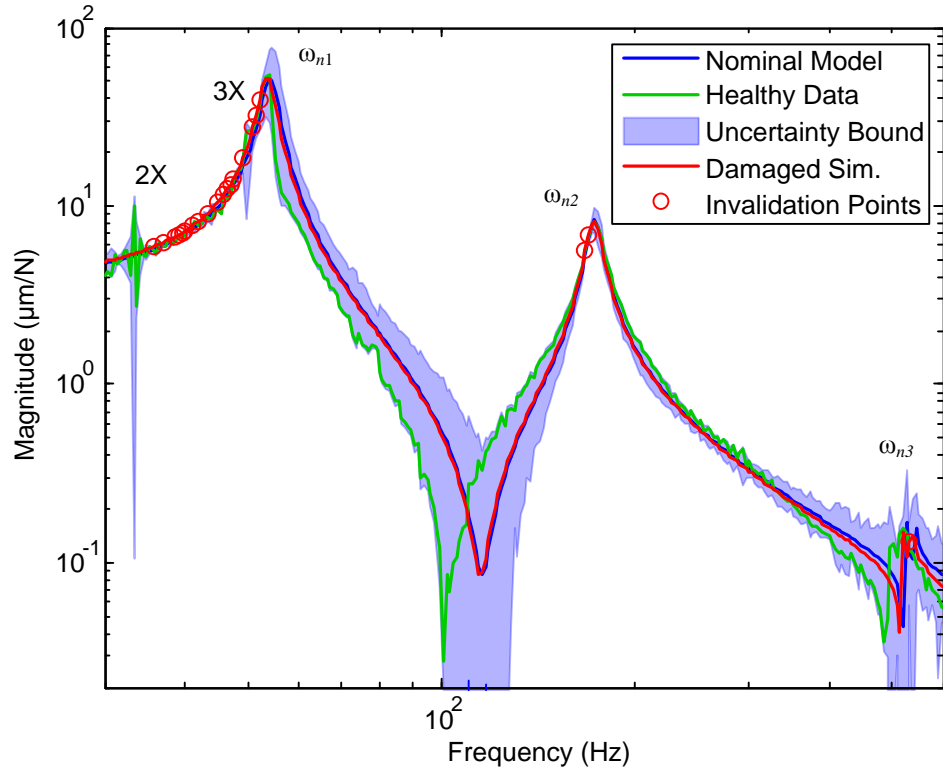


Figure 66 Simulated Rotating Crack Damage Model Validation Results (Magnitude)

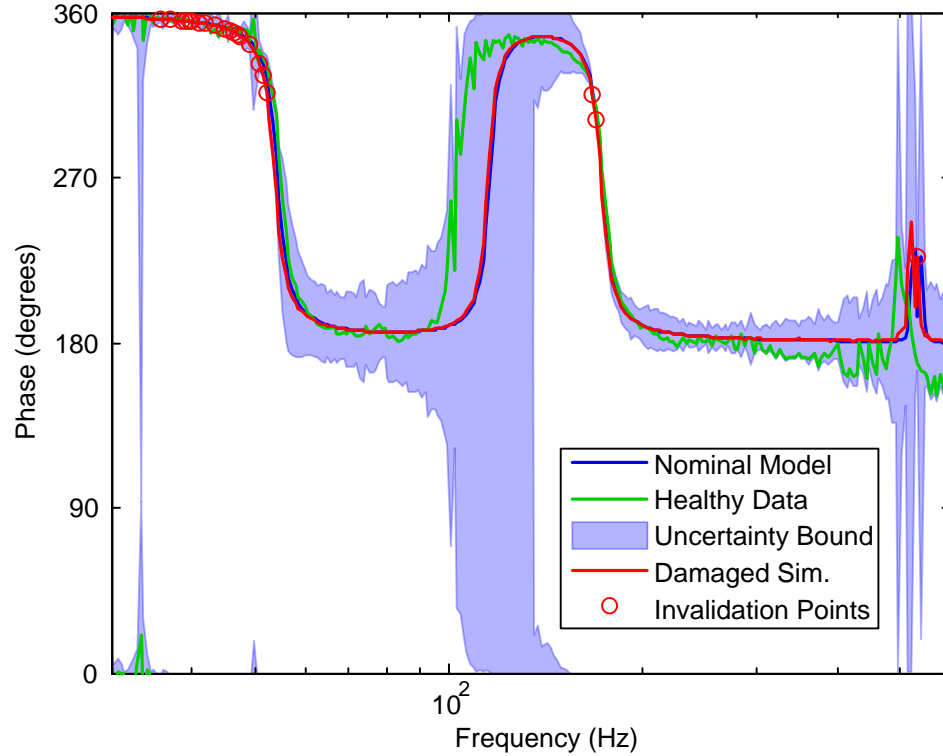


Figure 67 Simulated Rotating Crack Damage Model Validation Results (Phase)

the rotating trial, this effect is mitigated by increasing the excitation current, increasing the signal to noise ratio.

Next, the uncertainty bound is fit to the nominal model in order to enclose all of the healthy data points. Figure 66 and Figure 67 illustrate the results from the model validation procedure. Figure 66 shows the magnitude response, or the displacement response due to an input force, over the 30 to 600 Hz frequency range. Figure 67 shows the phase response, or the angle between the excitation and recorded output, over the same frequency range. The results of this step are indicated by the nominal model, healthy data responses, and the uncertainty bound. As shown, the uncertainty bound is sized to enclose the healthy data at each of the frequency points.

Overall, the size of the bound indicates that the healthy model is reasonably accurate. Three outliers include: the behavior at 33.3 Hz, the height of the bound at the first natural frequency, and the size of the bound in the vicinity of the first anti-resonance. First, the behavior at 33.3 Hz is to be due to the influence of the rotation, as it is two times the running speed of $16 \frac{2}{3}$ Hz (1000 rpm). This nonlinearity is not included in the model and is likely due to misalignment between the bearing center points. Interestingly, the lower bound of the uncertainty approaches zero at the peak, which leads to the phase bound covering the entire 360 degrees of the complex plane. Second, the peak of the uncertainty bound at the first natural frequency is larger than expected. This appears to be the result of the healthy data decreasing abruptly just after the first natural frequency. Third, the inaccuracy of the first anti-resonance creates a large uncertainty bound in the magnitude plot, which also approaches zero. As a result, the phase response in the region once again covers the entire phase range. Fortunately, the log scale on the magnitude graph

overemphasizes the effect of a large lower bound on the uncertainty, which does not lead to large inaccuracies in the identified damage dynamics, as will be shown later. Conversely, the larger magnitude of the healthy data in this region will lead to larger uncertainties in the identified damage.

Once the uncertainty bound is optimized to create the uncertain healthy system, the second data set may be analyzed in order to detect the presence of damage. Figure 66 and 66 illustrate the results of this step. In these figures, the damaged data indicates the results from the system identification of the simulated breathing crack while the fault points indicate the frequencies where the damaged data falls outside of the uncertainty bound. The results detect the presence of damage in the frequencies leading up to the first natural frequency peak, and at two points in the vicinity of the second peak.

This result indicates two important facts. First, the breathing crack is difficult to detect, even in simulation. As shown, the behavior of the damaged data is difficult to distinguish from the nominal model by visual inspection. This result supports what is known about the behavior of breathing cracks, which creates a small change in the dynamics overall. As a result, the damaged response does not largely deviate from the healthy model. Second, the uncertainty bound in some areas is large relative to the difference between the healthy and damaged models. Naturally, no fault points are indicated in areas with a large uncertainty bound.

For more detail, a closer view of the magnitude response from 30 to 60 Hz is shown in Figure 68. This plot shows the frequency range where the damage is indicated. The cause of which is twofold. First, in this region, the simulated crack causes the largest reduction in stiffness. Second, the nominal model is very accurate in this region. Any differences

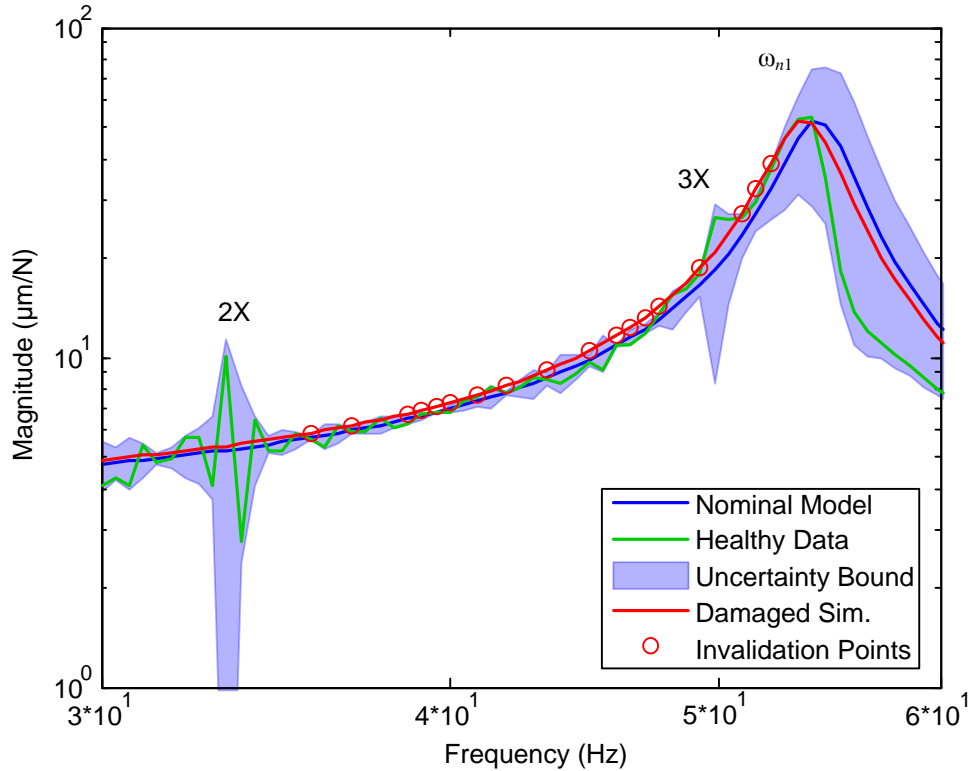


Figure 68 Simulated Rotating Crack Damage Model Validation Results Detail

between the model and healthy data appear may be attributed to the noise in the experimental procedure, which have a relatively small effect at this magnitude. Two exceptions occur at the 2X and 3X running speed components which cause nonlinearities in the system that are not present in the model. As a result, no damage points are indicated around these two frequencies.

The final issue with the simulation trial is that the damaged data is affected by the crack relative to the healthy model. Clearly, this is due to the damaged data being generated in a simulation that utilizes the healthy model. This becomes a problem in regions where the healthy model is less accurate when compared to the experimental data, which are already indicated by a large uncertainty bound. In these areas, the healthy model sits in the center of the uncertainty bound. Therefore, a large change from the healthy model is required to cross over the uncertainty bound and indicate damage.

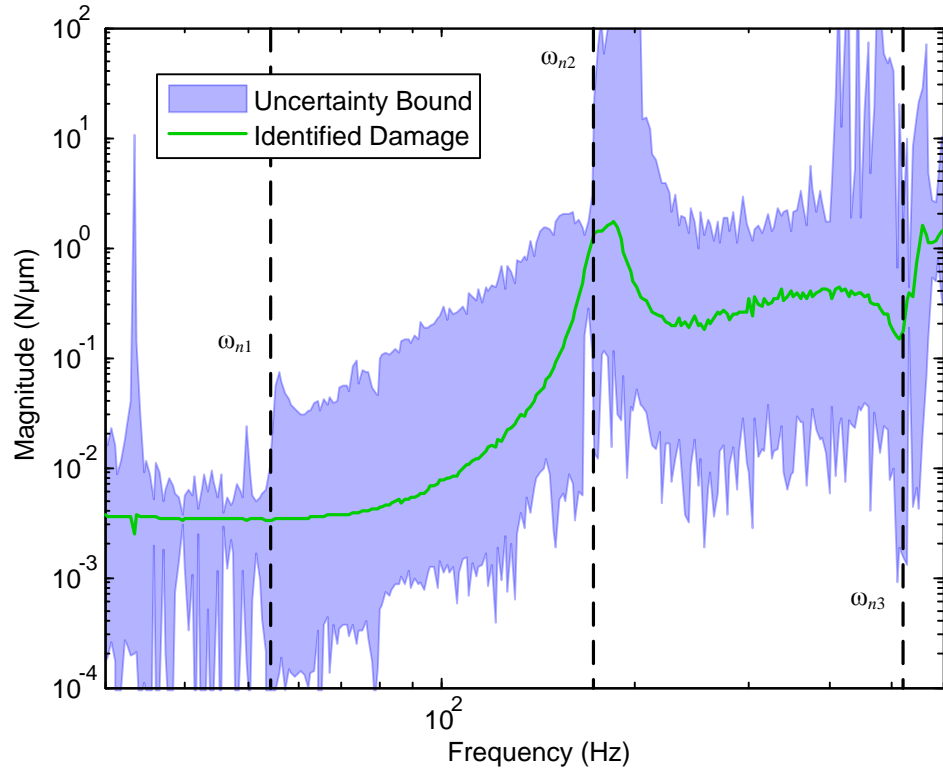


Figure 69 Simulated Rotating Crack Identified Damage Dynamics (Magnitude)

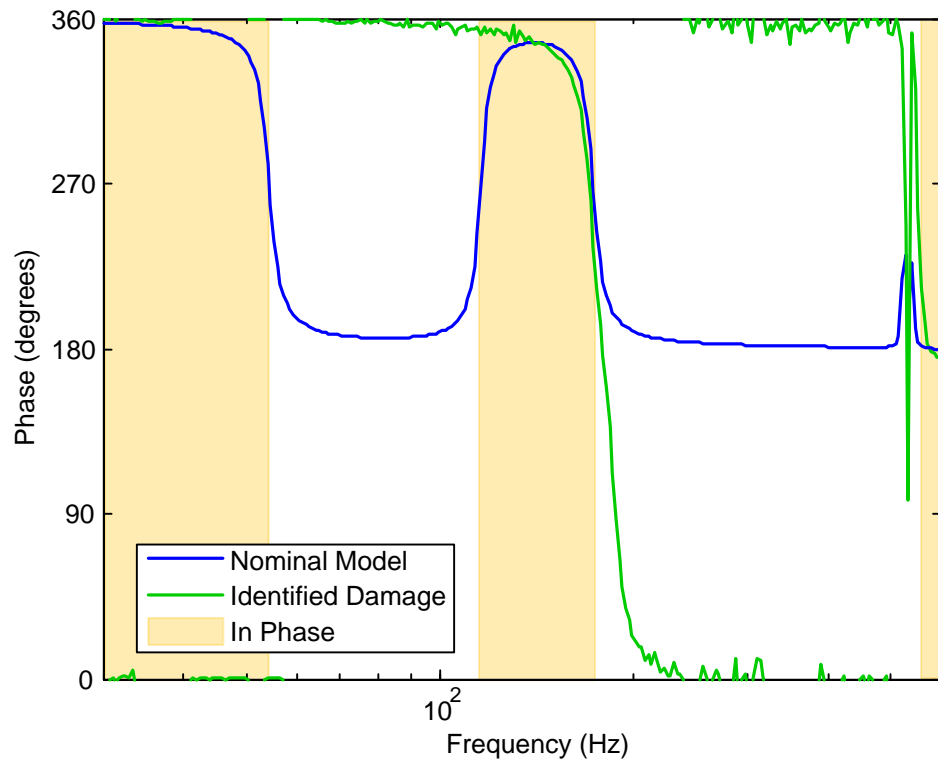


Figure 70 Simulated Rotating Crack Identified Damage Dynamics (Phase)

Alternatively, the healthy data lies on the edge of the uncertainty bound, meaning that a smaller change from the healthy data is required to detect damage. In the experimental case, the damaged data will be relative to the healthy data, alleviating this issue for when the damage causes the data to move from away from the nominal model.

Now that the presence of damage has been detected, the local change in dynamics due to the rotating EDM cut can be identified. Figure 69 summarizes the damage dynamics due to the breathing crack. The plot shows the force magnitude response due to a displacement input over the identification frequency range of 30 to 600 Hz. The magnitude response offers some interesting insight into the behavior of the simulated breathing crack. First, the crack behaves like a flat reduction in stiffness below 80 Hz. This is the same behavior as a change in spring stiffness. As the frequency increases, the crack takes on a gradual upslope. The behavior changes again at the second natural frequency ω_{n2} . A local peak in the damaged response occurs. Interestingly, no such behavior is shown at the first natural frequency ω_{n1} . Similarly, the third ω_{n3} provides a peak in the identified dynamics along with a valley resembling an anti-resonance. Finally, the uncertainty bound offers a wide range of possible behaviors for the actual damage. This is due to the healthy uncertainty bound from the model validation step being larger than the difference between the healthy and damaged responses at most frequencies.

The frequency-dependent phase responses of the identified damage and nominal model are plotted in Figure 70. The relative angle between the nominal model and identified damage determines whether the two are in phase or out of phase. As a consequence, the in phase region will cause a reduction in stiffness in the model, whereas the out of phase region will cause an increase in stiffness. The two responses begin with

an in phase region until the first natural frequency of the nominal model. The responses remain out of phase until the first anti-resonance of the model before falling out of phase at the second natural frequency. A large out of phase frequency range occurs before the third natural frequency's peak and anti-resonance pair, which settles the two back in phase. This phase behavior is consistent with the magnitude plot in Figure 46. Specifically, the in phase regions correspond to frequencies where the simulated damage response has a higher compliance, i.e. lower stiffness, magnitude than the nominal model. Conversely, the out of phase regions correspond to the frequencies where the simulated damage response is lower than the nominal model, indicating a higher stiffness in the damaged simulation at those frequencies.

5.7 Experimental Results

The experimental damage identification results are obtained using the healthy data set along with the nominal healthy model and an experimental damaged data set. Both the healthy data set and nominal healthy model were presented in Section 5.4. This experiment is completed in order to identify the effect of a breathing crack on a rotor, demonstrating the identification technique on a useful example which is known to be difficult to detect.

Once again, the damage identification technique presented in Section 3.3 outlines the procedure which will be followed here. First, the nominal model is developed, which was completed in Section 5.4. As stated earlier, the model is accurate for detection for the 30 to 600 Hz range. The only significant error in the model is in the incorrect location of the first anti-resonance. This effect will be investigated later in the section. Second, the noise is fit to the model. Similar to the simulation results, the noise bound is fit to match the

noise floor observed in the healthy data. Therefore, the value of $0.02 \mu\text{m}$ is used again as the healthy data is the same.

Third, the uncertainty is bound is created to allow the uncertain healthy system to include all of the observed data. Figures 71 and 72 present the results from this step with the responses for the nominal model, healthy data, and uncertainty bound. Figure 71 shows the frequency-dependent compliance, or the displacement response due to a force input. Figure 72 shows the angle between the input signal and output response. The plots indicate that the model validation process was completed correctly as the healthy data is contained within the uncertainty bound throughout.

Similar to the simulation, the uncertainty bound is generated using the healthy data and nominal model covered in Section 5.4. As a result the same bound is created. Any differences in the plot are purely graphical. Naturally, this leads to the same conclusions as in the simulation which are summarized here. First, the bound is tight overall, meaning that the model is accurate and small changes in the system dynamics will be detected. Next, three frequency ranges produce larger bounds: the area around 33 Hz, or two times the running speed, the first natural frequency, and the frequencies around the anti-resonance. Details on the behavior in these regions were covered in the previous section.

Fourth, the damaged data set is compared to the uncertain healthy system in order to detect any change in dynamics which may be indicative of damage. The results of this step are also summarized by Figures 71 and 72. As shown, the technique identifies enough fault points to clearly indicate the presence of damage.

The damage detection step leads to significantly different results from those predicted by the simulation. First of all, the damage is detected at many more frequency points,

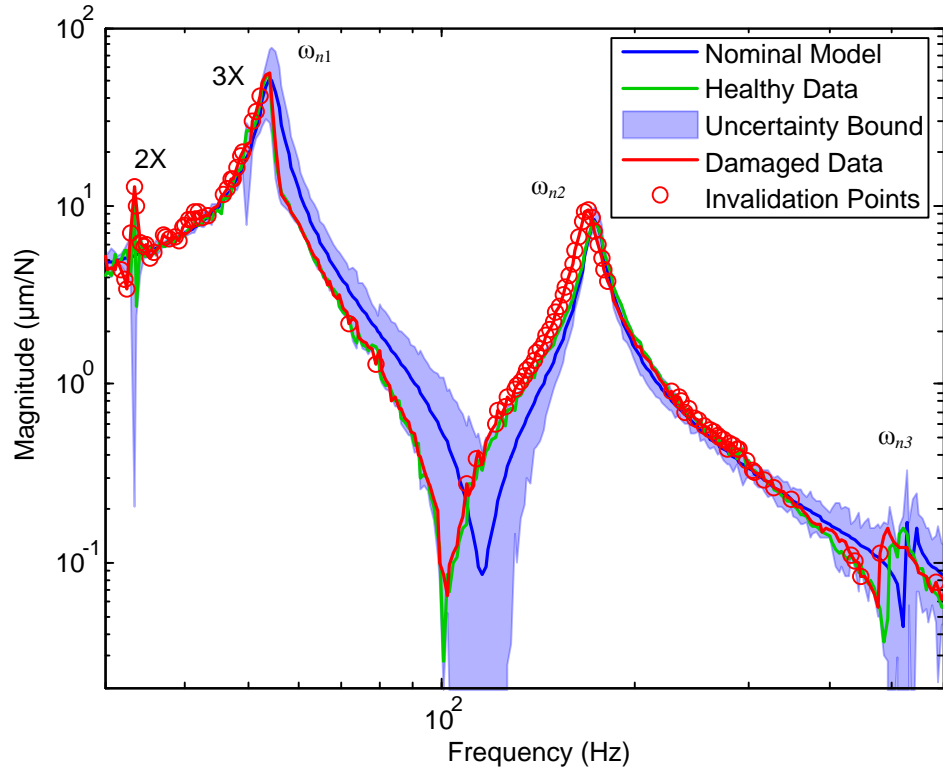


Figure 71 Experimental Rotating Crack Damage Model Validation Results (Magnitude)

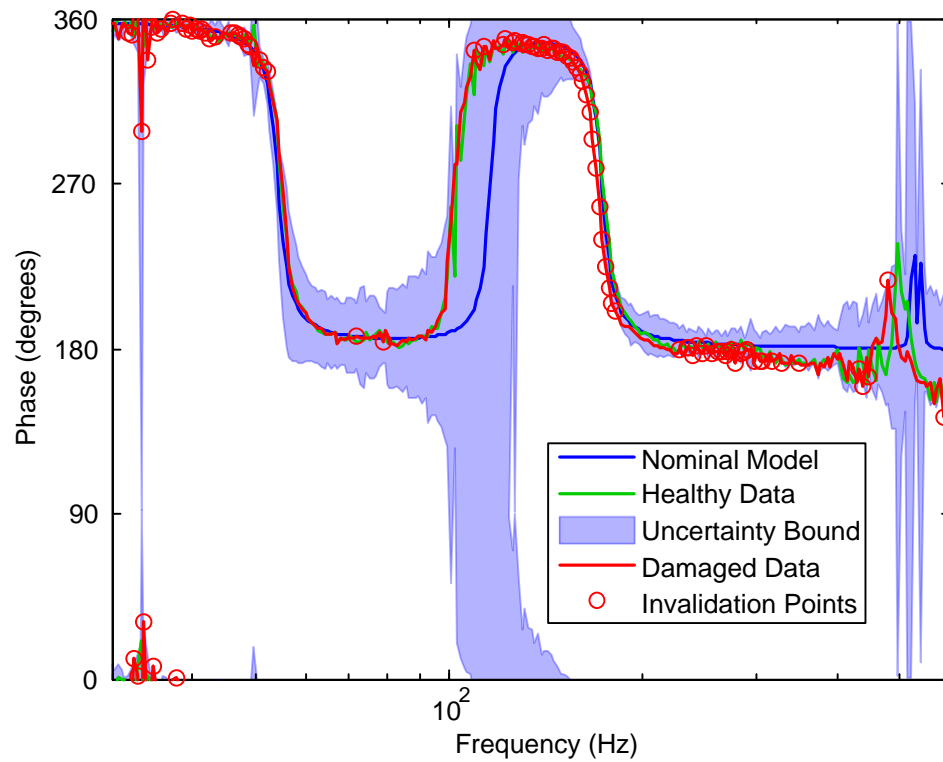


Figure 72 Experimental Rotating Crack Damage Model Validation Results (Phase)

with the experimental damage falling out of the bound at 101 out of 262 points or 38.6%, while the simulation damage falls out at 21 of 262 points or 8%. As alluded to earlier, the primary reason for this is that the simulation damaged data is generated relative to the nominal model, whereas the experimental damaged data is damaged relative to the healthy data. As a result, the reduction in stiffness moves the simulated damage response to the left of the nominal model. Similarly, the reduction in stiffness moves the damaged data to the left of the healthy data. The reason why this causes more fault points to be detected goes back to the creation of the uncertainty bound in the third step of the identification process. For both trials, the uncertainty bound is optimized to enclose the healthy data with the least distance from the nominal model in the complex plane. As a result, the healthy data rests on the border of the bound. Clearly, small changes from the healthy data in the direction of the border could result in a point falling outside of the bound. More details on this behavior are covered in the previous chapter along with an illustration on the bound of an individual frequency point in Figure 48.

For a more detailed view of this issue, Figure 73 shows a close up of the magnitude response in the region of 120 to 180 Hz. This frequency range covers the magnitudes leading up to and including the second natural frequency. It can be seen that the experimental damaged data very clearly falls outside of the healthy model uncertainty bound, resulting in the points being marked as indicative of a fault. In contrast, the simulated damaged data remains firmly within the bound and does not cause any of the frequencies to be marked as points of interest. While the simulated damaged data does deviate from the healthy model, inaccuracies in the modeling cause this data to appear to be stiffer than the healthy data over the frequency range shown, a counterintuitive change

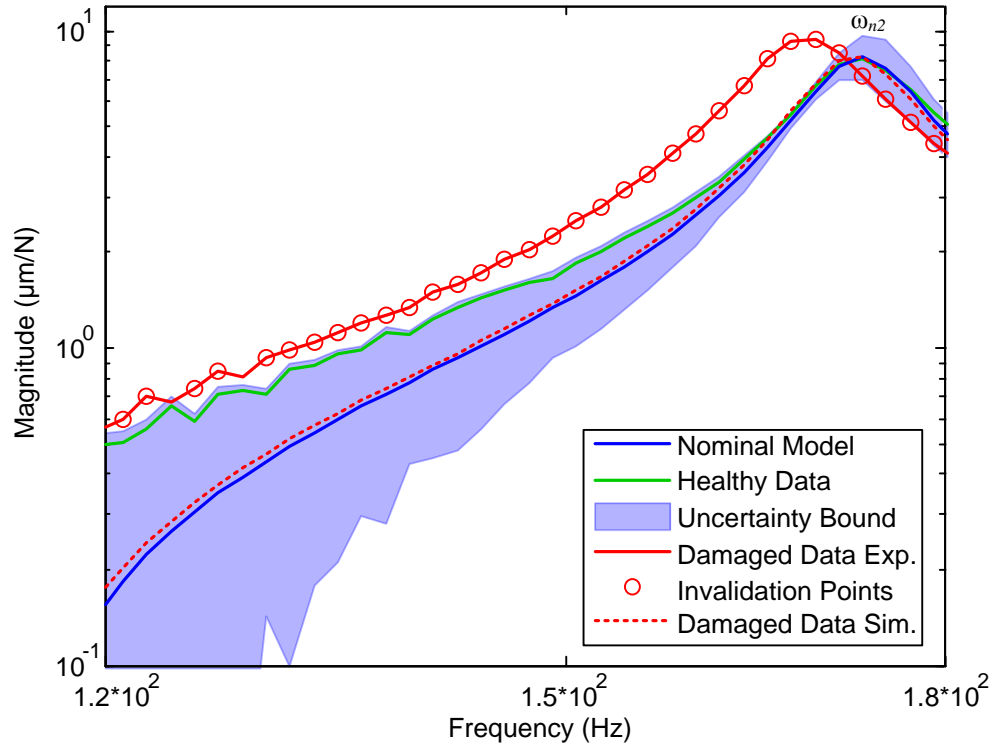


Figure 73 Experimental Rotating Crack Damage Model Validation Results Detail

for a crack in a shaft to induce. Therefore, despite the fact that both the simulated and experimental damaged data sets show a decrease in stiffness relative to their starting points, only the experimental set indicates damage because this change is relative to the healthy data set.

The second cause for more detection points is the nonlinear behavior occurring at two times the running speed. Figure 74 provides a closer view of the magnitude response in the frequencies leading up to the first critical speed. This plot illustrates how the nonlinearity in the healthy data at 2X is reflected in the damaged data. In turn, this allows for damage to be detected at the points in the vicinity despite the effect not being included in the nominal model. A breathing crack is an additional nonlinearity which allows for more cross talk between the unbalance and harmonics of the running speed

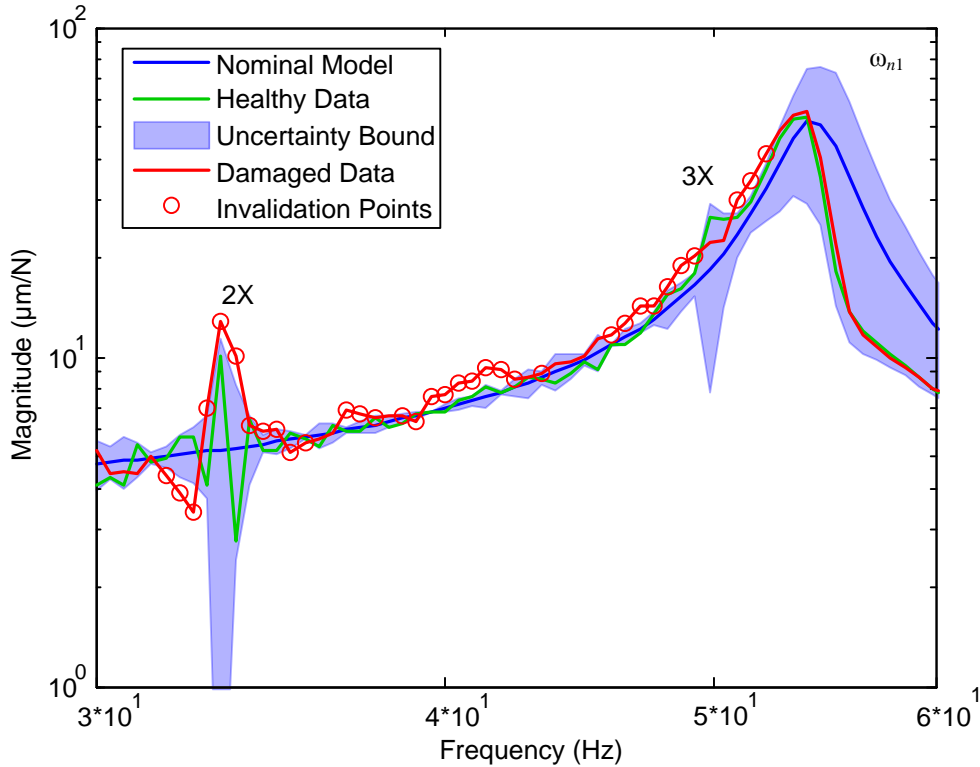


Figure 74 Experimental Rotating Crack Damage Model Validation Results Detail 2

than exists in the healthy system. Therefore, more points can be invalidated even in the presence of the increased uncertainty bound.

Finally, following successful detection of a change in dynamics, the damage which caused this change is identified. The results for this step are presented in Figure 75. The figure shows the magnitude of the force response due to a displacement input over a 30 to 600 Hz frequency range. Interestingly, the identified damage exhibits unique behaviors between each natural frequency. Prior to the first natural frequency, there is a region which appears erratic. Clearly, the nonlinearities shown in Figure 74 persist into the identified damage dynamics. Interestingly, this does not lead to a large uncertainty bound in the region. Between the first and second natural frequencies, the damage follows a steady upward trend indicative of a change in both stiffness and inertia. Lastly, the region between the second and third natural frequencies shows a more level magnitude with the

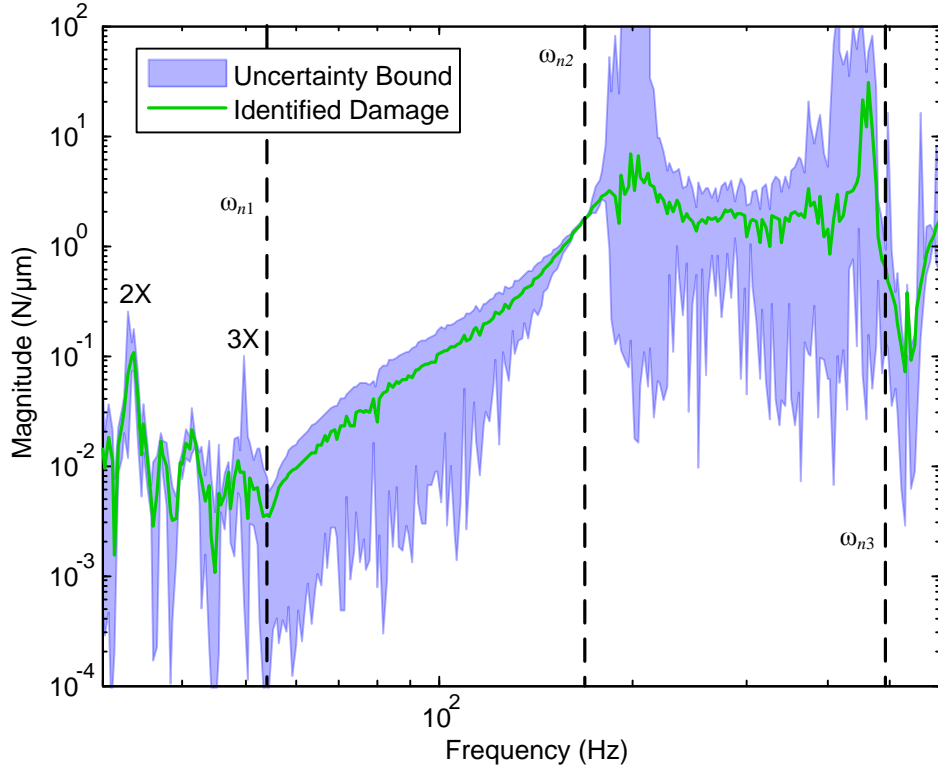


Figure 75 Experimental Rotating Crack Identified Damage Dynamics (Magnitude)

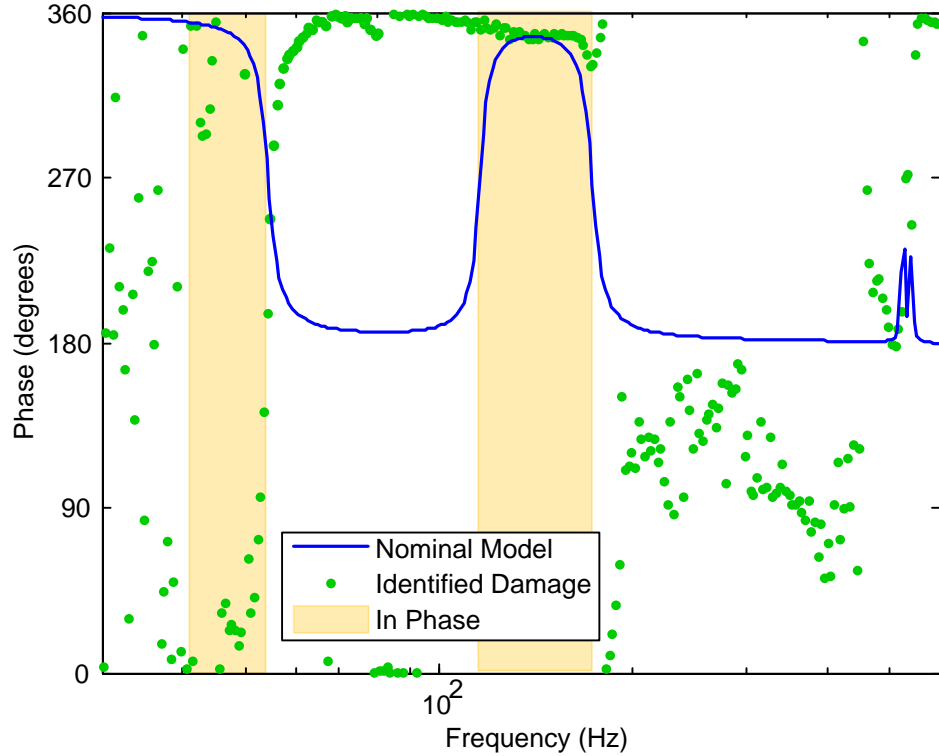


Figure 76 Experimental Rotating Crack Identified Damage Dynamics (Phase)

exception of a single large peak. This peak occurs around the anti-resonance of the damaged data and is due to the difference between the model and data around this frequency. The final region, after the third peak, shows a dip in the damage magnitude due to the closeness of the model and data before trending upward once again.

Additional information on the identified damage dynamics are provided by the phase response shown in Figure 76, which illustrates the phase of the identified damage and nominal model relative to their inputs over the indicated frequency range. Once again, the relative phase of the nominal model and identified damage responses provides insight into whether the damage will induce a decrease or increase of stiffness in the nominal model. Recall that the in phase region indicates a decrease in stiffness, whereas the out of phase region indicates an increase in stiffness.

This phase plot follows a few similar trends to the simulation. First, there is an in phase region before the model's first natural frequency. Second, a second in phase region occurs between the model's first anti-resonance and second natural frequencies. Where the experiment deviates significantly is in three frequency ranges. The first is in the frequencies before the first in phase region. This range would be expected to be in phase, but cannot be labeled as such due to the noise in the data brought on by the nonlinearity in the damaged data. The second is region after the second natural frequency. According to the magnitude plot, the two responses should be in phase, due to the damaged data showing a decrease in stiffness relative to the nominal model through roughly 300 Hz. Unfortunately, the jagged nature of the identified damage response does not allow it to settle in phase at 180 degrees. The third discrepancy occurs after the third natural

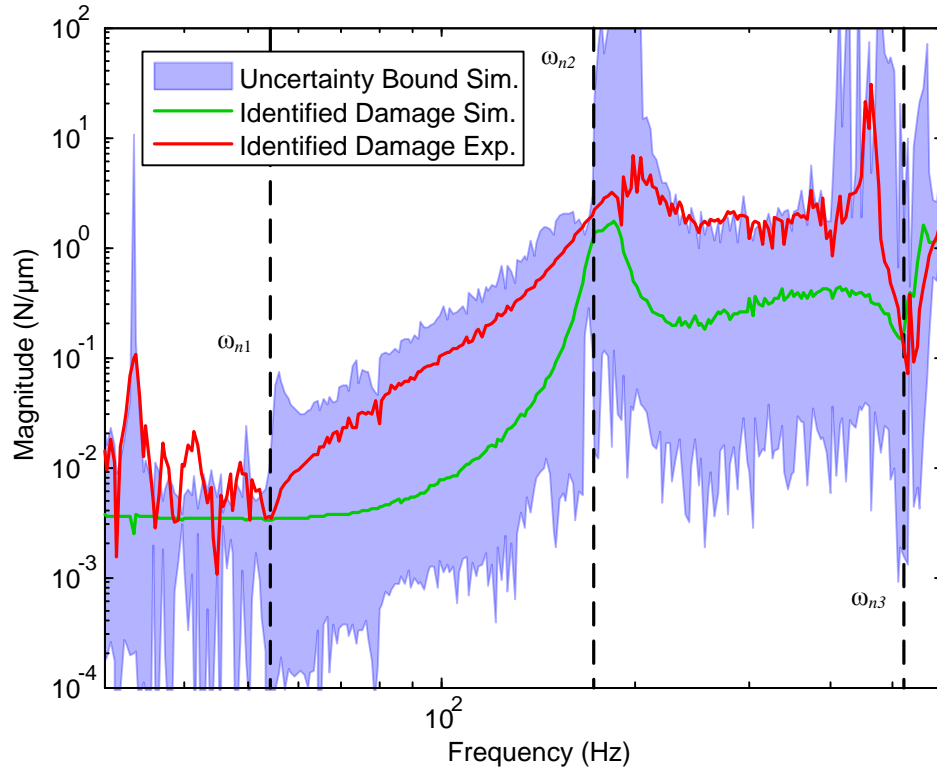


Figure 77 Simulated and Experimental Identified Damage Comparison

frequency, where the simulated identified damage falls back in phase with the nominal model, whereas the experimental identified damage does not.

The final piece of analysis is provided by comparing the simulated and experimentally identified dynamics of the breathing crack. First, recall the results from Section 3.4 Illustrative Example of Damage Identification. The example illustrates the damage identification procedure on a three degree of freedom mass-spring-damper system. Additionally, multiple trials provide insight into the effect of modeling inaccuracies. Figure 30 summarizes this effect, illustrating that the identified damage dynamics and associated uncertainty bound for the more accurate models are nested within the uncertainty bound for the less accurate model(s). Now, the simulated and experimentally identified dynamics are compared to see if any correlation can be found.

In Figure 77, the identified experimental and simulated damages, originally presented in Figures 69 and 75, respectively, are plotted along with the uncertainty bound from the simulation results from Figure 69. A few interesting conclusions can be drawn from the comparison of the two identified responses. First, the magnitudes are roughly equivalent at the first and third natural frequencies. In contrast, the simulated damage underpredicts the change in stiffness at the second natural frequency. Another difference is in the presence of nonlinearities in the low frequency behavior due to the crack interacting with the running speeds. Next, the shape of the slope is different between the first and second natural frequencies. This difference is due to both the disagreement between the second natural frequency as well as the misplacement of the first anti-resonance. Finally, the peak in the experimental damage which precedes the third natural frequency is missing from the simulation, due to the simulated damaged third natural frequency more closely matching that of the nominal model.

Interestingly, the experimental damaged data is mostly enclosed by the simulated uncertainty bound, aside from the low frequency region. Superficially, this appears to be analogous to the results from Figure 30, where the more accurate models sit inside the uncertainty bounds of their less accurate counterparts. Though this is not a completely apt comparison, it reinforces the conclusions previously drawn from Figure 73. The identified experimental damage is able to have smaller uncertainty bounds than the simulation due to the fact that the experimental damage occurs relative to the healthy data, which drives the size of the uncertainty bound. As a result, the damaged behavior naturally occurs near the edge of the uncertainty bound. On the contrary, when the simulation damage appears to be closer to the nominal model than the healthy data, such

as between the first and second natural frequencies, the associated uncertainty bound becomes very large. This leads to the conclusion that this damage identification procedure is more accurate, and therefore, applicable, in actual experiments. Though the simulation does offer a valuable reference point which confirms that the identified damage is reasonable.

5.6 Conclusions

This experiment demonstrated that the proposed damage identification method is capable of detecting and identifying the change in dynamics brought on by a breathing crack in a rotor. This case study is important because the breathing crack is known to present difficulties in detection due to the small change in system dynamics which is induced. Despite this fact, the method was able to fulfill the goal of identifying the change in dynamics along with an uncertainty bound, which provides a frequency-dependent quality estimate for the results. Additionally, this bound may be used in future robust control applications; for example, designing a controller which is robust to the presence of cracks.

Interestingly, the technique was shown to be more effective with experimental data than in simulation. This accuracy is demonstrated by the experimental results indicating damage at more frequency points as well as producing a smaller uncertainty bound on the experimentally identified damage. While this result is somewhat counterintuitive, it follows the fact that the healthy data is consistently utilized for the uncertainty bound on the nominal model. This result can be seen as a success since the technique is designed for experimental use. Additionally, the simulated results are still able to provide a valuable confirmation that the identified damage falls within a realistic range.

CHAPTER VI

CONCLUSIONS

This chapter will cover the primary contributions of this work as well as possible directions for continuing the study of robust damage identification. First, the contributions from developing a damage identification method utilizing robust control tools will be discussed. To that end, the developed technique as well as detail the advantages of performing a damage identification procedure in the robust control framework will be covered. Next, three directions for future work will be introduced.

6.1 Contributions

The primary contribution of this work is the development of a new damage identification technique which utilizes robust control tools. In summary, the technique first applies model validation to detect a change in dynamics indicative of damage, followed by the application of model-based identification to define the change in dynamics due to the damage. The detailed procedure is laid out by the following five steps.

Step 1 Develop the nominal model. This may be completed using an established engineering technique, such as finite element modeling.

Step 2 Fit the noise to the model. The noise is defined by a deterministic bound on the external disturbances. For this work, the bound was found by matching the noise magnitude to the noise floor of system identification data in the frequency domain.

Step 3 Bound the uncertainty of the nominal model using the frequency-dependent model validation optimization problem FDMVOP. By employing the frequency-dependent model validation decision problem FDMVDP illustrated in Figure 13 at every frequency point of interest, the system identification input and output of the healthy system and the nominal model are utilized to calculate the optimal uncertainty bound. As a result, the FDMVOP will experimentally not invalidate the uncertain healthy system. In other words, any difference between the nominal model and the healthy physical system will be accounted for by the definitions for the noise and uncertainties. Therefore, the uncertain system may be used to robustly predict any future behavior of the healthy physical system.

Step 4 Collect new system identification data from a system suspected of being damaged. Check the new data against the healthy uncertain model for changes in behavior indicative of damage. This is accomplished by the frequency domain inverse model validation decision problem FDMVDP. This is the inverse of the FDMVDP. The difference between these two problems is that instead of attempting to identify the uncertainty bound required to enclose the data, the experimentally not invalidated uncertainty bound from the previous step will be compared to the new data to check if any points fall outside of the bound. As a result, the FDMVDP indicates frequency

points at which the uncertainty bounds are not large enough to enclose the experimental data. Therefore, there exists a difference between the data and nominal model which is not explained by the uncertainties and noise, indicating a change in the system's dynamics between the trials. For this procedure, such a change is assumed to be indicative of damage.

Step 5 Identify the change in dynamics due to the damage. This step follows the model-based identification procedure illustrated in Figure 15. In particular, this step compares the healthy engineering model and the data from the damaged system as the engineering *engsys* and true systems *true_sys*, respectively. What results is the change in dynamics due to the damage D_u . Additionally, the engineering system is able to inherit the uncertainty and noise from the model validation procedure. This leads to the definition for the damage containing an uncertainty bound, which can be utilized as a quality measure for the identified dynamics.

The novelty in this damage identification technique results from the combination of two methodologies which were developed in the robust control framework. Application of a robust control relevant model validation technique along with model-based identification, which was defined to be solved with robust control tools (uncertainties and μ), leads to a damage identification technique which remains in the robust control framework. The advantages to this are three-fold. First, the damage identification technique may be completed using the same set of tools. Also, the uncertainty definitions from the model validation step may be carried over into the model-based identification procedure for identifying the local change in dynamics due to the damage. As stated previously, this allows a definition of the damage which also contains uncertainties. This

leads directly into the second and third advantages. Second, the uncertainty bound on the identified damage may be used as a quality estimate for the identified change in dynamics due to the damage. Third, the estimate for the damage dynamics may be ported into robust control applications. The importance of this feature will be covered in the future work section.

Finally, the method was successfully implemented in the detection of the change in dynamics due to a breathing crack in a rotor. This result is important because the crack represents a damage source which is difficult to detect in practice. In fact, previous work on the subject required inputs defined specifically for the experimental setups to accurately detect the presence of the crack. In contrast, the presented methodology was shown to detect the presence of a crack using the commonly-used system identification technique in the sine sweep. Also, the dynamics of the local effect of the crack may prove to be valuable moving forward in the field of structural health monitoring in rotors.

6.2 Future Work

The future work directions for this topic can be broken up into three areas. First is continuing the work into robust controls. Second, is continuing into the area of model-based identification and creating model sets for common sources of damage. Third, is refining the damage identification technique to include more detailed descriptions of the damage in the form of determining the location.

The first area of future work would be to continue the application into robust controls. The basic idea is to utilize the knowledge obtained about the damage to design a robust controller for the damaged system. This could go in one of two directions. The first is to design a controller to be able to control the setup in the presence of the known source of

damage. In other words, create a controller which is robust to the damage dynamics. Demonstration of this technique could be completed by experimental verification of the performance of the healthy and damaged systems and a comparison to the defined performance criteria. The second direction would expand on this idea by utilizing a controller switching technique in order to safely power down the system in the case of detected damage. A simplified look at the procedure would be to detect and identify a source of damage, design a controller for it, switch to the controller and safely power the system down. This application would be useful wherever machines are operated at supercritical speeds by providing a safety guarantee when slowing through the damaged critical speed, which may be different than the healthy critical speed for which the original controller was designed. While this second application is more ambitious because a controller would have to be designed while the machine is operating, both would make use of the definition of the damage dynamics in the robust framework.

The second area of future work would be to continue in the direction of identification of the local change in dynamics due to the damage. In general, the goal of this direction would be to gain insight into the effect of the severity of a particular damage source on the identified damage dynamics. For example, applying the developed method to the same crack detection test rig with varying EDM cut depths could lead to a quantified understanding of the effect of varying the depth of the breathing transverse crack in a rotor. The final goal of this study would be to create a model of the breathing crack which is dependent on the depth, location, rotor speed, etc. of the crack. This would tie in the additional topic of system identification for robust systems. If successful, this work could

provide different models for various damage types, and eventually the ability to classify an unknown source of damage.

The final direction for future work would be to provide more information in the damage identification technique. Particularly, the method would seek to provide the location of the damage. This advancement would allow for increased ease of use, as the engineer would know where repairs to the damaged system need to be made, potentially saving the effort of disassembling and inspecting the entire setup. Work in this area has been attempted by the author, as touched on in the literature review in Section 1.3.2. Currently, the addition of damage location was successful in one trial, but the technique has shown to be influenced by the frequency range of the data used in system identification. More investigation would need to be completed in order to refine the technique and remove these dependency. Potential benefits include requiring less sensors or less frequency data in the form of less natural frequencies being required for location.

REFERENCES

- [1] R. S. Smith, "Model validation for uncertain systems," Diss. California Institute of Technology, Pasadena, CA, 1990.
- [2] R. S. Smith and J. C. Doyle, "Towards a methodology for robust parameter identification," in *American Control Conference, 1990*, San Diego, CA, 1990.
- [3] R. S. Smith and J. C. Doyle, "Model validation: a connection between robust control and identification," *Automatic Control, IEEE Transactions on*, vol. 37, no. 7, pp. 942-952, 1992.
- [4] R. S. Smith, C. C. Chu and J. L. Fanson, "The design of H_∞ controllers for an experimental non-collocated flexible structure problem," *Control Systems Technology, IEEE Transactions on*, vol. 2, no. 2, pp. 101-109, 1994.
- [5] K. Poolla, P. Khargonekar, A. Tikku, J. Krause and K. Nagpal, "A time-domain approach to model validation," *Automatic Control, IEEE Transactions on*, vol. 39, no. 5, pp. 951-959, 1994.
- [6] A. Kumar and G. J. Balas, "An approach to model validation in the μ framework," in *American Control Conference, 1994*, 1994.
- [7] A. Kumar and G. J. Balas, "A scaling approach to model validation in the μ -framework," in *American Control Conference, 1995*, Seattle, Washington, 1995.
- [8] L. Guo and L. Ljung, "The role of model validation for assessing the size of the unmodelled dynamics," in *Proceedings of the 33rd Conference on Decision and Control*, Lake Buena Vista, Florida, 1994.
- [9] R. L. Kosut, "Uncertainty model unfalsification: A system identification paradigm compatible with robust control design," in *Decision and Control, 1995., Proceedings of the 34th IEEE Conference on*, New Orleans, LA, 1995.
- [10] R. S. Smith, "Model validation for robust control: an experimental process control application," *Automatica*, vol. 31, no. 11, pp. 1637-1647, 1995.
- [11] T. Zhou and H. Kimura, "Structure of model uncertainty for a weakly corrupted plant," *Automatic Control, IEEE Transactions on*, vol. 40, no. 4, pp. 639-655, 1995.
- [12] S. Rangan and K. Poolla, "Time-domain validation for sample-data uncertainty models," *Automatic Control, IEEE Transactions on*, vol. 41, no. 7, pp. 980-991, 1996.
- [13] R. Smith and G. E. Dullerud, "Continuous-time control model validation using finite experimental data," *Automatic Control, IEEE Transactions on*, vol. 41, no. 8, pp. 1094-1105, 1996.
- [14] G. Dullerud and R. Smith, "Sampled-data model validation: An algorithm and experimental application," *International Journal of Robust and Nonlinear Control*, vol. 6, no. 9-10, pp. 1065-1078, 1996.
- [15] R. Smith, G. Dullerud, S. Rangan and K. Poolla, "Model validation for dynamically uncertain systems," *Mathematical Modelling of Systems*, vol. 3, no. 1, pp. 43-58, 1997.

- [16] J. Chen and S. Wang, "Validation of linear fractional uncertain models: Solutions via matrix inequalities," *Automatic Control, IEEE Transactions on*, vol. 41, no. 6, pp. 844-849, 1996.
- [17] J. Chen, "Frequency-domain tests for validation of linear fractional uncertain models," *Automatic Control, IEEE Transactions on*, vol. 42, no. 6, pp. 748-760, 1997.
- [18] O. Toker and J. Chen, "Time domain validation of structured uncertainty model sets," in *Decision and Control, 1996., Proceedings of the 35th IEEE Conference on*, 1996.
- [19] B. Boulet and B. A. Francis, "Consistency of open-loop experimental frequency-response data with coprime factor plant models," *Automatic Control, IEEE Transactions on*, vol. 43, no. 12, pp. 1680-1691, 1998.
- [20] L. Chen and R. Smith, "Closed-loop model validation for an inverted pendulum experiment via a linear matrix inequality approach," in *IEEE CONFERENCE ON DECISION AND CONTROL*, 1997.
- [21] L. Chen and R. Smith, "Closed-loop model validation; an application to an unstable experimental system," in *American Control Conference, 1998*, 1998.
- [22] G. Dullerud and R. Smith, "The validation of model sets on the basis of closed-loop feedback system generated data," in *Computer Aided Control System Design, Proceedings of the 1999 IEEE International Symposium on*, 1999.
- [23] R. Smith and G. Dullerud, "Modeling and validation of nonlinear feedback systems," in *Robustness in identification and control*, London, Springer, 1999, pp. 87-101.
- [24] M. P. Newlin and R. S. Smith, "A generalization of the structured singular value and its application to model validation," *Automatic Control, IEEE Transactions on*, vol. 43, no. 7, pp. 901-907, 1998.
- [25] P. A. Parrilo, M. Sznaier and R. S. S. Pena, "Mixed time/frequency-domain based robust identification," *Automatica*, vol. 34, no. 11, pp. 1375-1389, 1998.
- [26] D. Xu, Z. Ren, G. Gu and J. Chen, "LFT uncertain model validation with time-and frequency-domain measurements," *Automatic Control, IEEE Transactions on*, vol. 44, no. 7, pp. 1435-1441, 1999.
- [27] R. A. de Callafon, "Coprime factor based closed-loop model validation," in *IEEE Conference on Decision and Control*, Sydney, Australia, 2000.
- [28] R. de Callafon and P. Van Den Hof, "Closed-loop model validation using coprime factor uncertainty models," in *Prepr. 12th IFAC Symposium on System Identification*, 2000.
- [29] M. Crowder and R. A. de Callafon, "coprime factor perturbation models for closed-loop model validation techniques," in *Proc. 13th IFAC Symposium on System Identification*, 2003.
- [30] M. Crowder and R. de Callafon, "Coprime factor based closed-loop model validation applied to a flexible structure," in *Decision and Control, 2003. Proceedings. 42nd IEEE Conference on*, Maui, Hawaii, 2003.
- [31] T. Zhou, "Unfalsified probability estimation for a model set based on frequency

- domain data," *International Journal of Control*, vol. 73, no. 5, pp. 391-406, 2000.
- [32] T. Zhou, "Quality evaluation for a coprime factor perturbed model set based on frequency-domain data," *Automatic Control, IEEE Transactions on*, vol. 46, no. 6, pp. 920-927, 2001.
- [33] W. Liu and J. Chen, "Probabilistic bounds for model invalidation assessment," in *Decision and Control, 2004. CDC. 43rd IEEE Conference on*, 2004.
- [34] W. Liu and J. Chen, "Probabilistic model validation problems with H_∞ type uncertainties," in *American Control Conference, 2005*, 2005.
- [35] R. L. Kosut, "Uncertainty model unfalsification for robust adaptive control," *Annual reviews in control*, vol. 25, pp. 65-76, 2001.
- [36] R. A. De Callafon, R. Nagamune and R. Horowitz, "Robust dynamic modeling and control of dual-stage actuators," *Magnetics, IEEE Transactions on*, vol. 42, no. 2, pp. 247-254, 2006.
- [37] T. A. E. Oomen, "System identification for robust and inferential control: with applications to ILC and precision motion systems," Diss. Technische Universiteit Eindhoven, 2010.
- [38] T. Oomen and O. Bosgra, "Estimating disturbances and model uncertainty in model validation for robust control," in *Decision and Control, 2008. CDC 47th IEEE Conference on*, Cancun, Mexico, 2008.
- [39] T. Oomen and O. Bosgra, "Well-posed model uncertainty estimation by design of validation experiments," in *15th IFAC Symposium on System Identification*, Saint-Malo, France, 2009.
- [40] T. Oomen, R. van Herpen and O. Bosgra, "Robust-control-relevant coprime factor identification with application to model validation of a wafer stage," in *15th IFAC Symposium on System Identification*, Saint-Malo, France, 2009.
- [41] T. Oomen, S. van der Meulen, O. Bosgra, M. Steinbuch and J. Elfring, "A robust-control-relevant model validation approach for continuously variable transmission control," in *American Control Conference*, Baltimore, Maryland, 2010.
- [42] T. Oomen and S. van der Meulen, "High performance continuously variable transmission control through robust control-relevant model validation," *Journal of Dynamic Systems, Measurement, and Control*, vol. 135, no. 6, p. 061018, 2013.
- [43] T. Oomen, R. van Herpen, S. Quist, M. van de Wal, O. Bosgra and M. Steinbuch, "Connecting system identification and robust control for next-generation motion control of a wafer stage," *Control Systems Technology, IEEE Transactions on*, vol. 22, no. 1, pp. 102-118, 2013.
- [44] A. Rytter, "Vibration based inspection of civil engineering structures," Diss. Aalborg University, 1993.
- [45] E. H. Maslen, J. A. Vazquez and C. K. Sortore, "Reconciliation of rotordynamic models with experimental data," *Journal of engineering for gas turbines and power*, vol. 124, no. 2, pp. 351-356, 2002.
- [46] J. A. Vazquez, E. H. Maslen, H. J. Ahn and D. C. Han, "Model identification of a rotor with magnetic bearings," in *ASME Turbo Expo 2001: Power for Land, Sea and Air*, 2001.

- [47] Q. Wang and E. H. Maslen, "Identification of frequency-dependent parameters in a flexible rotor system," *Journal of engineering for gas turbines and power*, vol. 128, no. 3, pp. 670-676, 2006.
- [48] Q. Wang, "Model-based identification and quality estimation in rotordynamics," Dissertation, University of Virginia, 2008.
- [49] Q. Wang, B. Pettinato and E. Maslen, "Identification in rotordynamics: Model-based vs. direct measurements," in *ASME Turbo Expo 2009: Power for Land, Sea, and Air*, Orlando, Florida, 2009.
- [50] Q. Wang, B. Pettinato and E. Maslen, "Identification in rotordynamics: uncertainty analysis and quality estimation," in *ASME Turbo Expo 2009: Power for Land, Sea, and Air*, Orlando, Florida, 2009.
- [51] J. T. Sawicki and R. Madden, "Identification of missing dynamics in rotor systems using robust control theory approach," in *Vibration Problems ICOVP 2011*, 2011.
- [52] R. J. Madden, "Identification of unmodeled dynamics in rotor systems using mu-synthesis approach," Master's Thesis, Cleveland State University, 2010.
- [53] R. J. Madden and J. T. Sawicki, "Rotor model validation for an active magnetic bearing machining spindle using mu-synthesis approach," *Journal of Engineering for Gas Turbines and Power*, vol. 134, no. 9, p. 092501, 2012.
- [54] R. J. Madden, J. T. Sawicki and A. H. Pesch, "Model validation for identification of damage dynamics," *Journal of Engineering for Gas Turbines and Power*, vol. 137, no. 6, p. 062506, 2015.
- [55] R. J. Madden, A. H. Pesch and J. T. Sawicki, "Model validation for damage identification and determination of local damage dynamics," in *Proceedings of the 9th IFToMM International Conference on Rotor Dynamics*, San Francisco, 2015.
- [56] R. J. Madden, A. H. Pesch and J. T. Sawicki, "A combined model-based identification and model validation approach for damage identification," *Structural Health Monitoring 2015*, 2015.
- [57] W. Fan and P. Qiao, "Vibration-based damage identification methods: a review and comparative study," *Structural Health Monitoring*, vol. 10, no. 1, pp. 83-111, 2011.
- [58] R. Y. Liang, J. Hu and F. Choy, "Theoretical study of crack-induced eigenfrequency changes on beam structures," *Journal of Engineering Mechanics*, vol. 118, no. 2, pp. 384-396, 1992.
- [59] A. Morassi, "Crack-induced changes in eigenparameters of beam structures," *Journal of Engineering Mechanics*, vol. 119, no. 9, pp. 1798-1803, 1993.
- [60] R. Y. Liang, F. K. Choy and J. Hu, "Detection of cracks in beam structures using measurements of natural frequencies," *Journal of the Franklin Institute*, vol. 328, no. 4, pp. 505-518, 1991.
- [61] A. Messina, E. J. Williams and T. Contursi, "Structural damage detection by a sensitivity and statistical-based method," *Journal of sound and vibration*, vol. 216, no. 5, pp. 791-808, 1998.
- [62] Z. Y. Shi, S. S. Law and L. M. Zhang, "Damage localization by directly using incomplete mode shapes," *Journal of Engineering Mechanics*, vol. 126, no. 6, pp. 656-660, 2000.

- [63] J. J. Lee, J. W. Lee, J. H. Yi, C. B. Yun and H. Y. Jung, "Neural networks-based damage detection for bridges considering errors in baseline finite element models," *Journal of Sound and Vibration*, vol. 280, no. 3, pp. 555-578, 2005.
- [64] K. M. Liew and Q. Wang, "Application of wavelet theory for crack identification in structures," *Journal of Engineering Mechanics*, vol. 124, no. 2, pp. 152-157, 1998.
- [65] L. J. Hadjileontiadis, E. Douka and A. Trochidis, "Fractal dimension analysis for crack identification in beam structures," *Mechanical Systems and Signal Processing*, vol. 19, no. 3, pp. 659-674, 2005.
- [66] A. K. Pandey, M. Biswas and M. M. Samman, "Damage detection from changes in curvature mode shapes," *Journal of sound and vibration*, vol. 145, no. 2, pp. 321-332, 1991.
- [67] M. A. Wahab and G. De Roeck, "Damage detection in bridges using modal curvatures: application to a real damage scenario," *Journal of Sound and Vibration*, vol. 226, no. 2, pp. 217-235, 1999.
- [68] C. P. Ratcliffe, "Damage detection using a modified Laplacian operator on mode shape data," *Journal of Sound and Vibration*, vol. 204, no. 3, pp. 505-517, 1997.
- [69] B. H. Kim, T. Park and G. Z. Voyiadjis, "Damage estimation on beam-like structures using the multi-resolution analysis," *International Journal of Solids and Structures*, vol. 43, no. 14, pp. 4238-4257, 2006.
- [70] A. K. Pandey and M. Biswas, "Damage detection in structures using changes in flexibility," *Journal of Sound and Vibration*, vol. 169, no. 1, pp. 3-17, 1991.
- [71] W. X. Ren and G. De Roeck, "Structural damage identification using modal data. I: Simulation verification," *Journal of Structural Engineering*, vol. 128, no. 1, pp. 87-98, 2002.
- [72] W. X. Ren and G. De Roeck, "Structural damage identification using modal data. II: Test verification," *Journal of Structural Engineering*, vol. 128, no. 1, pp. 96-104, 2002.
- [73] M. Athans, D. Castanon, K. P. Dunn, C. Greene, W. Lee, N. Sandell Jr and A. S. Willsky, "The stochastic control of the F-8C aircraft using a multiple model adaptive control (MMAC) method--Part I: Equilibrium flight," *Automatic Control, IEEE Transactions on*, vol. 22, no. 5, pp. 768-780, 1977.
- [74] M. G. Safonov, "Origins of robust control: Early history and future speculations," *Annual Reviews in Control*, vol. 36, no. 2, pp. 173-181, 2012.
- [75] M. G. Safonov and M. Athans, "Gain and phase margin for multiloop LQG regulators," in *Proceedings of the IEEE conference on decision and control*, Clearwater Beach, FL, 1976.
- [76] M. G. Safonov, "Robustness and stability aspects of stochastic multivariable feedback system design," Diss. Massachusetts Institute of Technology, 1977.
- [77] J. Doyle, "Analysis of feedback systems with structured uncertainties," *IEEE Proceedings D (Control Theory and Applications)*, vol. 129, no. 6, pp. 242-250, 1982.
- [78] G. Zames, "Feedback and optimal sensitivity: Model reference transformations, multiplicative seminorms, and approximate inverses," *Automatic Control, IEEE*

- Transactions on*, vol. 26, no. 2, pp. 301-320, 1981.
- [79] G. Balas, "Robust control of flexible structures: Theory and experiments," Diss. California Institute of Technology, 1990.
 - [80] S. Skogestad and I. Postlethwaite, *Multivariable Feedback Control Analysis and Design*, West Sussex: John Wiley & Sons, Ltd, 2005.
 - [81] K. Zhou and J. C. Doyle, *Essentials of Robust Control*, Upper Saddle River, New Jersey: Prentice-Hall, Inc., 1998.
 - [82] F. Paganini and J. Doyle, "Analysis of implicitly defined systems," in *Decision and Control, 1994., Proceedings of the 33rd IEEE Conference on*, 1994.
 - [83] T. R. Parks, *Manual for Model 210/210a Rectilinear Control System*, Bell Canyon: Educational Control Products, 1999.
 - [84] M. I. Friswell, J. E. T. Penny, S. D. Garvey and A. W. Lees, *Dynamics of rotating machines*, New York: Cambridge University Press, 2010.
 - [85] R. Gasch, "A survey of the dynamic behaviour of a simple rotating shaft with a transverse crack," *Journal of sound and vibration*, vol. 160, no. 2, pp. 313-332, 1993.
 - [86] I. W. Mayes and W. G. R. Davies, "A method of calculating the vibrational behaviour of coupled rotating shafts containing a transverse crack," *Vibrations in rotating machinery*, pp. 17-27, 1980.
 - [87] I. W. Mayes and W. G. R. Davies, "Analysis of the response of a multi-rotor-bearing system containing a transverse crack in a rotor," *Journal of Vibration and Acoustics*, vol. 106, no. 1, pp. 139-145, 1984.
 - [88] O. S. Jun, H. J. Eun, Y. Y. Earmme and C. W. Lee, "Modelling and vibration analysis of a simple rotor with a breathing crack," *Journal of Sound and vibration*, vol. 155, no. 2, pp. 273-290, 1992.
 - [89] J. E. T. Penny and M. I. Friswell, "Simplified modelling of rotor cracks," *Key Engineering Materials*, vol. 245, pp. 223-232, 2003.
 - [90] N. Ozay and M. Sznaiier, "A pessimistic approach to frequency model (in) validation," in *Decision and Control, 2007 46th IEEE Conference on*, 2007.
 - [91] M. I. Friswell, "Damage identification using inverse methods," *Philosophical Transactions of the Royal Society A: Mathematical, Physical and Engineering Sciences*, vol. 365, no. 1851, pp. 392-410, 2007.
 - [92] Y. Liu, W. Chen, P. Arendt and H. Z. Huang, "Toward a better understanding of model validation metrics," *Journal of Mechanical Design*, vol. 133, no. 7, p. 071005, 2011.
 - [93] T. Buranathiti, J. Cao, W. Chen, L. Baghdasaryan and Z. C. Xia, "Approaches for model validation: methodology and illustration on a sheet metal flanging process," *Journal of Manufacturing Science and Engineering*, vol. 128, no. 2, pp. 588-597, 2006.
 - [94] R. G. Hills, "Model validation: model parameter and measurement uncertainty," *Journal of Heat Transfer*, vol. 128, no. 4, pp. 339-351, 2006.
 - [95] R. Rebba, S. Huang, Y. Liu and S. Mahadevan, "Statistical validation of simulation models," *International Journal of Materials and Product Technology*, vol. 25, no.

- 1, pp. 164-181, 2006.
- [96] S. Mahadevan and R. Rebba, "Validation of reliability computational models using Bayes networks," *Reliability Engineering & Systems Safety*, vol. 87, no. 2, pp. 223-232, 2005.
- [97] W. L. Oberkampf and M. F. Barone, "Measures of agreement between computation and experiment: validation metrics," *Journal of Computational Physics*, vol. 217, no. 1, pp. 5-36, 2006.
- [98] S. Ferson, W. L. Oberkampf and L. Ginzburg, "Model validation and predictive capability for the thermal challenge problem," *Computer Methods in Applied Mechanics and Engineering*, vol. 197, no. 29, pp. 2408-2430, 2008.
- [99] S. Ferson and W. L. Oberkampf, "Validation of imprecise probability models," *International Journal of Reliability and Safety*, vol. 3, no. 1, pp. 3-22, 2009.
- [100] R. Gasch, "Dynamic behaviour of a simple rotor with a cross sectional crack," in *Vibrations in Rotating Machinery*, 1976.
- [101] I. W. Mayes and W. G. R. Davies, "Analysis of the response of a multi-rotor-bearing system containing a transverse crack in a rotor," *Journal of Vibration and Acoustics*, vol. 106, no. 1, pp. 139-145, 1984.

APPENDIX

Finite Element Parameters

Node Locations

Station #	1	2	3	4	5	6	7	8	9	10
Location (m)	0.000	0.015	0.175	0.295	0.335	0.450	0.471	0.486	0.615	0.660

Rotor-Bearing Properties

Outer Diameter (m)	0.016
Inner Diameter (m)	0.000
Density (kg/m ³)	7.809×10 ³
Young's Modulus (GPa)	224.08
Shear Modulus (GPa)	83
Disc Mass (kg)	0.9299
Disc Polar Moment of Inertia (kg/m ²)	0.0025
Disc Transverse Moment of Inertia (kg/m ²)	0.0011
AMB Rotor Mass (kg)	0.7521
AMB Rotor Polar Moment of Inertia (kg/m ²)	2.3938×10 ⁻⁴
AMB Rotor Transverse Moment of Inertia (kg/m ²)	3.5264×10 ⁻⁴
Support Bearing Stiffness (N/m)	40×10 ⁹